UNIVERSITÉ PAUL VERLAINE-METZ

NORTHEASTERN UNIVERSITY

DISSERTATION

Presented at
University of Paul Verlaine-Metz and Northeastern University

LI Lei 李磊

To obtain the doctor's degree of

University of Paul Verlaine-Metz and Northeastern University

SPECIAL FIELD: Engineering Sciences
OPTION: Materials Science

Effect of magnetic field on crystallography and microstructure of as-cast Al-based binary alloys

Defended on the 22nd of October 2010 in front of the jury:

Y. FAUTRELLE	Professor	Institut National Polytechnique de Grenoble, France	Reviewer
Z. REN	Professor	Shanghai University, China	Reviewer & Jury member
C. ESLING	Professor	University of Paul Verlaine-Metz, France	Supervisor
J. CUI	Professor	Northeastern University, China	Supervisor
Y. ZHANG	Doctor	University of Paul Verlaine-Metz, France	Co-Supervisor
Z. ZHAO	Doctor	Northeastern University, China	Co-Supervisor
X. ZHAO	Professor	Northeastern University, China	Jury member
X. LI	Professor	Shanghai University, China	Jury member

Laboratoire d'Etude des Textures et Application aux Matériaux CNRS-FRE 7078
Ile du Saulcy 57045 Metz Cedex 1

Abstract

In this work, hypereutectic Al-3.31wt.%Fe and hyperperitectic Al-1.36wt.%Zr alloys are solidified in non-directional ways without and with high magnetic field, and isomorphous Al-9.8wt%Zn and hypoeutectic Al-0.24wt%Fe alloys are semi-continuously cast without and with conventional direct current (DC) magnetic field. The effects of magnetic field on the crystallography and microstructures of these alloys are theoretically and experimentally studied.

Without a high magnetic field, a crystallographic feature investigation on the primary Al_3Fe and Al_3Zr crystals in the respective Al-3.31wt.%Fe and Al-1.36wt.%Zr was carried out. For the primary Al_3Fe crystals, they are bar-shaped and possess two preferred crystallographic extension directions (<010> or <011>). Compound twin and type I twin are found in them (their complete twinning elements have been determined). Type I twin causes the crystals to bend. The Al_3Fe crystals are in forms of monoclinic and triclinic prisms. The crystallographic planes have been identified as (100) and (001) for the monoclinic prism in the extension direction and (001), (001) and (02-1) for the triclinic prism. The formation of the twins is attributed to the (100) and (001) planes exposed to the Al melt during the growth. For the primary Al_3Zr crystals, they are tabular and display two forms of longitudinal cuts - octagonal (smaller sized) and rectangular (larger sized). The faceted planes binding the crystals are determined as {001}, {101} and {111} for the smaller sized crystals and only {001} and {101}) for the larger sized ones. One compound twin with two variants is found in the dendritic crystals (the complete twinning elements are determined). The tabular shape is attributed to the low roughness of {001} planes and thus the low migration rate. The disappearance of {111} planes in the larger sized crystals result from their high roughness and thus the high migration rates. The twin formation is realized by lattice shear plus local atom stacking fault accompanied by local atomic reshuffling.

The applied magnetic field shows little effect on the above crystallographic features of these two crystals but exhibits remarkable effect on some other precipitation behaviors of them. A uniform high magnetic field tends to eliminate the gravity segregation of the primary Al_3Fe crystals by the magnetic viscosity force, whereas a positive gradient one moves them towards the maximum filed intensity zone to segregate at the other end of the specimen by the magnetization force. However, the distribution of primary Al_3Zr crystals is not strongly affected by the magnetic field due to their high density - most of them are segregated at the lower part of the ingot. The magnetic torque induced by the magnetic anisotropy tends to rotate the primary Al_3Fe and Al_3Zr crystals in the deposit layers and thus creates strong preferential crystallographic orientation in the field direction. However, the alignment of the long bar-shaped Al_3Zr crystals and dendritc ones is disturbed by the gravity force and the inconsistence of the preferred direction between the branches and trunks, respectively. The magnetic field also induces bifurcation and cracking of the Al_3Fe through the thermoelectric magnetic force and the shrinkage coefficient difference between the Al_3Fe and the Al matrix. Crystal detachment and

solute diffusive suppression enhances the nucleation of the primary Al_3Fe. The interaction between the increased crystals by the increased Zr content weakens the alignment tendency of the Al_3Zr crystals in the deposit layer in the field direction.

During the semi-continuous casting, the low conventional DC magnetic field transfers the mixture of equiaxed and columnar grains in Al-9.8wt%Zn to twinned feathery ones, and the columnar grains in Al-0.24wt%Fe to twinned lamellas. Both transformations are accompanied by a change of growth directions from <100> to <110> and finally result in the formation of strong crystallographic texture and CSL Σ3 boundaries. The transformations are attributed to the modification of the solidification conditions at the liquid/solid front by the Lorentz force induced by the magnetic field.

The experimental examination and theoretical study of the effect of the magnetic field on the microstructure and crystallography of the aluminum alloys during solidification carried out in this work contribute to the enrichment of the theory of Electromagnetic Processing of Materials (EPM) and are of both theoretical significance and technical interest. The positive results on gravity segregation control and texturation of aluminum alloys through the application of a magnetic field could offer useful guidance for practical material processing techniques.

Keywords: Al-based alloys; Solidification; Magnetic field; Crystallography; Microstructure

摘　要

本文在无磁场和强磁场下以非定向的方式凝固了过共晶 Al-3.31wt.%Fe、过包晶 Al-1.36wt.%Zr 和过共晶 Al-95.54wt.%Zn 合金，在无磁场和普通直流磁场下半连续铸造了匀晶 Al-9.8wt%Zn 和亚共晶 Al-0.24wt%Fe 合金。从实验和理论的角度，详细研究了磁场对这些合金的晶体学和微观组织的影响。

无磁场时分别考察了在Al-3.31wt.%Fe和Al-1.36wt.%Zr合金凝固中形成的初生Al_3Fe和Al_3Zr相的晶体学特征。对于初生Al_3Fe晶体，它们呈棒状并且拥有两个晶体学择优延伸方向(<010>或<011>)。在这些晶体中还发现了混合型和I型孪晶(本文已经确定了它们的完整孪生要素)。I型孪晶的形成使晶体发生了弯曲。此外，初生Al_3Fe晶体具有单斜或三斜柱的形貌。对于单斜柱，在延伸方向上其晶体学面确定为(100)和(001)；而对于三斜柱，包裹它的晶体学面为{001}，{101}和{111}。孪晶的形成归因于(100)和(001)面在晶体生长过程中暴露在了Al熔体中。对于初生Al_3Zr晶体，它们呈层片状并显示出两种形状的纵截面：八边形(小尺寸)和四边形(大尺寸)。其中，包裹小尺寸初生晶体的晶体学面为{001}，{101}和{111}，而包裹大尺寸的只有{001}和{101}。此外，还在枝晶状的晶体中发现了含有两个变体的混合型孪晶(本文已经确定了它们的完整孪生要素)。片状形貌是由{001}面的低粗糙度导致的低迁移速率所引起的，而大尺寸晶体中的{111}面的消失则是由其高粗糙度所导致的高迁移率所造成的。孪晶是由点阵切变加上局部原子层错并伴随局部原子重置所形成的。

施加磁场对以上两种初生晶体的晶体学特点影响很小，但对它们的析出行为却产生了重要影响。匀强磁场通过诱发的磁粘滞阻力趋于消除初生Al_3Fe晶体的重力偏析，而正梯度磁场则通过诱发的磁化力使它们朝磁感应强度最大位置的方向发生了迁移并在试样的另一端形成了新的偏析。然而，初生Al_3Zr晶体由于密度很大，其分布受磁场的影响很小 – 大部分聚集在样品的下部。由磁各向异性所诱发的磁力矩趋于使初生Al_3Fe和位于沉积层中的Al_3Zr晶体发生旋转，从而在磁场方向上形成强烈的择优晶体学取向。然而，长棒和枝晶状的Al_3Zr晶体则分别会受到重力和枝晶与主干择优取向不一致的干扰。此外，磁场还能够诱发初生Al_3Fe晶体的轴向分叉和横向裂纹及形核数的增加。其中，分叉是热电磁力诱发的，裂纹是Al_3Fe晶体与Al基体之间的收缩系数差造成的，形核数的增加则与晶体分离和溶质扩散的抑制有关。对于沉积层中的初生Al_3Zr晶体，锆元素含量的增加弱化了它们在磁场方向上的排列趋势，这是由于晶体析出量的增加导致了它们之间的相互作用。

在半连续铸造过程中，低强度普通直流磁场把Al-9.8wt%Zn合金中由等轴晶和柱状晶构成的组织转变成羽毛状晶，而把Al-0.24wt.%Fe合金中的柱状晶转变成层片状孪晶。

此外，这两种组织转变均伴随着生长方向从<100>到<110>的改变，从而在两种合金中形成了强烈的晶体学织构和CSL Σ3晶界。这些现象与磁场所诱发的Lorentz力所造成的固液界面凝固条件的改变有关。

本文考察了在铝合金凝固过程中施加磁场后其对合金的晶体学和微观组织的影响，在实验和理论上丰富了材料电磁处理(Electromagnetic Processing of Materials，简称EPM)领域的知识，因此这一工作具有重要的理论价值和现实意义。本文通过磁场来控制铝合金组织中晶体的比重偏析和织构化的实验结果为实际材料处理过程提供了一定的指导作用。

关键词：铝基合金；凝固；磁场；晶体学；微观组织

Résumé

Dans ce travail, des alliages hypereutectiques Al-3.31%Fe et hyperperitectic Al-1.36%Zr sont préparés par solidification non-directionnelle avec et sans champ magnétique intense, et des alliages isomorphes Al-%9.8Zn et hypoeutectiques Al-0.24%Fe sont préparés en coulée semi-continue avec et sans application de champ magnétique statique conventionnel. Les effets d'un champ magnétique sur la cristallographie et la microstructure de ces alliages sont étudiés théoriquement et expérimentalement.

Les caractéristiques cristallographiques des cristaux primaires de Al_3Fe et Al_3Zr obtenus, sans l'application de champ magnétique intense, dans les alliages respectifs Al-3.31%Fe et Al-1.36% Zr ont été étudiées. Les cristaux primaires de Al_3Fe sont en forme de barre et possèdent deux directions cristallographiques privilégiées d'extension (<010> ou <011>). Ils renferment des macles de type composées et de type I. Leurs éléments de maclage ont été complètement déterminés. Les macles de type I sont à l'origine de la courbure des cristaux. Les cristaux de Al3Fe ont des formes de prismes monocliniques et tricliniques. Les plans cristallographiques ont été identifiés comme (100) et (001) pour le prisme monoclinique dans la direction d 'extension et (001), (001) et (02-1) pour le prisme triclinique. La formation des macles est attribuée aux plans (100) et (001) exposés à l'Al fondu pendant la croissance. Pour les cristaux Al_3Zr primaire, ils sont de forme tabulaire et présentent deux formes de coupe longitudinale - octogonale (pour ceux de petite taille) et rectangulaires (pour les plus grandes tailles). Les facettes délimitant les cristaux sont déterminées comme (001), (101) et (111) pour les cristaux de plus petite taille et (001) et (101)) pour ceux de plus grande taille. Une macle composée avec deux variants est trouvée dans les cristaux dendritiques (les éléments de jumelage complets ont été déterminés). La forme tabulaire est attribuée à la faible rugosité de plans (001) et donc au faible taux de migration. La disparition des plans (111) dans les cristaux de plus grande taille résulte de leur rugosité élevée et donc du taux de migration élevé. La formation de macles est réalisée par cisaillement du réseau local plus faute d'empilement atomique accompagnée d'un remaniement atomique local.

Le champ magnétique appliqué montre peu d'influence sur les caractéristiques cristallographiques ci-dessus de ces deux cristaux, mais présente une influence remarquable sur certains autres de leur comportements de précipitation. Un champ magnétique uniformité élevé tend à éliminer la ségrégation par gravité des cristaux Al_3Fe primaires par la force de viscosité magnétique, alors qu'une gradient de champ positif les déplace vers la zone d'intensité maximale pour ségréger à l'autre bout de l'échantillon sous l'effet de la force d'aimantation. Toutefois, la répartition des cristaux primaires d'Al_3Zr n'est pas fortement affectée par le champ magnétique en raison de leur haute densité - la plupart d'entre eux sont ségrégés à la partie inférieure du lingot. Le couple magnétique induit par l'anisotropie magnétique tend à faire tourner le et les cristaux primaires Al_3Fe et Al_3Zr dans les couches de dépôt et crée ainsi une forte orientation cristallographique préférentielle dans la direction du champ. Toutefois,

l'alignement des longs cristaux d'Al_3Zr en forme de barre et des cristaux dendritiques est perturbé par la force de gravité et par l'inconsistance de la direction privilégiée entre les branches et les troncs, respectivement. Le champ magnétique induit également des bifurcations et des fissurations d'Al_3Fe par l'intermédiaire de la force thermoélectrique magnétique et de la différence entre les coefficients de retrait d'Al_3Fe et de la matrice Al. Le détachement de cristaux et l'énergie d'aimantation ainsi que la suppression de la diffusion du soluté accroissent la nucléation d'Al_3Fe primaire. L' augmentation de l'interaction entre les cristaux due à l'augmentation du contenu en Zr affaiblit la tendance d'alignement, dans la direction du champ, des cristaux Al_3Zr dans la couche de dépôt.

Au cours de la coulée semi-continue, le faible champ magnétique statique transfère le mélange de grains équiaxes et colonnaires d'Al-9.8%Zn en grains de type « plumeau » maclés, et les grains colonnaires d'Al-0.24%Fe en lamelles maclées. Les deux transformations sont accompagnées d'un changement de directions de croissance de <100> à <110> et, enfin, entraînent la formation d'une forte texture cristallographique forts et de joints de coïcidence (Coincident Site Lattice CSL) Σ3. Les transformations sont attribués à la modification des conditions de solidification à l'interface liquide / solide par la force de Lorentz induite par le champ magnétique.

L'examen expérimental et l'étude théorique de l'effet du champ magnétique sur la microstructure et la cristallographie des alliages d'aluminium pendant la solidification menés dans ce travail contribuent à l'enrichissement de la théorie du traitement électromagnétique des matériaux (Electromagnetic Processing of Materials EPM) et présentent un intérêt à la fois théorique et technique. Les résultats positifs sur le contrôle de la ségrégation par gravité et la texturation des alliages d'aluminium par l'application d'un champ magnétique pourraient offrir des orientations utiles pour le traitement pratique des matériaux.

Contents

Chapter 1 Introduction

1.1 Outline

Nowadays magnetic field has been widely used both in industrial production and people's daily lives. However, human beings experience a long and tortuous process from recognizing to applying it. During this process, many excellent scientists made brilliant contributions to its development: Edmond Halley proposed time-dependent and multi-polar models to explain the earth magnetism in 1683; Hans Christian Oersted discovered the relationship between electrical current and magnetism in 1820 and later André-Marie Ampére formulated a law of electromagnetism on the basis of Oersted's foundation; Faraday discovered the electromagnetic induction in 1831. However, a substantial breakthrough in theory was made by James Clerk Maxwell. His set of Maxwell's equations first appeared in fully developed form in Electricity and Magnetism in 1873. These equations made all the other classical laws or equations of these disciplines simplified. Thanks to these scientists' hard work, people's lives have been completely changed since the magnetic field was widely used.

The technologies applying electromagnetic fields in the materials processing also have a long development history [1]. In 1923 and 1932, electromagnetic levitation and electromagnetic mixing were invented, respectively. However, there was not too much scientific understanding about them at that time. To link up the technology with the scientific understanding, Magnetohydrodynamics (MHD) established in 1942 by Alfven was first introduced at the IUTAM conference at Cambridge University in 1982. Afterwards, in 1994, EPM (Electromagnetic Processing of Materials) was firstly and formally established and used at the International Symposium on Electromagnetic Processing of Materials in Nagoya, Japan [2]. Thus, a special term for the application of magnetic fields in materials processing was born. Henceforth, the successive symposium was held every three years in France and Japan in turn.

Before the maturity of the superconducting magnetic technologies, the mainly used magnetic field in materials processing was conventional electromagnetic field (usually less than 2 Tesla produced by conventional electromagnets and permanent magnets). Its effect on

matters was mainly limited to a macroscopic scale due to its weak intensity. A substantial change of the magnetic field effect on matters did not take place until 1980s when a direct current high magnetic field became available [3]. With a strong and powerful magnetic energy, a high magnetic field can affect the matters in a microscopic scale, such as atom arrangement, matching and migration, which are usually neglected in conventional field. The effects of high magnetic field have been examined under several processes such as solidification [4], electro-deposition [5], vapour-deposition [6] and solid phase reaction [7].

The metallurgists are working hard to obtain various properties of materials to meet the different demands of people. Since electromagnetic field was applied in materials processing, many interesting phenomena and functions have been found. Encouraged by this, EPM is being developed quickly. After many years of development, a new branch of materials science, i.e. applying magnetic field in materials processing, has been formed.

1.2 Solidification in magnetic field

1.2.1 Introduction

Solidification is a process of transformation from liquid to solid. It is one of the most important processes for metallic alloys as it is not only widely used for shaping materials to desired products but also for controlling the macro- and microstructures which are intimately related to the final properties of the alloys.

It is well known that convection in the molten metallic alloys is an important phenomenon to be treated during the solidification as it is directly associated with the heat and mass transfer of the melt. There are many sources of convection during solidification, such as mold filling, buoyancy, floating or settling of free crystals, thermocapillary forces and mechanical and/or magnetic stirring. A good control of the convective patterns in the melt of metallic alloys during the solidification can help improve the macro- and microstructures and thus the final properties of alloys. Luckily, the application of a conventional electromagnetic field makes this control available as it can induce Lorentz force in the melt and then suppresses or stirs the melt.

In contrast to the conventional electromagnetic field, the introduction of a high magnetic field to the solidification process of metallic alloys can induce more enhanced effects. Besides

the Lorentz force, high magnetic field makes the magnetization force that is usually negligible in conventional magnetic field emerge. Magnetization force is usually classified into two different kinds – one is by which materials are rotated to a magnetic field direction as a compass rotates to the north direction, and the other is by which ferromagnetic and paramagnetic materials are pulled to a magnet and the diamagnetic ones are repulsed [8]. These two kinds of magnetization forces are of importance in affecting the macro- and microstructures of the alloys during the solidification process. The former can rotate the crystals with obvious magnetic anisotropies in the melt to some preferred crystallographic orientation to generate macroscopic texture; whereas the latter can modify the distribution of the related phases. Other than Lorentz force and magnetization force, thermoelectric magnetic force (TEMF) can also be induced by the magnetic field during the solidification process and plays an important role in affecting the macro- and microstructures of the alloys.

So far, large industrial and experimental achievements have been obtained through applying magnetic field during the solidification process of metallic alloys. However, there are still quite some of the metallic alloys waited to be investigated. Based on this, a further study of the effects of magnetic field on various metallic alloys during different solidification processes seems necessary and may bring about some new phenomena.

1.2.2 Solidification in conventional magnetic field

1.2.2.1 Basic principles

(a) Lorentz force

The present principles mainly aim at the imposition of external magnetic field on electroconducting metallic alloy during the solidification process. First, we give the MHD form of Maxwell's equations (SI unit):

$$\begin{aligned} \nabla \times \boldsymbol{E} &= -\frac{\partial \boldsymbol{B}}{\partial \boldsymbol{t}} & \nabla \cdot \boldsymbol{D} &= 0 \\ \nabla \times \boldsymbol{H} &= \boldsymbol{j} & \nabla \cdot \boldsymbol{B} &= 0 \end{aligned} \tag{1.1}$$

where $\boldsymbol{E}$ is electric field intensity, $\boldsymbol{D}$ electric displacement field, $\boldsymbol{H}$ magnetic field intensity, $\boldsymbol{B}$ magnetic flux density, $\boldsymbol{j}$ current density. The Ohm's law for a moving conducting fluid can be expressed as:

$$\boldsymbol{j} = \sigma_e(\boldsymbol{E} + \boldsymbol{u} \times \boldsymbol{B}) \tag{1.2}$$

where σ_e is electrical conductivity and $\boldsymbol{u}$ local velocity of the fluid.

For a macroscopic homogeneous medium, the Maxwell stress tensor $T_{\alpha\beta}$ is given as [9, 10]:

$$T_{\alpha\beta} = \underset{(1)}{\varepsilon E_\alpha E_\beta} + \underset{(2)}{\mu H_\alpha H_\beta} - 0.5\delta_{\alpha\beta}\left[\underset{(3)}{E^2(\varepsilon - \rho\left(\frac{\partial \varepsilon}{\partial \rho}\right)_T}} + \underset{(4)}{H^2\left(\mu - \rho\left(\frac{\partial \mu}{\partial \rho}\right)_T\right)}\right] \tag{1.3}$$

where ε, μ, ρ and T denote the respective electric permittivity, magnetic permeability, fluid density and temperature; E_α, E_β and H_α, H_β represent the respective αth and βth components of the electric field and magnetic field. The Kroneker delta $\delta_{\alpha\beta}$ = 1 when $\alpha = \beta$ and $\delta_{\alpha\beta} = 0$ when $\alpha \neq \beta$ $(\alpha, \beta = 1, 2, 3)$.

Term (1) and (3) in Eq. (1.3) reflect the electrostatic effects that are hardly used during the solidification of conducting fluids. Term (2) and (4) represent the major effect of the electromagnetic field on the solidification of metals. For molten metals, the magnetorestrictive effects can be neglected (i.e. $\rho\left(\frac{\partial \mu}{\partial \rho}\right)_T \approx 0$). Thus, Lorentz force which is the volumetric momentum source of the electromagnetic origin will play a major role in affecting the convection of the melt. The Lorentz force $\boldsymbol{F}$ is equal to the divergence of the Maxwell stress tensor $\underline{\underline{T}}$ [9]:

$$\boldsymbol{F} = \nabla \cdot \underline{\underline{T}} \quad \text{or} \quad F_\alpha = T_{\alpha\beta,\beta} \tag{1.4}$$

where $T_{\alpha\beta,\beta}$ is the derivative of $T_{\alpha\beta}$ with respect to β.

Considering the MHD form of Maxwell's equations in Eq. (1.1) and Ohm's law Eq. (1.2), the expression of Lorentz force $\boldsymbol{F}$ in equation (1.4) can be simplified into a common form:

$$\boldsymbol{F} = \boldsymbol{j} \times \boldsymbol{B} = \nabla \times \boldsymbol{H} \times \boldsymbol{B} = \sigma_e\left(\boldsymbol{E} + \mathrm{u} \times \boldsymbol{B}\right) \times \boldsymbol{B} \tag{1.5}$$

This Lorentz force has two opposite effects – braking or stirring the melt. When a direct current (DC) magnetic field is applied, it brakes the melt; whereas when an alternating current (AC) magnetic field is applied, it stirs the melt.

The electromagnetic braking effect originates from the direct interaction of the applied DC magnetic field $\boldsymbol{B}$ and the melt velocity $\boldsymbol{u}$. When an electroconducting fluid is crossing the magnetic field lines, flux variations occur which result in local electromotive force $\boldsymbol{E}_{\mathrm{m}} = \boldsymbol{E} + \boldsymbol{u} \times \boldsymbol{B}$ and thus induce electric current $\boldsymbol{j} = \sigma_{\mathrm{e}} \left(\boldsymbol{E} + \mathrm{u} \times \boldsymbol{B} \right)$ [11, 12]. $\boldsymbol{j}$ interacts with the applied DC magnetic field and then gives rise to the Lorentz force which can be expressed as

$$\boldsymbol{F} = \underset{(1)}{\sigma_{\mathrm{e}} \boldsymbol{E} \times \boldsymbol{B}} + \underset{(2)}{\boldsymbol{u} \times \boldsymbol{B} \times \boldsymbol{B}} \tag{1.6}$$

During solidification process, $\boldsymbol{E}$ is heavily reduced since the highly conducting solid phase often acts as an electrical short circuit [11]. Thus, term (1) in Eq. (1.6), despite responsible for another force, is negligible. Here, it should be noted that the interaction between $\boldsymbol{B}$ and $\boldsymbol{u}$ is anisotropic because of the presence of two cross products. Therefore, term (2) obviously yields a braking force $-\sigma_{\mathrm{e}} \boldsymbol{B}^2 \boldsymbol{u}$ when $\boldsymbol{B}$ and $\boldsymbol{u}$ are perpendicular; whereas it becomes zero when they are parallel. The negative sign indicates that the direction of the yielded Lorentz force is opposite to that of $\boldsymbol{u}$, suggesting that it counteracts the flow of the melt, as schematically shown in Fig. 1.1(a). However, there is a particularity for this braking force due to its proportionality to the $\boldsymbol{u}$, i.e. the stronger the velocity is, the more efficient is the brake [12]. That is to say, a melt flow can not be damped completely by this braking force.

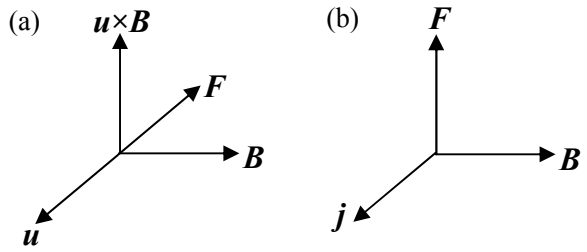

Figure 1.1 Lorentz force $\boldsymbol{F}$ induced by the interaction between (a) the applied DC magnetic field $\boldsymbol{B}$ and the melt with a velocity of $\boldsymbol{u}$ and (b) the applied AC magnetic field $\boldsymbol{B}$ and the induced electric current $\boldsymbol{j}$ [9].

The electromagnetic stirring effect comes from the interaction between the applied AC magnetic field and the induced eddy current. When a liquid metal is submitted to a time varying alternating magnetic field, an eddy current is induced in the melt. This current interacts with the AC magnetic field and then gives rise to an electromagnetic body force – Lorentz force that can also be expressed by Eq. (1.6). This Lorentz force, as opposed to that

induced by a DC magnetic field, can result in a forced convection in the melt, as schematically shown in Fig. 1.1(b). Moreover, this induced Lorentz force can also produce an electromagnetic pressure on the free surface of the melt (especially when a high-frequency AC magnetic field is applied), which is favorable for the improvement of surface quality of casting ingots.

(b) Thermoelectric magnetic force (TEMF)

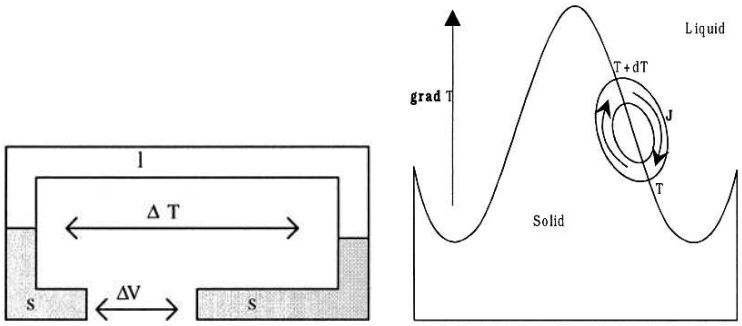

(a) (b)

Figure 1.2 (a) Seebeck effect in a thermocouple and (b) elementary short-circuited thermocouple at the dendritic interface during the solidification of metallic alloy [12].

Based on the principle that the motions of current and heat have the same physical origin (i.e. free electrons), three main effects resulting from the coupling between a temperature gradient and an electrical field can be distinguished: Peltier, Thomson and Seebeck effects [13]. During the solidification process, it has been shown that both Peltier and Thomson heating are negligible [14]. Therefore, only Seebeck effect is discussed in the present work.

First we give the working principle of a thermocouple. When two media of different thermoelectric powers (η_S, η_L) are connected together and a difference of temperature ΔT is present between the two junctions, a voltage ΔV can be measured (see Fig. 1.2(a)) [12]:

$$\Delta V = (\eta_S - \eta_L)\Delta T \tag{1.7}$$

This equation can be expressed more generally in each media by the modified Ohm's law derived from thermodynamics of irreversible processes [15]:

$$j = -\sigma(\nabla V + \eta \nabla T) \tag{1.8}$$

where j is the current density created either by an electrical field or by the electronic movement due to the heat conduction, σ the electrical conductivity, V the electrical potential

and *T* the temperature.

During the solidification process of a metallic alloy, a similar “thermocouple” can be produced at the dendritic interface in a given temperature gradient when the liquid and solid phases show a difference of thermoelectric power (see Fig. 1.2(b)). Different from the real thermocouple, it is short-circuited and then results in the generation of a local current. When a DC magnetic field is applied during the solidification process, this current interacts with the applied field and then creates a thermoelectric Lorentz force, i.e. thermoelectric magnetic force (TEMF).

1.2.2.2 DC magnetic field

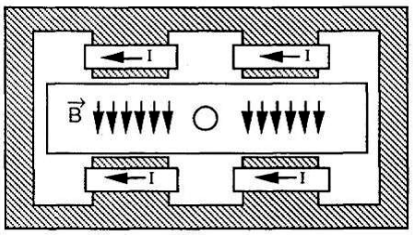

Figure 1.3 Schematic top view of the arrangement of DC magnets [16].

As mentioned previously, DC magnetic field has a braking effect on the melt flow, which has been practiced in commercial continuous casting of steel. This technique of stably controlling the molten steel flow in the mold was developed by applying a level DC magnetic field (LMF) across the mold width. The metallurgical effects of LMF are to minimize the penetration of oxide inclusions into the cast and stabilize the steel flow in the mold so as to avoid the entrainment of liquid flux into the cast. In 1993, Gardin et al. [16] presented a configuration describing the influence of an electromagnetic actuator on steel flows, as schematically shown in Fig. 1.3. The actuator was installed at Sollac Dunkirk on one continuous casting strand in order to be tested and optimized. This device consists of two pairs of induction poles, located on either side of the feeding submerged nozzle. It generates a cross stationary magnetic field in the mold with a highest intensity of 0.32 T for a slab size of 250 mm in thickness. The field creates Lorentz forces which "brake" fluid motion and tend to better disperse the kinetic energy of molten steel jets coming from the nozzle ports in the mold. To better understand the brake effect on flows, they built a numerical tool from the

PHOENICS finite which could predict the effect of an electromagnetic actuator on steel flows and inclusion mass fluxes entrapped by the solidifying shell. The results shows that the field leads to a high confinement of the inclusions in the upper part of the caster and tends to increase the heterogeneity of the inclusion distribution in the widthwise direction of the slab.

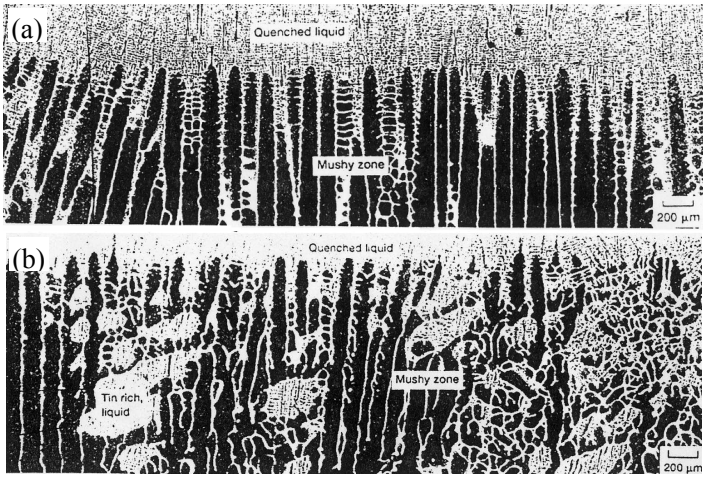

Figure 1.4 Cellular microstructures of directionally solidified Pb-17.7wt.%Sn alloy (a) without and (b) with a 0.45-T transverse magnetic field [21].

Besides the practical application, more experiments were carried out to investigate the effects of the DC magnetic field on the macro- and microstructures of metallic alloys. Uhlmann et al. [17] investigated the effect of a DC magnetic field on the solidification microstructure of Cu-2%Al alloy. It was found that the microstructure is transformed from equiaxed grains without magnetic field to complete columnar grains with an external 0.2-T one. They attribute this to the braking effect on the convection in the melt by the magnetic field, which reduces the dendrite fragmentation and the subsequent crystal multiplication during the solidification. Moreover, the reduction of heat evacuation rate and thus the undercooling of the melt induced by this field decrease the nucleation rate so that equiaxed grains are less formed, which usually block the growth of the columnar grains ahead of them. This also contributes to the complete development of the columnar grains. A similar grain coarsening effect by a DC magnetic field was also observed in an Al-4%Cu alloy [18]. These grain coarsening effects mainly refer to the large ingots solidified in a non-directional way. As a matter of fact, more effects of DC magnetic fields are investigated during the directional solidification of relatively small ingots. Early in 1966, Youdelis et al. [19] applied a

34000-oersteds transverse magnetic field during the directional freezing of Al-Cu alloys and found that the diffusion coefficient and hence the fiber spacing can be reduced. Later in 1970, the same author [20] investigated the effect of a transverse magnetic field on ambipolar diffusion and concluded that for a heterovalent metal alloy significant diffusion inhibition should occur when some condition is met. In 1973, Verhoeven and Pearson [21] solidified eutectic Sn-Cd and Sn-Pb alloys vertically under a transverse magnetic field of 23000 oersteds and found that the magnetic field had no effect on the eutectic lamellar spacing. In 1981, Boettinger et al. [22] imposed a 0.1-Tesla transverse (or axial) magnetic field during the directional solidification of near eutectic Pb-57wt.%Sn alloy, but found that no influence on the microstructure or longitudinal macrosegregation was detected. In 1994 Tewari et al. [23] applied a higher 0.45-Tesla transverse magnetic field during the directional solidification of Pb-17.7wt.%Sn alloy. It was found that the 0.45-Tesla magnetic field has no influence on the morphology of dendrite arrays, but does cause severe distortion in the cellular array morphology, as shown in Fig. 1.4. They attributed this to the anisotropy in the thermosolutal convection caused by the magnetic field. With a deeper study of the effects of DC magnetic field on the macro- and microstructures of metallic alloys, numerical analyses and models are also presented to account for the induced phenomena. In 1995, Alboussiere et al. [24] investigated the axial segregation during horizontal Bridgman growth in the presence of a uniform axial magnetic field. With a numerical and theoretical study, they predict that the Hartmann number has no influence on the axial segregation until it reaches a given value. Two years later, the same authors [25] investigated the segregation in a dilute metallic alloy during horizontal Bridgman growth. This time, they presented a 2-D model to exhibit a critical value of the magnetic field intensity for segregation, above which the effective partition ratio is increasing with the increase of the magnetic field intensity. In the same year, Li [26] developed a fully 3-D numerical model to represent the magnetic damping of complex fluid flow in a melt cavity during the unidirectional solidification of Sn-35.5%Pb alloy. Numerical results show that magnetic damping can be effectively applied to reduce the turbulence and flow levels in the melt undergoing solidification and over a certain threshold value a higher magnetic field resulted in a higher velocity reduction.

When exploring the effects of the DC magnetic field during the solidification of metallic

alloys, thermoelectric effect and thus the TEMF also cannot be neglected. The first experiment to demonstrate thermoelectric effect was performed by Alboussiere et al. [27] in 1991. They directionally solidified Pb-Sn (47at.%Pb) and Bi-Sn (60at.% Bi) alloys under a permanent magnetic field and found that the microstructure is affected and the solute segregation is enhanced with the magnetic field. They attributed these to the thermoelectric currents generated in the dendritic zone and thus could create Lorentz force (i.e. TEMF) able to increase the solutal convection. In 1993 [28] and 1996 [29], Moreau et al considered both Peltier effect and Seebeck effect at all scales and again demonstrated the relevance of these phenomena. In 1998, Lehmann et al. [12] presented a study where they took good advantage of the thermoelectric effect. To investigate the influence of convection on the mushy zone during the horizontal directional solidification of Cu-60mass%Ag and Al-10mass%Cu alloys, they used a transverse DC magnetic field to modify the fluid flow in the dendritic network by thermoelectric magnetohydrodynamic effect. The induced Lorentz force can oppose or reinforce the natural solute buoyancy force and then makes it possible to change only the convective intensity without modifying the other parameters of the growth. More recently, L. et al. [30] applied an axial magnetic field (≤1 Tesla) during the directional solidification of Al-Cu alloy. It was found that the magnetic field caused changes in the macroscopic interface shape and the cellular/dendritic morphology. They attributed these changes to the thermoelectric magnetic convection on the sample scale and the cell/dendrite scale.

Application of DC magnetic field to the solidification process of metallic alloys has brought about fruitful results. However, it is still at an initial stage. Quite some of the mechanisms in explaining the induced phenomena by researchers are just tentative. Considering this, a deeper and wider study in this field is of interest and significance.

1.2.2.3 AC magnetic field

AC magnetic field has been successfully applied to the technique of direct chill (continuous or semi-continuous) casting of aluminium alloys. In 1970s, Getselev [31] developed electromagnetic casting (EMC) on the basis of conventional direct chill of aluminium alloys. In his design, a high frequency (2000-3000Hz) AC magnetic field was applied. During the casting, the molten metal was not confined by a mold but the magnetic

pressure. This pressure results from the induced Lorentz force which balances the metallostatic pressure. EMC remarkably improves the surface qualities of the cast aluminium ingots so that they can be rolled without scalping. In the end of 1980s, Vivès [32] developed CREM (Casting, Refining, Electromagnetic) technique, as schematically shown in Fig. 1.5. Different from Getselev, he applied an AC magnetic field with commercial frequency (50Hz) during the direct chill casting of aluminium alloys. The results indicated that compared with the ingots by conventional direct chill casting method the solidified structures are refined and the surface qualities of the ingots are also improved. These results also arise from the induced Lorentz force by the field. Different from the form given by Eq. (1.5), he described the Lorentz force $\boldsymbol{F}$ in his work as follows:

$$\boldsymbol{F} = \boldsymbol{J} \times \boldsymbol{B} = \underset{(1)}{\frac{1}{\mu}(\boldsymbol{B} \cdot \nabla)\boldsymbol{B}} - \underset{(2)}{\frac{1}{2\mu}\nabla \boldsymbol{B}^2} \tag{1.9}$$

where $\boldsymbol{B}$ and $\boldsymbol{J}$ are the respective magnetic flux density and current density generated in the melt and μ is the permeability of the melt. In Eq. (1.9), term (1) is a rotational component, resulting in a forced convection and flow in the melt; whereas term (2) is a potential force, giving rise to the formation of meniscus and a decrease in the contacting pressure on the mold. These two terms account for the refined structure and the improved surface quality, respectively. Later, in 1990s, on the basis of CREM, Vivès et al. [33, 34] developed electromagnetic vibration technique where a steady DC magnetic field and an AC magnetic field were applied simultaneously. Due to the added magnetic vibration effect besides the stirring effect, much finer structure than that under CREM was obtained.

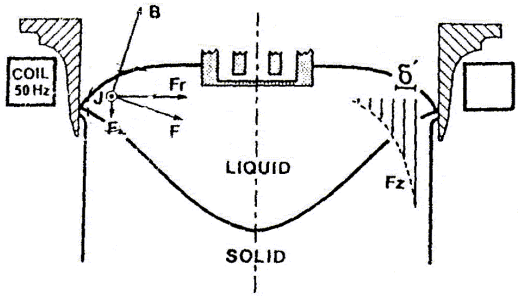

Figure 1.5 Schematic diagram of CREM [33].

It is known that due to the skin effect the Lorentz forces mainly concentrate at the

surface of the melt if the frequency of the AC magnetic field is very high. Provided a much lower frequency field was applied, the electromagnetic forces might be able to penetrate deeper into the melt and then produce a stronger stirring effect. Based upon this, Cui et al. developed LFEC (Low-Frequency Electromagnetic Casting) [35-45]. They applied AC magnetic fields with frequencies of 15-30 Hz during the direct chill casting of aluminium alloys. The results show that LFEC can effectively promote the solution of alloying elements, refine the microstructures and help reduce the macrosegregation and cracks. In addition, despite of the low electromagnetic force at the surface of the melt, the surface qualities of the ingots can also be improved when the magnetic intensity is strong enough.

Due to the easy availability and remarkable effects on the macro- and microstructures of the metallic ingots, conventional AC magnetic field has been widely used in the direct chill casting and is developing quickly.

1.2.3 Solidification in high magnetic field

1.2.3.1 Basic principles

(a) Crystal orientation

When a non-magnetic crystal is submitted to an external magnetic field and magnetized, the magnetization energy of the substance U is usually given as [8]

$$U = -\frac{\chi}{2\mu_0\left(1+N\chi\right)^2}B^2 \tag{1.10}$$

where χ is the magnetic susceptibility of the crystal, μ_0 the permeability in vacuum ($4\pi\times10^{-7}$ [H/m]), N the demagnetization factor and B the magnetic flux density. However, due to the magnetic anisotropy of the crystal, the magnetization energy is also crystallographically dependent. Based on this, the magnetization energy U_i in $\boldsymbol{i}$ crystallographic direction when $\boldsymbol{i}$//$\boldsymbol{B}$ can be expressed as

$$U_\mathrm{i} = -\frac{\chi_\mathrm{i}}{2\mu_0\left(1+N\chi_\mathrm{i}\right)^2}B^2 \tag{1.11}$$

From Eq. (1.10), it can be known that the crystal is in an energetically unstable state if the crystallographic direction with the highest susceptibility is not in the external magnetic field direction. As a consequence, it will be rotated by the magnetic field to its lowest energy state,

i.e. its energetically stable position. The driving force (i.e. the magnetization force) of the rotation originates from the magnetic torque, which is the result of the interaction of the induced magnetization and the applied magnetic field. During the solidification of metallic alloys, the primarily precipitated crystals with strong magnetic anisotropies can be rotated by this toque due to the free liquid environment.

(b) Crystal migration

When a crystal with volume V is precipitated in the melt under an external gradient magnetic field, another pulling or repulsing magnetization force $\boldsymbol{F}$ will be induced to act on it, which usually can be expressed as [2]:

$$\boldsymbol{F} = V\,\chi/\mu_0\left(\boldsymbol{B}\cdot\nabla\right)\boldsymbol{B} \tag{1.12}$$

Under this magnetization force, the crystal may migrate from one position to another.

1.2.3.2 Crystal orientation

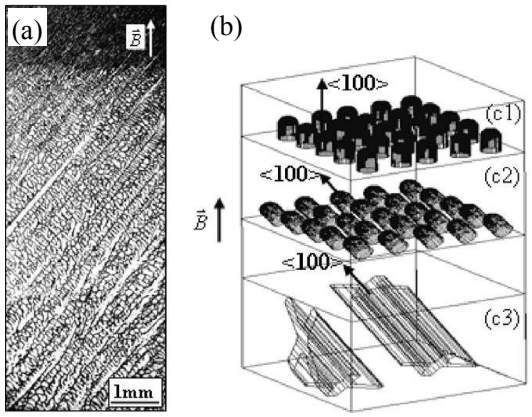

Figure 1.6 (a) the deflected structure on the longitudinal section of Al-4.5wt.%Cu alloy ingot; (b) schematic illustration of the α-Al deflected dendrites growth under the magnetic field [45].

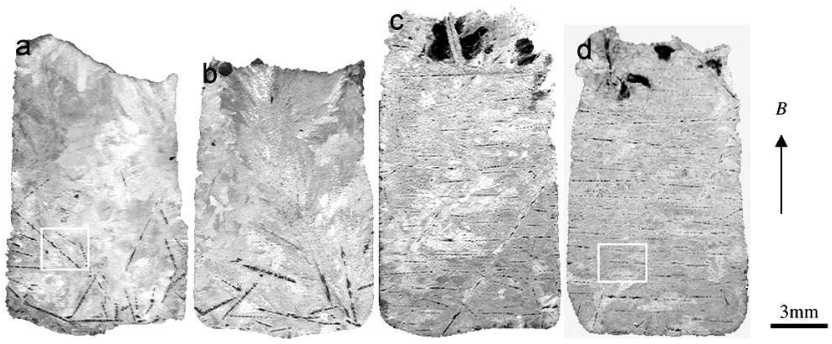

Figure 1.7 Macrostructures of Al-Ni alloy solidified under magnetic field of (a) 0, (b) 1, (c) 4.4 and (d) 8.8 Tesla [54].

As mentioned previously, magnetic orientation arises from the anisotropic magnetization energy of crystals. Owning to this anisotropy, a crystal receives torque in a magnetic field, and then orients to the energetically stable position. However, during the solidification process, four conditions are necessary to realize such an orientation modification [1]: firstly, the precipitated crystals have a crystallographically magnetic anisotropy; secondly, the magnetization energy should be larger than thermal energy; thirdly, the grain is surrounded by fluid; finally, each crystal should be dispersed in the medium.

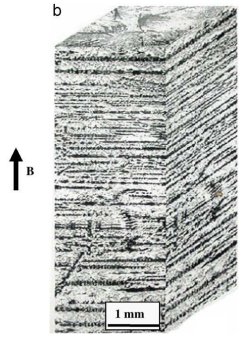

Figure 1.8 Three-dimensional macrostructure of Al-Ni alloy directionally solidified under a magnetic field of 12 Tesla [55].

Once all the necessary conditions are met, the crystals in the melt can be oriented and then reveal a macroscopic texture. This has been verified in many different alloys during the solidification processes. Mikelson et al. [46] reported that the macrostructure of Al-Cu and Cd-Zn alloys aligned in the direction of the magnetic field. Savitisky et al. [47] found that the MnBi phase in the Bi-Mn alloy also aligned in the direction of the magnetic field. Later, Yasuda et al. [48] reported a similar alignment of the MnBi phase in the Bi-Mn alloy. Rango et al. [49] extended the investigation to the solidification of paramagnetic YBa2Cu3O7 material and obtained textured crystal structure in a magnetic field. Katsuki et al. [50] reported that diamagnetic benzophenone crystallized from n-hexane, KCl and $BaCl_2$ crystallized from a solution aligned in a 10 Tesla magnetic field. Asai found that the primary phase in Al-Si-Fe alloy aligned with the longer axis perpendicular to the magnetic field [2]. Textured crystal growth of Bi-2201 [51] and Bi (Pb)-2212 [52] has also been obtained in a high magnetic field. Recently, Li. et al. [53] investigated the influence of a high magnetic field on the alignment behavior of α-Al dendrites in Al-4.5wt.%Cu alloy during the directional solidification. A deflected structure was found on the longitudinal section parallel

to the magnetic field, as shown in Fig. 1.6(a). Normally, they should grow with the preferred crystallographic direction <100> along the temperature gradient direction which is consistent with the magnetic field. However, the α-Al dendrites are oriented by the magnetic field with the easy magnetization axis <111> parallel to the field direction, as shown in Fig. 1.6(b). As a consequence, the primary dendrite arm is deflected from the temperature gradient direction. Wang et al. [54] investigated the effects of a high magnetic field on the alignment of primary Al_3Ni phase in Al-Ni binary alloys during a non-directional solidification process. The results showed that the primary phase Al_3Ni aligns regularly in the direction perpendicular to the imposed magnetic fields, as shown in Fig. 1.7. XRD examination indicated that magnetic field makes (h k 0) and (0 k l) planes of the Al_3Ni crystals oriented parallel and perpendicular to the magnetic field direction, respectively. Different from Wang, Li et al. [45, 56] solidified the Al-Ni alloy in a directional way under a high magnetic field. It was found that a sandwich structure is formed, as shown in Fig. 1.8. By means of the XRD and EBSD analysis, it is determined that the <001> crystallographic direction of the Al_3Ni crystals orients along the magnetic field; whereas <100>, <110> and <010> are perpendicular to the magnetic field. More recently, Liu et al. solidified Mn-89.7wt.%Sb alloy in various magnetic fields with different holding times [57]. The results showed that the primary MnSb crystals are oriented with their c-plane parallel to the magnetic field direction, but the eutectic MnSb can not be oriented.

Crystal alignments are intimately related to the properties of materials, therefore a good control of the crystal orientations becomes significant. Thanks to the development of superconducting magnetic technologies, obtaining materials with desired crystal orientations and thus alignments become possible.

1.2.3.3 Crystal migration

When a crystal precipitated in the melt during the solidification process is submitted to a gradient high magnetic field, the induced magnetization force may move it from one position to another due to the susceptibility difference between the crystal and the melt. If the crystal is ferromagnetic or paramagnetic, it will have a tendency to migrate toward the position with higher magnetic field; whereas if it is diamagnetic, the tendency is just the opposite. This has

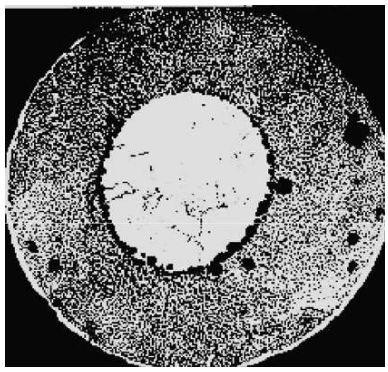

Figure 1.9 Macrostructure in the transverse section of Bi–6wt.%Mn ingot under a radial gradient magnetic field of 10 Tesla [61].

been verified in a series of solidification experiments of various metallic alloys. Sassa et al. [58] reported a migration of primary Si during the solidification of Al-Si alloy. When the sample was put in a positive gradient magnetic field, the Si grains were located at the lower region of the sample; whereas when the sample was put in a negative one, they mostly concentrated at the upper region of the sample. This is directly related to the diamagnetic property of Si crystals and the paramagnetic property of Al melt. A similar migration of the primary Si grains under gradient magnetic field was also found by Wang et al [59]. However, a more detailed investigation on the migration behavior of the primary Si grains was made by Jin et al [60]. They investigated the effects of magnetic flux density and gradient separately during the solidification of Al-18wt.%Si alloy. It was found that under a gradient magnetic field the primary Si grains migrate toward one end of the specimen, forming a Si-rich layer. At a constant magnetization force, the migratory degree of the primary grains decreased with the increase of the magnetic flux density; whereas at a fixed magnetic flux density, the amount of separated primary grains increased with increasing magnetic field gradient. They attributed the results to the combined effects of the magnetization force and the magnetic viscosity of the melt, both of which increase with the increase of the magnetic flux density. Recently, L. et al. [61] showed a typical example of the application of magnetization force on moving crystals. They employed a radial gradient magnetic field during the solidification of Bi-6wt.%Mn alloy. The results indicated that a ring-like primary MnBi phase-rich layer is formed, as shown in Fig. 1.9. As the MnBi phase and the matrix Bi are ferromagnetic and diamagnetic, respectively, the MnBi phase will be subjected to an outward magnetization

force along the radial direction and thus migrates to the peripheral region of the specimen. Based on their experiment, one can imagine that an axial gradient magnetic field will let the primary MnBi phase concentrate at a specific end of the specimen. This has been verified during the solidification of a dilute Bi-Mn alloy by Wang et al. [62]. More recently, Lou et al. investigated the effects of high magnetic fields on the migration of $TiAl_3$ particles during the solidification of Al-7wt.%Si-0.5wt.%Ti alloy [63]. Without magnetic field, the $TiAl_3$ particles segregate at the lower part of the solidified structure. Under uniform magnetic field, the segregation of the particles reduces with the increase of the magnetic flux density. When a negative gradient field is applied, the segregation is further reduced. The segregation of the particles is the result of their much higher density than the Al melt, the reduction of the segregation under uniform magnetic field is related to the increased effective viscosity of the melt and the further reduction under negative magnetic field is attributed to the magnetization force acting on the particles.

According to the magnetic properties of the crystals, we can imagine to control their distribution by the high magnetic field, which is also an important part of materials processing. Based on this, a large number of experiments with various materials seem quite necessary.

1.3 Other material processes with magnetic field

1.3.1 Introduction

Due to the special capacities of magnetic field in affecting materials, more and more researches have been involved in EPM, especially since high magnetic field becomes readily available because of the recent progress in superconducting magnet technique. The quick development of high magnetic field helps extend the research objects from the previous magnetic materials to non-magnetic ones, such as water, air and even organic tissues. Besides solidification process, it has also been applied in many other processes, such as phase transformation, vapour-deposition and electro-deposition, and meanwhile some interesting phenomena have been found.

1.3.2 Phase transformation

Shimotomai et al. [64] applied a 8-Tesla magnetic field during the $\alpha \rightarrow \gamma$ inverse transformation in Fe-C alloys. It was found that two-phase microstructures with the

paramagnetic γ phase are aligned as chains or columns in the matrix of the ferromagnetic α phase along the direction of applied magnetic field. They attributed this to the dipolar interactions between the nuclei of γ phase which are regarded as magnetic poles in the background of ferromagnetic medium of α phase. Sadovsky et al. [65, 66] carried out a series of researches on the effect of magnetic field on martensitic starting point, the amount of martensite obtained and microstructure morphologies appearing during martensitic transformation in some ferroalloys and found that the magnetic field can obviously increase the transformation temperature and promote transformation amount.

1.3.3 Vapour-deposition

Tahashi et al. [67] applied a 5-Tesla high magnetic field during the vapour-depostion process of bismuth. The bismuth was first put into a vacuum chamber set in the bore of a superconducting magnet and then heated up to 1073 K after the pressure in the chamber reached 5×10^{-3} Pa so that they can be deposited onto a glass substrate. The results indicated that bismuth is deposited in the c-plane orientation and the orientation indices in the c-plane increase with an increase of the distance between the target and the substrate, suggesting that the radiation heat due to the laser heat source interrupted the crystal orientation in the vicinity of the target.

1.3.4 Electro-deposition

Takahisa et al. [68] applied a high magnetic field during the electro-deposition process of zinc. A copper substrate as cathode and a zinc plate as anode were set in a vessel as an electrolytic cell under the magnetic field. The result indicated that the observed orientation plane of zinc electrodeposits was the c-plane when the magnetic field was imposed perpendicularly to the cathode substrate plane and the orientation indices of the c-plane increased with the increase of the magnetic field.

1.4 Motivation and objectives

Since magnetic field was involved in materials processing, significant progress has been made. However, due to the complexity of the phenomena, various fundamental issues still exist and impede the development of EPM. Therefore, a deeper and more comprehensive study in this field is required. As an important material, aluminium-based alloys have been

widely used in modern industries, so how to improve their properties is always a hot topic in the field of materials science. Solidification is a key process for controlling the macro- and microstructures and thus the final properties of alloys, and meanwhile magnetic field can induce various effects on materials, therefore applying magnetic fields during the solidification of aluminium-based alloys is worth trying and may bring about some new phenomena and facilitate to the understanding of some fundamental issues. Based upon this background, Al-based binary alloys are chosen as the target material for solidification experiments under both high and conventional DC magnetic field in the present work.

According to the previous analysis, only the crystals with a free liquid environment can be effectively affected by the high magnetic field. Considering this, hypereutectic Al-3.31wt.%Fe and hyperperitectic Al-1.36wt.%Zr alloys in which intermetallic compounds Al_3Fe and Al_3Zr can be primarily formed in the melt during the solidification process are prepared in the present work. To better understand the possible effects on the Al_3Fe and Al_3Zr compounds by the high magnetic fields, the alloys are first solidified in the absence of magnetic field and then a clear determination of their crystallographic features by making use of EBSD technique is performed. Afterwards, the alloys are solidified under various intensities of high magnetic field to systematically investigate the influences of high magnetic field on their precipitation behaviors, including the distribution and alignment. As the conventional magnetic field influences the metallic alloys in a macroscopic scale, the isomorphous Al-9.8wt.%Zn and hypoeutectic Al-0.24wt.%Fe alloys are prepared and semi-continuously cast under conventional DC magnetic fields to experimentally examine the microstructural transformations and the accompanied crystal orientation change.

Reference

[1] Asai S, *Magnetohydrodynamics: Historical Evolution and Trends*, 2007, 80:315-327.

[2] Asai S, *Sci. Technol. Adv. Mater.*, 2000, 1:191-200.

[3] Watanabe K, Awaji S, *Jpn. J. Appl. Phys.* 1998, 37-38:L1148-L1150.

[4] Morikawa H, Sassa K and Asai S, *Mater. Trans. JIM*, 1998, 39:814.818.

[5] Taniguchi T, Sassa K, Yamada T and Asai S, *Mater. Trans. JIM*, 2000, 41:981-984.

[6] Tahashi M, Sassa K, Hirabayashi I and Asai S, *Mater. Trans. JIM*, 2000, 41:985-990.

[7] Ito M, Sassa K, Ogawa H, Doyama M, Yamada S and Asai S, *TANSO*, 2000, 191:37-41.

[8] Asai S, Sassa K and Tahashi M, *Sci. Technol. Adv. Mater.*, 2003, 4:455-460.

[9] Li B Q, *JOM-e*, 1998, 50:1-10.

[10] Jackson J D, Classical Electrodynamics, 2nd ed., New York: John Wiley & Sons, Inc. 1975.

[11] Gillon P, *Mater. Sci. Eng., A*, 2000, 287:146-152.

[12] Lehmann P, Moreau R, Camel D and Bolcato R, *Acta Mater.*, 1998, 46:4067-4079.

[13] Callen H B, *Phys. Rev.*, 1948, 73:1349-1358.

[14] Lakar O, Ph.D. Thesis, INPG, France, 1994.

[15] Nakada M, Mori K, Nishioka S, Tsutsumi K, Murakami H and Tsuchida Y, *ISIJ Int.*, 1997, 37:358-364.

[16] Gardin P, Galpin J-M, Regnier M-C and Radot J-P, *IEEE Trans. Magn.*, 1995, 31(3):2088-209.

[17] Uhlmann D R, Seward III T P and Chalmers B, *Trans. Metall. Soc. AIME*, 1966, 236:527-532.

[18] Ambardar R, *Aluminum*, 1986, 62:446-448.

[19] Youdelis W V and Dorward R C, *Can. J. Phys.*, 1966, 44:139-150.

[20] Youdelis W V and Cahoon J R, *Can. J. Phys.*, 1970, 48:805-808.

[21] Verhoeven J D and Pearson D D, *J. Mater. Sci.*, 1973, 8:1409-1412.

[22] Boettinger WJ, Biancaniello FS and Coriell SR, *Metall. Trans. A*, 1981, 12:321-327.

[23] Tewari S N, Shah R and Hui S, *Metall. Mater. Trans. A*, 1994, A25:1535-1544.

[24] Alboussiere T, Neubrand A C, *Magnetohydrodynamics*, 1995, 31:228-235.

[25] Alboussiere T, Neubrand A C, Garandet J P and Moreau R, *J. Cryst. Growth*, 1997, 181:133-44.

[26] Li B Q, *J. Mater. Process. Technol*., 1997, 71:402-413.

[27] Alboussiere T, Moreau R and Camel D, *C. R. l'Academie. Sci., Ser. II Univers*, 1991, 313:749-55.

[28] Moreau R, Laskar O, Tanaka M and Camel D, *Mater. Sci. Eng., A*, 1993, A173:93-100.

[29] Moreau R, Laskar O and Tanaka M, *Magnetohydrodynamics*, 1996, 32:173-177.

[30]Li X, Gagnoud A, Ren Z M, Fautrelle Y and Moreaub R, *Acta Mater.*, 2009, 57:2180-2197.

[31]Getselev Z N, *J. of Metals*, 1971, 23:38-59.

[32]Vives C, *Metall. Trans.*, 1989, B20:623-629.

[33]Vives C, *Metall. Mater. Trans.*, 1996, B27:445-455.

[34]Vives C, *Metall. Mater. Trans.*, 1996, B27:457-464.

[35]Zhang B J, Cui J Z and Lu G M, *J. Mater. Sci. Technol.*, 2002, 18:1-3.

[36]Zhang B J, Cui J Z and Lu G M, *Trans. Nonfer. Metals Soc. China*, 2002, 12:545-548.

[37]Dong J and Cui J Z, *Metall. Mater. Trans.*, 2004, 35:2487-2494.

[38]Guo S J, Cui J Z, Le Q C and Zhao Z H, *Mater. Lett.*, 2005, 59:1841-1844.

[39]Zhao Z H, Cui J Z, Dong J and Zhang B J, *J. Mater. Process. Technol.*, 2007, 182:185-190.

[40]Zhao Z H, Cui J Z, Dong J, Wang Z F and Zhang B J, *J. Alloys Compd.*, 2005, 396:164.168.

[41]Zhang B J, Cui J Z and Lu G M, *Mater. Lett.*, 2003, 57:1707-1711.

[42]Zuo Y B, Cui J Z, Dong J and Yu F X, *Mater. Sci. Eng.*, A, 2005, 408:176-181.

[43]Zuo Y B, Nagaumi H and Cui J Z, *J. Mater. Process. Technol.*, 2008, 197:109-115.

[44]Zuo Y B, Cui J Z, Dong J and Yu F X, *J. Alloys Compd.*, 2005, 402:149-155.

[45]Zuo Y B, Cui J Z, Zhao Z H, Zhang H T and Qin K, *Mater. Sci. Eng.*, A, 406:286-292.

[46]Mikelson A E and Karklin Y K, *J. Cryst. Growth*, 1981, 52:524.529.

[47]Savitisky E M, Torchinova R S and Turanoy S A J, *J. Cryst. Growth*, 1981, 52:519.

[48]Yasuda H, Tokieda K and Ohnaka I, *Mater. Trans. JIM*, 2000, 41:1005-1012.

[49]Rango P D, Lee M, Lejay P and Sulpice A, *Nature*, 1991, 349:770-772.

[50]Katsuki A, Tokunaga R, Watanabe S I and TanimotoY, *Chem. Lett.*, 1996, 25:607-608.

[51]Lu X Y, Nagata A, Watanabe K, Nojima T, Sugawara K, Hannda S and Kamada S, *Physica C*, 2002, 382:27-32.

[52]Chen W P, Maeda H, Kakimoto K, Zhang P X, Watanabe K, Motokawa M, Kumakura H and Itoh K, *J. Cryst. Growth*, 1999, 204:69-77.

[53]Li X, Fautrelle Y and Ren Z M, *Acta Mater.*, 2007, 55:5333-5347.

[54] Wang C J, Wang Q, Wang Z Y, Li H T, Nakajima K and He J C, *J. Cryst. Growth*, 2008, 310:1256-1263.

[55] Li X, Fautrelleb Y and Ren Z M, *J. Cryst. Growth*, 2007, 306:187-194.

[56] Li X, Ren Z M and Fautrelle Y, *J. Cryst. Growth*, 2008, 310:3488-3497.

[57] Liu T, Wang Q, Gao A, Zhang C, Li D G and He J C, *J. Alloys Compd.*, 2009, 481:755-760.

[58] Sassa K, Waki N and Asai S, In: Mishra B and Yamauchi C (eds), *Proceedings of Second Conference on Processing Materials for Properties, The Minerals, Metals and Materials Society,* San Francisco*,* 2000, p. 565.

[59] Wang Q, Wang C J, Pang X J and He J C, *Chin. J. Mater. Res.*, 2004, 18:568-576.

[60] Jin F W, Ren Z M, Ren W L, Deng K, Zhong Y B and Yu J B, *Sci. Technol. Adv. Mater.,* 2008, 9:1-6.

[61] Li X, Ren Z M and Fautrelle Y, *Mater. Des.*, 2008, 29:1796-1801.

[62] Wang Q, Lou C S, Liu T, Wei N, Wang C J and He J C, *J. Phys. D: Appl. Phys.*, 2009, 42:1-5.

[63] Lou C S, Wang Q, Wang C J, Liu T, Nakajima K and He J C, *J. Alloys Compd.*, 2009, 472:225-229.

[64] Michio S and Kei-ichi M, *Scripta Mater.*, 2000, 42:499-503.

[65] Sadovskii V D, Rodigin N M, Smirnov L V, Filonchik G M and Fakidov I G, *Fiz. Met. Metalloved.*, 1961, 12:131-133.

[66] Krivoglaz M A and Sadovskiy V D, *Fiz. Met. Metalloved.*, 1964, 18:23-27.

[67] Tahashi M, Sassa, K, Hirabayashi I and Asai S, *Mater. Trans. JIM*, 2000, 41:985-990.

[68] Taniguchi T, Sassa K, Yamada T and Asai S, *Mater. Trans. JIM*, 2000, 41:981-984.

Chapter 2 Crystallographic features of primary Al_3Fe and Al_3Zr phases in as-cast Al-based binary alloys

2.1 Introduction

The core content of the present dissertation is to investigate the effects of high magnetic field and conventional DC magnetic field on the crystallography and microstructure of Al-based binary alloys. In the high magnetic field experiments, it mainly refers to the modification of the precipitation behaviors of the primary Al_3Fe and Al_3Zr phases during the solidification of Al-Fe and Al-Zr. As the precipitation behaviours of these two phases are intimately correlated with their crystallographic structures, a systematic study in advance on their crystallographic features in the absence of magnetic field will contribute to the understanding of the effects brought by the high magnetic field. To show a clear text structure, we present their crystallographic features in a single chapter.

Table 2.1 Crystallographic data of Al_3Fe and Al_3Zr crystals

Formula	Structure	Number of atoms in the unit cell	Lattice parameters				Space group	No.
			a	b	c	β		
Al_3Fe	monoclinic	102	1.549 nm	0.808 nm	1.248 nm	107.72°	C2/m	12
Al_3Zr	tetragonal	16	0.3998 nm		1.728 nm	90°	I4/mmm	130

Iron and zirconium are two important additives in the production of aluminium-based alloys as they can improve some certain properties of the alloys [1-3]. As a consequence, intermetallic compounds Al_3Fe (sometimes denoted as $Al_{13}Fe_4$, $Al_{19}Fe_6$ or Al_7Fe_2) and Al_3Zr often emerge in these alloys. Al_3Fe compound has a direct impact on the formability and fatigue resistance of Al-Fe alloy [4]; whereas Al_3Zr is of interest for potential aerospace applications due to its low density, high melting point and large elastic modulus [5]. So far, their basic physical properties have been widely reported [4], such as density, linear expansion coefficient, electric resistively, thermal conductivity, etc. Their crystal structures have also been well identified, as shown in Table 2.1 [6, 7]. Their some correlated crystallographic features have also been partly studied and detailed as follows.

For Al_3Fe compound, it has been proved that it has a strong tendency to twin. Groth [8]

was the first to observe (100) and (001) reflection twins. Black [9, 10] suggested (100) and (001) glide twin models. Fung et al. [11] confirmed that the (20-1) twinning is another possibility. Ma et al. [12] reported an investigation on (001) microtwins. Some other researchers [13-15] also did some work in revealing the twins in Al_3Fe compound. However, a complete study combining twinning with their morphologies on the primary Al_3Fe phase during the solidification of Al-Fe hypereutectic alloy has not been well addressed. Moreover, a clear description of the twinning mode with the complete set of twinning elements for the twins formed in this crystal has also not been reported.

For Al_3Zr compound, it has been determined in a slowly cooled Al-10wt.%Zr melt that the fully grown primary Al_3Zr crystals are tabular and bound by {001} and {101} facets [16]. Moreover, (1-1-4) twin was also found in this compound [17]. However, a more complete study involving the morphology of the primary Al_3Zr crystal in the cause of growth has not been addressed. A clear description of the twinning mode with the complete set of twinning elements for the twin formed in this compound has not been reported. The effect of twining on the morphology of the crystal and the twinning formation mechanism in atomic scale has also not been analyzed.

Based on the background above, Al-3.3wt.%Fe and Al-1.36wt.%Zr alloys were selected and solidified to form primary Al_3Fe and Al_3Zr phase in the present work. A systematic study on the crystallographic aspects of these two compounds was carried out to obtain the useful information.

2.2 Experimental

The Al-3.31wt.%Fe (or Al-1.36wt.%Zr) alloy was prepared by melting high-purity aluminum (99.999wt.%) and iron (99.99wt.%) (or zirconium (99.999wt.%)) in an induction furnace. After magnetically stirred and held at 850°C (or 1100°C for Al-1.36wt.%Zr) for 30min, a further mechanical stirring is applied to make the alloy composition homogeneous in the whole melt and then the melt was poured into a high-purity water-cooled copper crucible ($20\times100\times100mm^3$) to be solidified quickly. A rod was cut from the billet, and then put into a tube of high-purity corundum crucible (10mm in inner diameter and 30 mm in height). The crucible with the rod was placed in a vacuum resistance furnace for solidification experiment.

After the pressure in the furnace reached 5×10^{-3} Pa, the rod was heated up to 830 °C (or 980 °C for Al-1.36wt.%Zr) by an electric heater at a heating rate of 5°C/min and held at this temperature for 40 min, and then cooled to room temperature at a cooling rate of 10 °C/min (or 12°C/min for Al-1.36wt.%Zr).

A specimen was cut longitudinally (or transversely for Al-1.36wt.%Zr) from the as-cast sample and then polished for further examination. The microstructure was observed with a Leica DMR optical microscope. Individual orientation measurements of the primary Al_3Fe (or Al_3Zr) phase were performed at manually chosen points through acquiring and indexing their EBSD Kikuchi patterns with a JOEL JSM 6500 FE-SEM, equipped with the software HKL Channel 5 – Oxford.

The principal crystallographic extension directions of the primary Al_3Fe phase were determined first by searching the longest Al_3Fe crystals in the sampling plane on hypothesis that these crystals may have their extension direction close to the observed plane. Then measure their longest interface trace vectors in the sample coordinate system and calculate their equivalent vectors in the crystal coordinate with the measured orientation of the crystals. Finally the statistically representative crystalline direction close to these trace vectors is determined as the crystallographic extension direction. Twin orientation relationships for both of Al_3Fe and Al_3Zr crystals were first determined by misorientation calculations expressed by rotation angles and axes [18], then the corresponding twinning elements ($\boldsymbol{K_1}$ - the twinning plane; $\boldsymbol{\eta_1}$ - the twinning direction; $\boldsymbol{K_2}$ - the reciprocal or conjugate twinning plane; $\boldsymbol{\eta_2}$ - the reciprocal or conjugate twinning direction; $\boldsymbol{P}$ - the plane of shear; s - the amount of shear) were completely determined according to the minimum shear criterion and the Bilby–Crocker theory [19]. The faceted Al_3Fe-matrix (or Al_3Zr-matrix) interfaces are identified by trace analysis and calculated with the indirect two-trace method developed by our group [20].

2.3 Results and discussion

2.3.1 Al-3.31wt.%Fe alloy

Fig. 2.1(a) shows the microstructure in the longitudinal section of the specimen. It can be seen that the primary Al_3Fe phase (gray bars) whose crystal structure is confirmed by indexing its EBSD Kikuchi patterns with the data in Table 2.1 are embedded in the eutectic matrix and

displays two forms of morphologies – straight and bent (enclosed in the rectangular frame). Here, it should be emphasized that the occurrence frequency of the bent Al_3Fe crystal is very low.

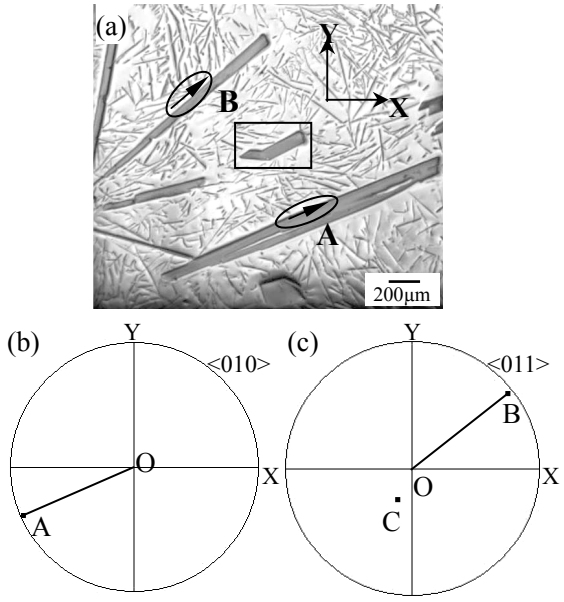

Figure 2.1 (a) Microstructure in the longitudinal section of the specimen; (b) stereographic projection of <010> of crystal A and (c) stereographic projection of <011> of crystal B on the microstructure observation plane. Axis X and Y represent the 2D coordinate system of the microstructure observation plane. Dot C in (c) is another pole from the <011> family.

Fig. 2.1(b) and (c) show stereographic projections of <010> and <011> of the respective crystals A and B (Fig. 2.1(a)) on the microstructure observation plane. From the interface traces of the primary Al_3Fe crystals (enclosed in the circles) in the microstructure, it can be observed that the crystals well extend in the arrowed directions. In the projection figures, the projection lines of the <010> (Line OA) and <011> (Line OB) are very close to the true <010> and <011> crystal lines as their poles are close to the outer circle of the stereographic projections. Moreover, these projection lines are also, respectively, very close to the longest interface traces, i.e. the principal extension directions (see the black arrows in Fig. 2.1(a)) of the Al_3Fe crystals, suggesting that the primary Al_3Fe phase has two preferred crystallographic extension directions – <010> and <011> (here, it should be mentioned that the <010> direction has a deviation of less than 3 degrees from the longest interface trace of the crystal). A statistical examination indicates that the occurrence frequency of <010> extension is a little

lower than that of <011> (2:3) and there is no obvious morphological difference between the two directionally extended crystals. The choice of extension direction of a primary Al_3Fe crystal may be related to the intrinsic interfacial energy anisotropy, local solute and temperature field and initial orientation of the nucleation.

Further crystallographic orientation analyses indicate that most of the primary Al_3Fe crystals are twinned. As an example, Fig. 2.2(a) shows the SEM image of a twinned primary Al_3Fe crystal that extends in <010> direction (the extension direction is shown with its corresponding <010> stereographic projection on the observation plane). The contrast

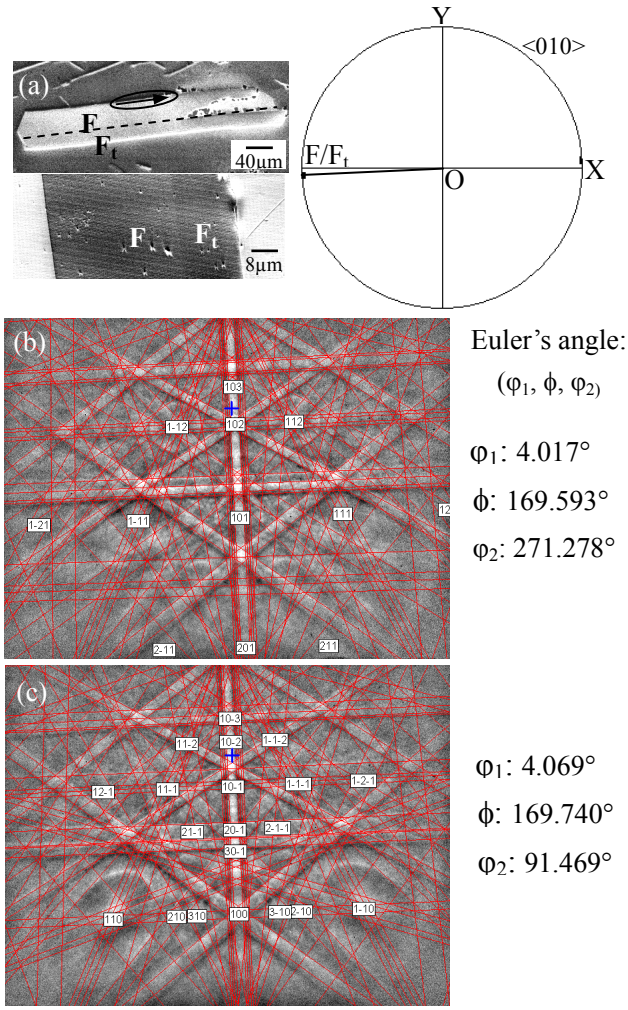

Figure 2.2 (a) SEM image of a twinned primary Al_3Fe crystal extending along <010> and the <010> stereographic projection on the observation plane of crystals F and F_t; the zoom BES image on the right part displays the contrast between the two interrelated crystals. (b) and (c) indexed EBSD Kikuchi patterns of F parent and F_t twin, respectively. φ_1, ϕ and φ_2 represent the set of rotations from the sample coordinate system to the crystal coordinate system of the two crystals.

variation between F parent and its twin F_t is also displayed in the zoom BSE (Back Scattered Electron) image below the SEM image (a rotation of 90° to the SEM image). Based on this BSE image, a dashed line is artificially added to mark the separation between F and F_t. A pair of indexed EBSD Kikuchi patterns from the parent F and its twin F_t are displayed in Fig. 2.2(b) and 2(c), evidencing the existence of the orientation change. The orientations of the two crystals represented with a set of rotations parameterized with Euler angles in Bunge notation [21] from the sample coordinate system to the crystal coordinate system are also given in the figure. Statistical examination of all the Al_3Fe crystals appearing in the entire longitudinal sample section shows that there are two sorts of twins. Hereafter they are denoted

Table 2.2 Misorientation angles and rotation axes between the two twinned parts in Twin 1 and Twin 2. The distinct rotation axis of each rotation angle is expressed in the coordinates in the orthonormal crystal coordinate system and in Miller indices in the monoclinic basis. The Miller indices of the plane normal to the rotation axis are also displayed.

	Misorientation angle , ω (°)	Coordinates of rotation axes, **d**			Miller indices of the rotation axes, [u v w]			Planes normal to the rotation axes, (h k l)		
		d_1	d_2	d_3	u	v	w	h	k	l
Twin 1	179.9	0	0	9.999	0	0	1	-1	0	3
	179.8	9.999	0	0	3	0	1	1	0	0
Twin 2	179.6	3.028	0	9.530	1	0	4	0	0	1
	179.9	-9.530	0	3.028	-1	0	0	-4	0	1

Table 2.3 Twinning elements for Twin 1and Twin 2

	Twin 1	Twin 2
K_1	(100)	(001)
η_1	[001]	[-0.0097, 0.5, 0]
K_2	(001)	(0.0159, 0.4034, 0.0969)
η_2	[100]	[1-14]
P	(010)	(0.2830, 0.0055, -0.0690)
s	0.6390	0.3403

Twin 1 and Twin 2. In the case of <010> extension, only Twin 1 is observed; whereas in the case of <011> extension, both Twin 1 and Twin 2 are detected. The two sorts of twins were first examined by misorientation calculations. Due to the monoclinic symmetry, there are two sets of misorientations, each set being defined by a misorientation angle ω and the corresponding family of rotation axes, i.e. two rotation axes. The distinct rotation axis for

each misorientation is first expressed with the coordinates in the orthonormal crystal coordinate system **d** (d_1, d_2, d_3) and then expressed with Miller indices [u v w] in the monoclinic basis. The coordinate transformation between the orthonormal crystal coordinate system and the monoclinic basis conforms to the Channel 5 convention. The misorientation calculation results for Twin 1 and Twin 2 are given in Table 2. The Miller indices (h k l) of the plane normal to the rotation axis are also calculated. It should be noted that due to the experimental errors, the calculated rotation axes do not have exact rational Miller indices, i.e. integers, but the deviation is very small, within 2°. It is seen from Table 2.2 that there are two 180° rotations for each sort of twin (Twin 1 and Twin 2), confirming that the two misoriented crystals are twin related according to the classical definition of twinning [22]. The corresponding plane normal to the rotation axis could be the twinning plane $\boldsymbol{K_1}$ and the rotation axis could be the twinning direction $\boldsymbol{\eta_1}$. This means that there are four possible twinning modes for each twin. All the twinning elements for each twinning mode are calculated. The mode that requires the smallest twinning shear is determined as the valid twinning mode for each sort of twin and the corresponding twinning elements are shown in Table 2.3. According to the established nomenclature, twinning can be classified into 3 modes according the rationality of the Miller indices of the twinning elements. Rational $\boldsymbol{K_1}$ and $\boldsymbol{\eta_2}$ correspond to type I and rational $\boldsymbol{K_2}$ and $\boldsymbol{\eta_1}$ type II. If all the four elements are rational, it is compound. As can be seen in Table 2.3, for Twin 1, all the twinning elements have rational indices, indicating that this twin is compound; whereas for Twin 2, only $\boldsymbol{K_1}$ and $\boldsymbol{\eta_2}$ are rational, therefore it belongs to type I twin. Twinning element calculation result indicates that the twin in Fig. 2.2(a) belongs to Twin 1.

The crystallographic extension direction and twinning have a direct influence on the morphologies of the primary Al_3Fe phase. Fig. 2.3(a) and (b) show two other twinned primary Al_3Fe crystals and (c) and (d) their corresponding <011> stereographic projections on the observation plane indicating their extension directions. Twinning element calculation result indicates that the twins in these two crystals belong to Twin 1 and Twin 2, respectively. Fig. 2.3(e) and (f) show the standard stereographic projections of the twinning elements corresponding to these two twinned crystals. From the three twinned primary crystals

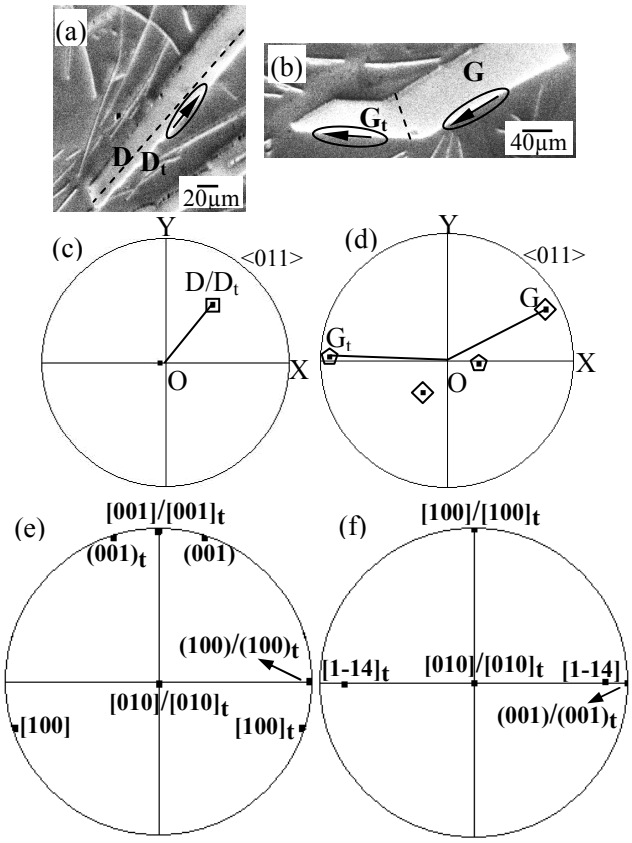

Figure 2.3 SEM images of two twinned primary Al_3Fe crystals extending along <011> but with a (a) straight and (b) bent morphology; <011> stereographic projections on the observation plane corresponding to (c) D and D_t and (d) G and G_t; standard stereographic projections of the twinning elements corresponding to (e) D and D_t and (f) G and G_t. The poles enclosed in the same shaped frames in (c) and (d) are from the same part of the crystal.

mentioned above, it is seen that the crystals extending in <010> (Fig. 2.2(a)) and <011> (Fig. 2.3(a)) with Twin 1 are long and straight, while that extending in <011> with Twin 2 (Fig. 2.3(b)) is bent. Actually for the long and straight morphology, the <010> and <011> directions are in the $\boldsymbol{K_1}$ plane, while for the bent morphology, the extension direction <011> is not in the $\boldsymbol{K_1}$ plane. It is known that $\boldsymbol{K_1}$ (i.e. twinning plane) is an invariant plane. If the extension direction is in the $\boldsymbol{K_1}$ plane, the two twinned parts share one and the same extension direction; therefore, twinning has no influence on the morphology during extension. However, if the extension direction is out of the $\boldsymbol{K_1}$ plane, the two twinned crystals cannot extend in the same direction, thus a bent morphology appears.

Morphology examination shows that the primary Al_3Fe crystals possess regular shape and the interface traces are always straight, suggesting that the crystal may expose faceted

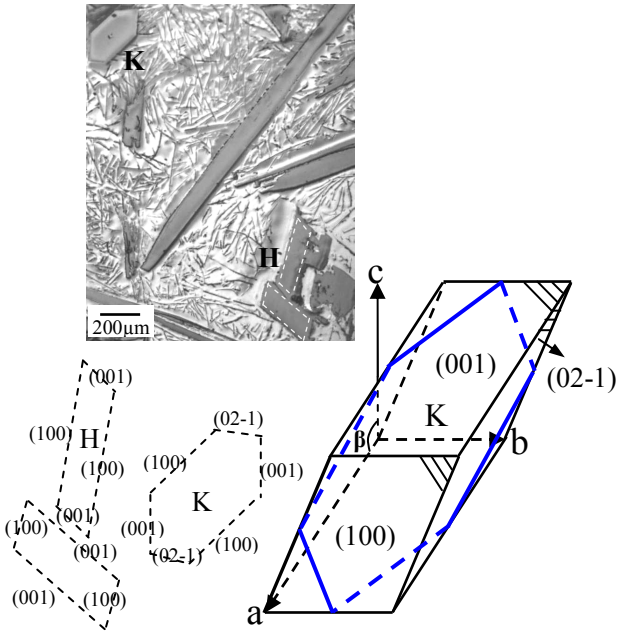

Figure 2.4 Microstructure indicating two shapes of intersection of Al_3Fe crystals with the sampling plane. Crystal H: monoclinic prism; Crystal K: triclinic prism. The schemes show the indices of the surface planes binding crystals H and K and the blue lines outline the intersection between the crystal and the sampling plane. Axes a, b and c represent the monoclinic crystal basis of the Al_3Fe.

low-index planes to the Al matrix. Two shapes of intersection of the Al_3Fe crystals are observed, as indicated in Fig. 2.4, parallelogram (crystal H) and hexagon (crystal K). It should be noted that as the sampling plane is not always perpendicular to the interfaces of these crystals, the angles between the adjacent interface traces in the figure do not correspond to the true angles between the interfaces. As can be seen, crystal H is bound by two pairs of parallel surface planes (see the white frames), whereas crystal K is bound by three pairs of parallel surfaces. Calculation shows that for the crystals having parallelogram intersection (crystal H), the surface planes are (100) and (001); while for those having hexagonal intersection (crystal K), the surface planes are (100), (001) and (02-1). Examining the angles between the adjacent interfaces, the three-dimensional form of the crystals can be obtained. Those having a parallelogram intersection (crystal H in Fig. 2.4) are in a form of monoclinic prism and the (100) and (001) planes are parallel to the extension direction; whereas those having a hexagonal intersection (crystal H in Fig. 4) are in triclinic prism, as illustrated in Fig. 2.4. The intersection between the sampling plane and the crystal is outlined in blue in Fig 2.4. For such crystals, they do not display an evident extension direction. Moreover, the crystals in the form

of monoclinic prism always possess Twin 1; whereas those in the form of triclinic prism possess Twin 2. According to the current crystal growth theories [23], crystals are bound by low-index faces. Obviously, the planes identified above are low-index ones. The identification of these planes is very helpful for the understanding of the formation of the two sorts of twins. During the growth process of a primary Al_3Fe crystal, its (100) and (001) planes may expose to the Al melt. Under the help of a convection, a stacking fault with respect to the (100) or (001) plane may occur when the iron and aluminium atoms attach to it, and thus giving rise to the formation of Twin 1 or Twin 2. Interestingly, it is found that for the crystals that are twinned by Twin 2, the twinned crystals have the (02-1) plane in common, therefore, twinning during the growth process does not change their external shape.

2.3.2 Al-1.36wt.%Zr alloy

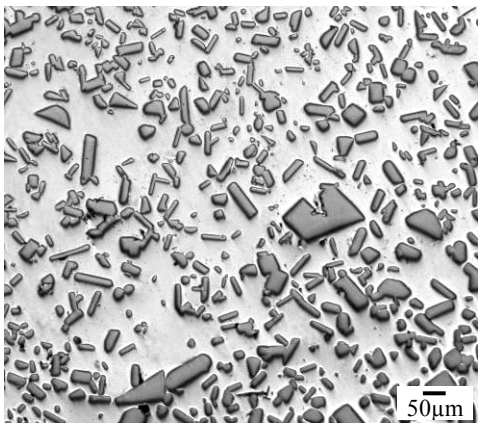

Figure 2.5 Microstructure in the transverse section of the ingot.

Fig. 2.5 shows the microstructure in the transverse section of the ingot. It is seen that the primary Al_3Zr crystals (gray color) – whose crystal structure is confirmed by indexing the EBSD Kikuchi patterns with the data in Table 2.1 – are embedded in the Al matrix. Fig. 2.6(a) and (b) show two typical longitudinal cuts of the primary Al_3Zr crystals and (c) displays one cross section, which indicates that the Al_3Zr crystal has a tabular shape. It is found that the shape of the longitudinal cut is size dependent. When the size of the crystal is relatively small, i.e. in the course of growth, the longitudinal cut appears in octagonal form (Fig. 2.6(a)); whereas when the size is large, i.e. after full growth, most of the crystals appear in a rectangular form (Fig. 2.6(b)). In both cases, the interface traces are straight, suggesting that

the crystals expose faceted planes to the Al matrix.

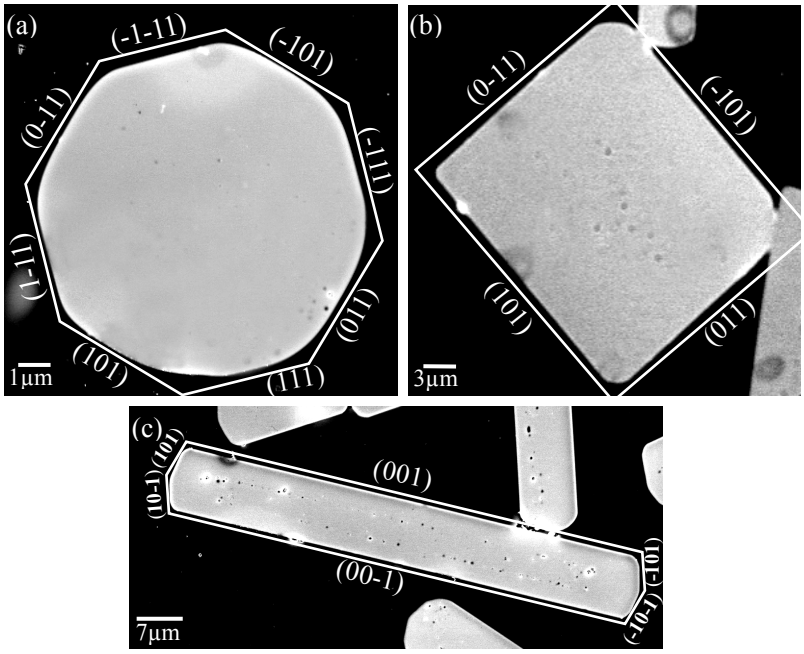

Figure 2.6 Longitudinal cuts of the primary Al_3Zr crystals in (a) octagonal and (b) rectangular form; (c) one cross section of the tabular primary Al_3Zr crystal.

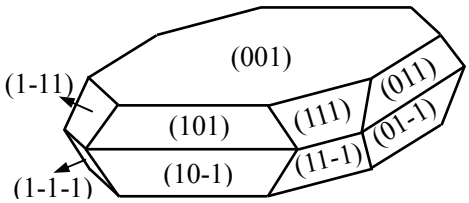

Figure 2.7 Three-dimensional schematic morphology of the Al_3Zr crystal with an octagonal shape in the longitudinal cut.

Al_3Zr-matrix interface calculation results indicate that for the two shaped crystals, the two large upper and lower plate surfaces correspond to the {001} planes, whereas for the smaller sized plates, the lateral surfaces correspond to two families of planes {101} and {111}, as illustrated in Fig. 2.7 , but for the larger sized plates, the lateral surfaces correspond to only one family of planes {101}.

It is known that the final shape of a faceted crystal is determined by the migration capacity (or rate) of its facets during the growth process and the migration capacity of a facet is related to its atomic scale roughness. Atoms more easily attach to rough planes than to smooth ones as rough planes have more vacant sites to accept atoms during the growth process. As a consequence, rough planes migrate faster than the smooth ones and finally the

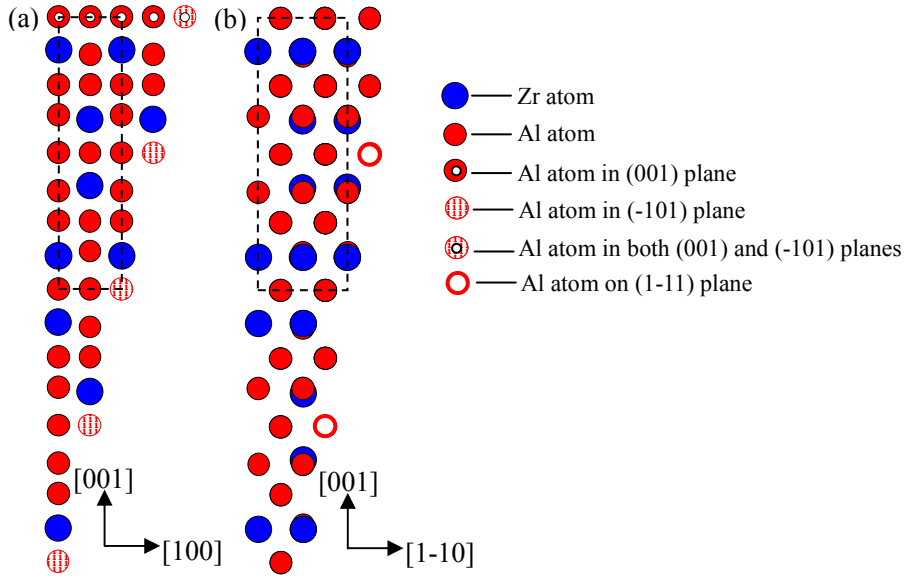

Figure 2.8 Projection of the Al and Zr atoms of the Al_3Zr crystal with (010) and (-101) (a) and (1-11) (b) on edge-on position (i. e. these planes are perpendicular to the projection plane). The unit cell is enclosed in the dashed rectangular frame in each figure.

fully grown crystal will only be enclosed by slowly migrating interfaces. In the present work, the faceted primary Al_3Zr crystals should also obey this rule. Fig. 2.8(a) show the projection of Al and Zr atoms of the Al_3Zr crystal with (001), (-101) and (1-11) on edge-on position (i.e. the three planes are perpendicular to the projection plane) to illustrate the roughness of these planes at the atomic scale. It can be seen that the (001) (Fig. 2.8(a)) has a high crystalline perfection, therefore, the atoms do not attach easily to this plane. As a consequence, (001) has a low migration rate during the growth process. Therefore, the growth of the crystal is mainly realized by the migration of the lateral interfaces (i.e. {101} and {111} planes), which results in a tabular shape as a whole for the primary Al_3Zr crystals. Compared with (001) plane, the (-101) (Fig. 2.8(a)) and (1-11) (Fig. 2.8(b)) planes are quite rough, containing steps or vacancies at the atomic level that can help to capture atoms during the growth process. However, the roughness of these two planes are also not exactly the same. The (-101) plane contains regular lateral steps which are still relatively smooth, whereas the (1-11) exhibits many irregularly sited vacancies which make the interface quite rough. Therefore, the (1-11) has a higher migration rate than the (-101). Finally, lateral planes from the {111} family disappear and only those from the {001} family and from the {101} family remain through the full growth process, and hence most fully grown Al_3Zr primary crystals possess a

rectangular shape in the longitudinal sections.

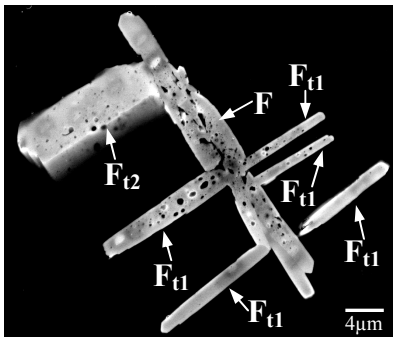

Figure 2.9 Dendritic primary Al_3Zr crystal with twin formed.

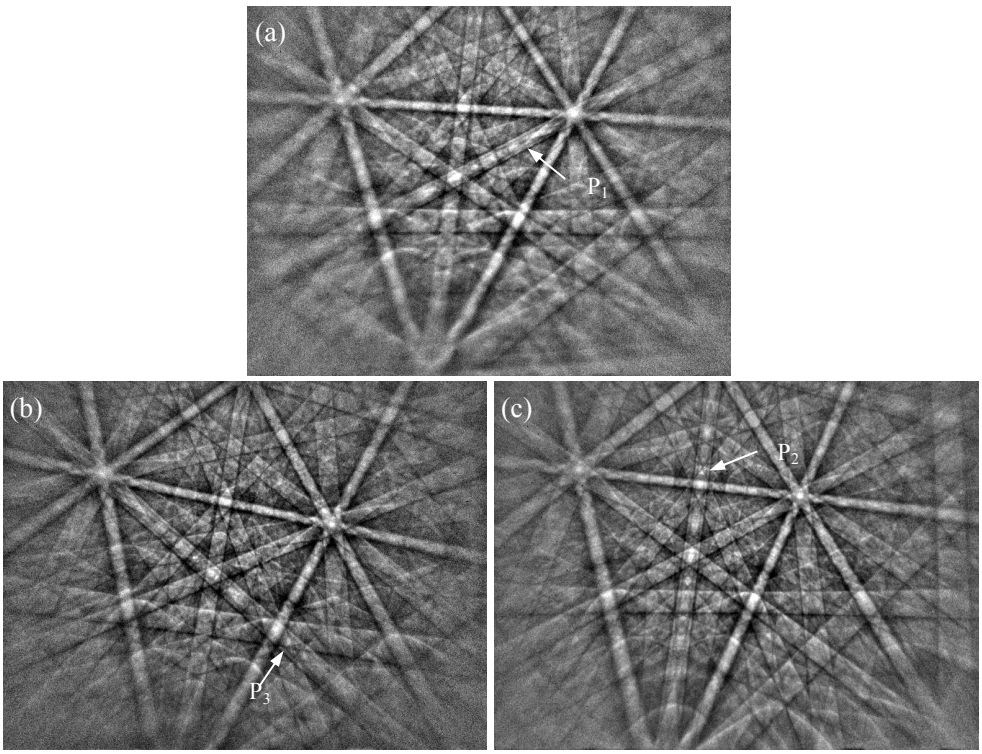

Figure 2.10 EBSD Kikuchi patterns corresponding to (a) F, (b) F_{t1} and (c) F_{t2} parts in Fig. 2.9, respectively.

Table 2.4 Misorientation angles and rotation axes between the two twinned parts. The distinct rotation axis of each rotation angle is expressed in the coordinates in the orthonormal crystal coordinate system and in Miller indices in the tetragonal basis. The Miller indices (h k l) for ω = 178.958° and [u v w] for ω = 176.608° are not given as they are irrational.

Twin between	Misorientation angle, ω (°)	Coordinates of rotation axes, **d**			Miller indices of the rotation axes, [u v w]			Planes normal to the rotation axes, (h k l)		
		d_1	d_2	d_3	u	v	w	h	k	l
F and F_{t1}	178.958	0.6783	0.0296	0.7342	4	0	1	–	–	–
	176.608	-0.7345	-0.0091	0.6785	–	–	–	-1	0	4

Table 2.5 Twinning elements.

Twinning elements	K_1	η_1	K_2	η_2	P	s
	(-104)	[401]	(104)	[40-1]	(010)	0.155

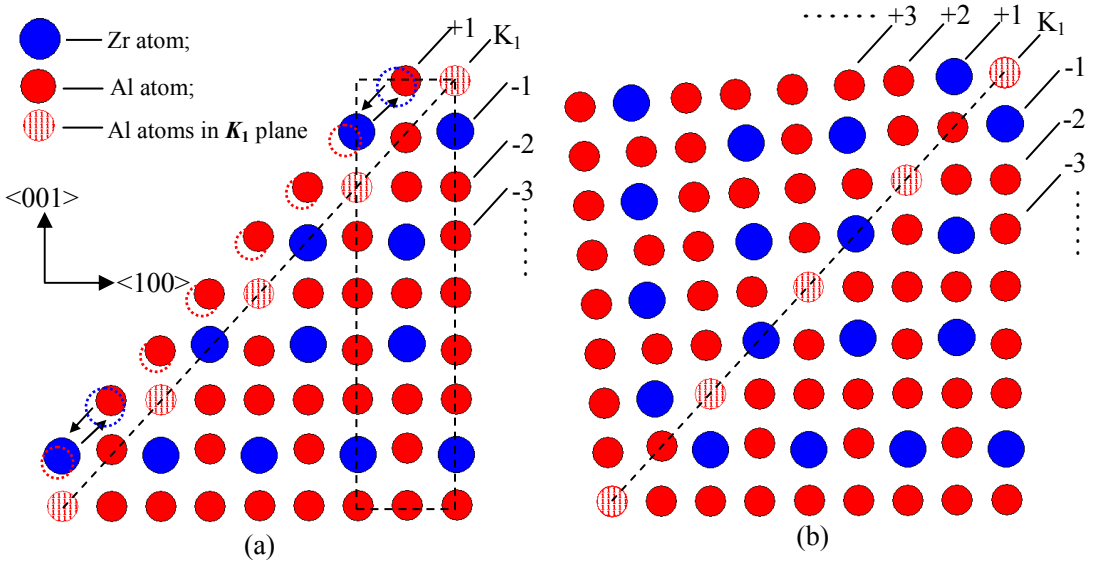

Figure 2.11 Position of the atoms and trace of the K_1 plane in the shear plane in the (a) untwinned and (b) twinned crystal, respectively. The unit cell is enclosed in the dashed rectangular frame.

Further observation indicates that other than the above mentioned tabular primary Al_3Zr crystals, there exists another shape of the Al_3Zr crystals – in dendritic form, as shown in Fig. 2.9, although the occurrence is relatively low. It is seen from Fig. 2.9 that some secondary arms F_{t1} and F_{t2} branch off from the primary trunk F perpendicularly. EBSD orientation measurements evidence that the crystallographic orientations of the primary trunk F and the secondary arms F_{t1} and F_{t2} are not the same, as indicated by their Kikuchi patterns in Fig. 2.10. As seen in the figures, the orientation difference is characterized by the position change of the "supercell diffraction lines" arrowed (P_1, P_2 and P_3) in the figures. Misorientation calculation shows that F-F_{t1} and F-F_{t2} each possesses a pair of near 180° rotations, each corresponding to a set of eight equivalent rotation axes, suggesting that the two pairs of crystals are twin related. For the two pairs of crystals, the 180° rotation axes belong to the same family, indicating that they possess the same kind of twin. The distinct rotation axis for each misorientation is first expressed with the coordinates in the orthonormal crystal coordinate

system **d** (d_1, d_2, d_3) and then with Miller indices [u v w] in the tetragonal basis. The Miller index (h k l) of the plane normal to the rotation axis is also calculated. The misorientation calculation results are given in Table 2.4. Following the minimum shear criterion, the full set of twinning elements are determined and shown in Table 2.5. It is seen that the twin belongs to compound twin as all the twinning elements have rational indices. Detailed atomic correspondence examination indicates that the formation of this crystal twin requires lattice shear defined by the twinning elements given in Table 2.5 plus local atom stacking fault accompanied by local atomic reshuffling. Fig. 2.11(a) and (b) show the position of the atoms and trace of the $\boldsymbol{K_1}$ plane in the shear plane in the untwinned and twinned crystal, respectively. In the figures, the -1, -2… planes are in the matrix; the +1, +2… planes in the twinned part and $\boldsymbol{K_1}$ is the invariant twinning plane. For simplicity of the explanation of the twin formation process, we suppose that the twinned part of crystal is formed by the motion of the interface from the matrix to the twinned part. As the two parts of the crystal are in compound twin relationship, they should be in mirror symmetry with respect to the invariant K_1 plane, as illustrated in Fig. 2.11(b). Therefore, the formation of the +1 plane requires the lattice shear to displace the atoms in this layer to be in mirror symmetry to those on the -1 plane with respect to the $\boldsymbol{K_1}$ plane accompanied by local atomic reshuffling plus local position exchanges between the Zr atom with a neighbouring Al atom, as illustrated in Fig. 2.11(a). The lattice shear could be due to external disturbance (e.g. convections in the melt) during the attachment of the atoms from the melt to the solidified Al_3Zr crystal and the position exchange between the Zr atom with a neighbouring Al atom realized by a local atomic stacking fault. Once the +1 layer is formed, the growth of the twinned part follows the stacking sequence of the twinned crystal, as indicated in Fig. 2.11(b). As the twinned crystal is oriented differently with respect to the matrix, the growth direction is also reoriented away from that of the matrix. This reorientation could be the origin of the secondary arms growing off from the matrix (Fig. 2.9). It should be noted that the position exchange between the Al and the Zr atoms should be very difficult once the crystal is formed. This suggests that the observed twinning is a typical growth twinning.

2.4 Conclusions

Al-3.3wt.%Fe and Al-1.36wt.%Zr alloys were solidified to form primary Al_3Fe and Al_3Zr phases. The crystallographic features of these two phases are investigated.

For the bar-shaped primary Al_3Fe crystals, their preferred crystallographic extension directions have been identified as <010> or <011>. Two sorts of twins are detected and their complete twinning elements determined. The morphologies related to the crystallographic extension direction and twinning are analyzed. The Al_3Fe crystals are in two forms, the form of monoclinic prism and the triclinic prism. Type I twin can give rise to the formation of bent crystals. The crystallographic planes of their surfaces are identified as (100) and (001) in the extension direction for the monoclinic prism and (001), (001) and (02-1) for the triclinic prism. The formation of the twins is related to the (001) and (001) planes exposing to the Al melt during the growth.

For the tabular primary Al_3Zr crystals, two forms of longitudinal cuts are observed - octagonal (smaller sized) or rectangular (larger sized). The surface planes binding the smaller (or larger) sized crystals are crystallographically determined as {001}, {101} and {111} (or {001} and {101}). Dendritic crystals related to the formation of two compound twins are observed, and the complete twinning elements for these two twins are also determined. The tabular shape of the primary crystals is attributed to the low roughness of {001} planes. The disappearance of {111} planes in the larger sized crystals result from their high roughness. The twin formation is realized by lattice shear plus local atom stacking fault accompanied by local atomic reshuffling.

Reference

[1] Belov N A, Aksenov A A and Eskin D G, Iron in aluminum alloys: impurity and alloying element, Taylor & Francis, London and New York, 2002.

[2] Allen C M, Kumar S, Carrol L, O'Reilly K A Q and Cama H, *Mater. Sci. Eng. A*, 2001, 304.306:604.607.

[3] Litynska L, Abou-Ras D, Kostorz G and Dutkiewicz J, *J. Microsc. (Oxf.)*., 2006, 223:182-184.

[4] Mondolfo L F, Aluminum alloys: structure and properties, Butterworth, London, 1976.

[5] Miao W, Tao K, Li B and Liu B X, *J. Phys. D: Appl. Phys.*, 2000, 33:2300-2303.

[6] Barlock J G and Mondolfo L F, *Z. Metall.*, 1975, 66:605-611.

[7] Ma Y, Gjonnes J and Tafto J, *Micron Microsc. Acta*, 1991, 22:163-164.

[8] Groth P, Cheniische Kristallographie, Erster Tcil, Wilhelm Engelmann, Leipzig, 1906.

[9] Black P J, *Acta Cryst*., 1955, 8:175-182.

[10] Black P J, *Acta Cryst.*, 1955, 8:43-48.

[11] Fung K K, Zou X D and Yang C Y, *Philos. Mag. Lett.*, 1987, 55:27-32.

[12] Ma X L**,** Liebertz H and Koster U, *Phys. Stat. Sol. (a)*, 1996, 158:359-367.

[13] Tsuchimori M, Ishimasa T and Fukano Y, *Phil. Mag. B*, 1992, 66:89-108.

[14] Ellner M and Burkhardt U, *J. Alloys Comp.*, 1993, 198:91-100.

[15] Saito K, Sugiyama K and Hiraga K, *Mater. Sci. Eng.*, 2000, 294.296:279-282.

[16] Zhen S and Davies G J, *J. Cryst. Growth*, 1983, 64:407-410.

[17] Zhao Y T, Cheng X N, Dai Q X, Cai L and Sun G X, *Mater. Sci. Eng. A*, 2003, 360:315-318.

[18] Cong D Y, Zhang Y D, Wang Y D, Esling C, Zhao X and Zuo L, *J. Appl. Cryst.*, 2006, 39:723-727.

[19] Bilby B A and Crocker A G, *Proc. R. Soc. London, Ser. A*, 1965, 288:240-255.

[20] Zhang Y D, Esling C, Zhao X and Zuo L, *J. Appl. Cryst.*, 2006, 40:436-440.

[21] Bunge H J, Esling, C and Muller J, *J. Appl. Cryst.*, 1980, 13:544-554.

[22] Christian J W and Mahajan S, *Prog. Mater. Sci.*, 1995, 39:1-157.

[23] Prywer J, *Eur. Phys. J.*, 2002, B25:61-68.

Chapter 3 Effect of high magnetic field on the precipitation behaviors of primary Al_3Fe and Al_3Zr phases during the solidification of Al-based binary alloys

3.1 Introduction

High magnetic field has been widely employed in various material processes, such as phase transformation [1], vapour-deposition [2], electro-deposition [3] and magnetic slip casting [4]. Solidification, as one of the most important processes for metallic alloys, also did not let it wait, and made it involved actively. So far, many interesting effects have been found since it was applied during this process. One of the most important elements in inducing these phenomena and effects results from the magnetization force, which is usually classified into two different kinds – one is by which materials are rotated to a magnetic field direction as a compass rotates to the north direction, and the other is by which ferromagnetic and paramagnetic materials are pulled to a magnet and the diamagnetic ones are repulsed [5]. During the solidification process, these two kinds of forces play different roles in affecting the macro- and microstructures of the metallic alloys – the former can rotate the crystals with obvious magnetic anisotropies in the melt to generate crystallographic alignment and thus to create macroscopic texture [6-17]; whereas the latter can modify the distribution of the related phases [18-23]. Besides the magnetization force, the induced Lorentz force and thermoelectric magnetic force (TEMF) are also two important elements in affecting the macro- and microstructures of the alloys.

Nowadays, aluminium-based alloy manufacturing industry has become one of most important pillar industries all over the world; therefore how to improve the properties of aluminium-based alloys has attracted much attention in field of materials science. Among these alloys, as already mentioned previously, iron and zirconium are often used as additives and thus results in the formation of the intermetallic compounds Al_3Fe and Al_3Zr. These two compounds are intimately correlated to the final properties of the metallic alloys, so it is of importance to study their characters. As high magnetic field can induce various effects during the solidification process of metallic alloys, introducing a high magnetic field to the solidification process of binary Al-Fe and Al-Zr alloys may modify the precipitation

behaviors of the primarily precipitated Al_3Fe and Al_3Zr phase. Based on this, Al-3.3wt.%Fe and Al-1.36wt.%Zr (and Al-1.95wt.%Zr) alloys were selected and solidified under various high magnetic fields in the present work. A systematic study of the effects of the magnetic field on the precipitation behaviors of the primary Al_3Fe and Al_3Zr phase is carefully carried out.

3.2 Experimental

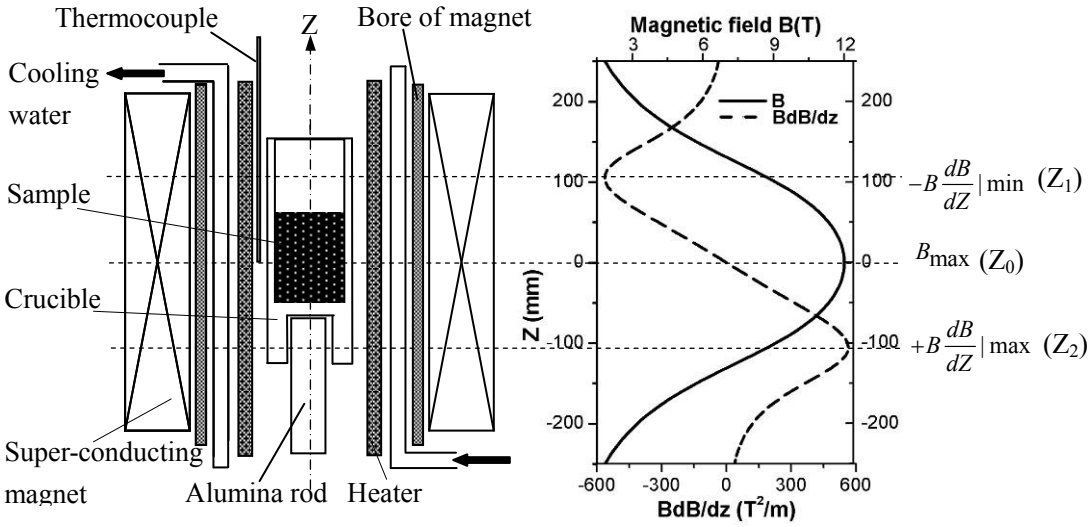

Figure 3.1 Schematic illustration of the experimental equipment and the corresponding magnetic field distribution.

In the present work, the preparation of Al-3.31wt.%Fe (or Al-1.36wt.%Zr and Al-1.95wt.%Zr) as-cast billet is the same as that mentioned in 2.2 in chapter 2. The billet was machined into several small rods. Each rod was then put into a high-purity cylindrical corundum crucible (10mm in inner diameter and 30 mm in height) for solidification experiment. Fig. 3.1 shows the schematic illustration of the experimental equipment and the corresponding magnetic field distribution. The equipment consists of a vacuum resistance furnace installed in the bore of the magnet and a superconducting magnet that can produce an axial static magnetic field (along Z direction) with a maximum magnetic flux density of 12 Tesla at the position Z_0 (i.e. B_{max}=12 Tesla) where the magnetic field is uniform within ±20 mm. When B_{max} reaches 12 Tesla, positions Z_1 and Z_2 have the maximum negative and positive *BdB/dZ*(-564 Tesla^2/m and +564 Tesla^2/m, respectively), where *B* is the magnetic flux density (both are 8.8 Tesla) and *dB/dZ* the magnetic field gradient at positions Z_1 or Z_2. An

R-type thermocouple is used to measure the furnace temperature. The corundum crucibles containing rods were placed at different positions (Z_0 or Z_2), and then magnetic fields with different densities were imposed each time. After the pressure in the furnace reached 5×10^{-3} Pa, the rods were heated up to 830 °C (or 980 °C for Al-1.36wt.%Zr and 1020 °C for Al-1.95wt.%Zr) by an electric heater at a heating rate of 5 °C/min and held at this temperature for 40 min, and then cooled to room temperature with different cooling rates. The experimental parameters for different alloys are listed in Table 3.1.

Table 3.1 Experimental parameters.

Alloys	Cooling rate (°C /min)	Position	Magnetic flux densities *B* (Tesla)					*BdB/dz* (Tesla^2/m)
Al-3.31wt.%Fe	10	Z_0	0	2	5	8	12	0
		Z_2			8.8			564
Al-1.36wt.%Zr	12	Z_0	0		2	5	12	0
Al-1.95wt.%Zr	12	Z_0			12			0

Specimens were cut longitudinally (parallel to the magnetic field direction) or transversely (perpendicular to the magnetic field direction) from the as-cast samples (about 10mm in diameter and 25 mm in length) for further examination. The macro- and microstructures of the specimens were observed with a Leica DMR optical microscope. Individual orientation measurements of the primary Al_3Fe phase were performed at manually chosen points through acquiring and indexing the EBSD Kikuchi patterns with a JOEL JSM 6500 FE-SEM, equipped with HKL Channel 5 software after an electrolytic polishing (700ml ethanol, 120ml distilled water, 100ml 2-butoxyethanol and 80 ml perchloric acid (68%), 40V, 5s).

The easy magnetization directions of the primary Al_3Fe and Al_3Zr phases are determined first by transforming the magnetic field direction (**FD**) vector in the sample coordinate system to its equivalent vector in the crystal coordinate system with the measured orientation of the crystals, and then the statistically representative crystalline direction close to the transformed **FD** vector is determined as the easy magnetization direction. The nucleation amount of the primary Al_3Fe crystals was obtained by counting the individual primary Al_3Fe crystal on the longitudinal section of the specimen.

3.3 Results of Al-Fe alloy

3.3.1 Morphology

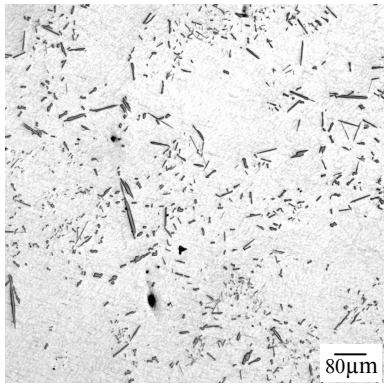

Figure 3.2 Microstructure in the longitudinal section of the initial rod cut from the as-cast billet.

Fig. 3.2 shows the microstructure in the longitudinal section of the as-cast billet as the initial material for the subsequent solidification without and with a high magnetic field. It can be seen that the initial microstructure is composed of the bar-shaped primary Al_3Fe phase (gray) and the eutectic matrix (α-Al and eutectic Al_3Fe). Due to the electromagnetic stirring and the mechanical stirring plus the subsequent rapid cooling, the primary Al_3Fe crystals are distributed relatively homogeneously within the cast billet. No macrostructural segregation of the primary Al_3Fe caused by the density difference between the two microstructural constituents is spotted.

Fig. 3.3(a)-(e) show the macrostructures in the longitudinal sections of the specimens placed in the uniform magnetic field (Z_0) with magnetic flux densities of 0, 2, 5, 8 and 12 Tesla, respectively. It can be observed that the distribution and the morphology of the primary Al_3Fe crystals are remarkably affected by the magnetic field. Without the magnetic field the primary Al_3Fe crystals mainly concentrate at the bottom of the specimen (a few of them are left in the upper peripheral region (Fig. 3.3(a)); whereas with a magnetic field the primary Al_3Fe crystals are "levitated" and tend to be distributed homogeneously in the specimen. The homogeneity enhances with the increase of the field. In addition, the primary Al_3Fe crystals tend to align with their longer axis perpendicular to the **FD**.

The "levitation" of the primary Al_3Fe crystals is also sensitive to the magnetic field gradient, as shown in Fig. 3.4. It can be seen that under a positive gradient (+64.1 Tesla/m),

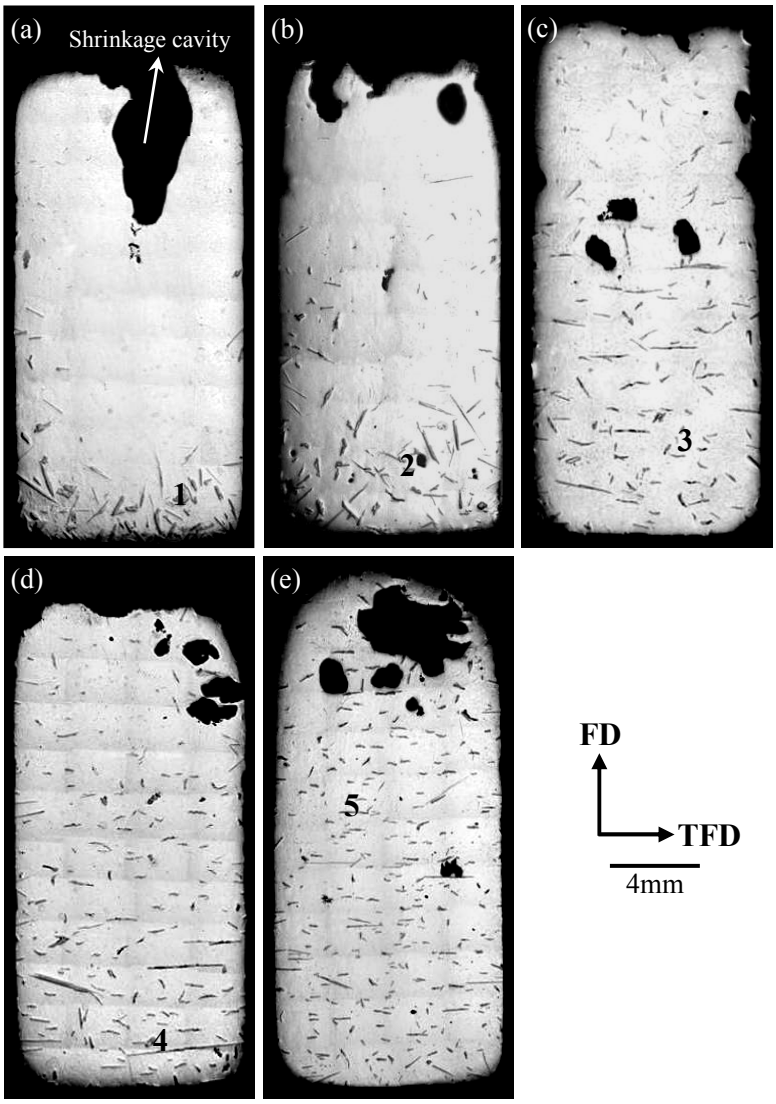

Figure 3.3 Macrostructures in the longitudinal sections of the specimens with B = (a) 0, (b) 2, (c) 5, (d) 8, (e) 12 Tesla (cooling rate: 10 °C /min; position: uniform magnetic field zone Z_0). **FD** and **TFD** denote the magnetic field direction and the transverse magnetic field direction, respectively.

most of the primary Al_3Fe crystals move upward and concentrate at the upper part of the specimen. Besides this, the alignment with their longer axis perpendicular to the **FD** remains. This phenomenon is very meaningful for practical applications. That means by modifying the magnetic field gradient distributed within the ingot, the distribution of the primary Al_3Fe crystals can be modified within the ingot for some specific requirements.

Other than the macroscopic effects of the magnetic field, it has microscopic influence on the morphology of the primary Al_3Fe crystals. Fig. 3.5(a)-(e) show the microstructures corresponding to positions 1-6 in Fig. 3.3(a)-(e), respectively. It is seen that without the magnetic field the primary Al_3Fe crystals show relatively regular shapes; whereas with the

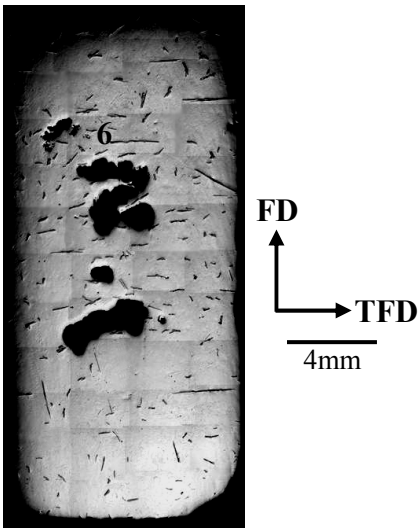

Figure 3.4 Macrostructure in the longitudinal section of the specimen with B = 12 Tesla (cooling rate: 10 °C /min; position: gradient magnetic field zone Z_2).

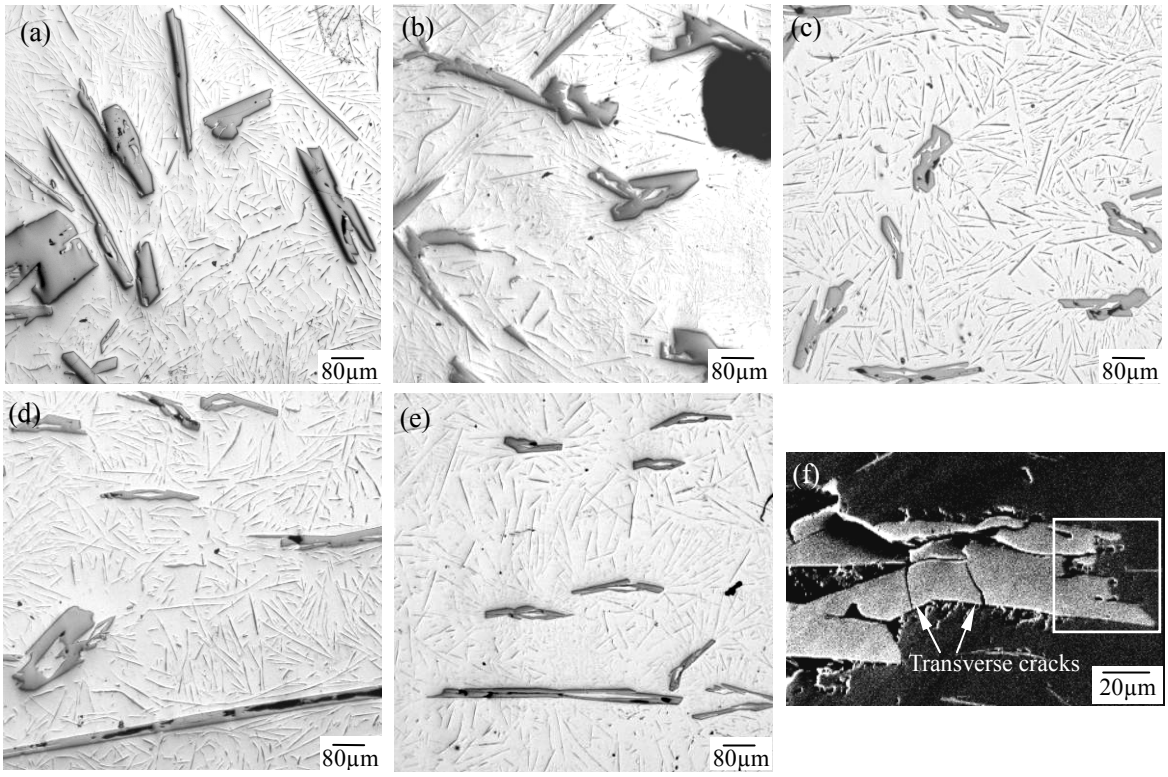

Figure 3.5 Microstructures corresponding to positions 1 (a), 2 (b), 3 (c), 4 (d) and 5 (e) in Fig. 3.3(a)-(e); (f) SEM image of a primary Al_3Fe crystal showing the transverse cracks.

magnetic field quite some of them bifurcated axially and the "gaps" between the bifurcated primary Al_3Fe crystals are filled by the eutectic mixture, as seen in Fig. 3.5(b)-(e). This suggests that bifurcations are initiated axially from the tips of the Al_3Fe crystals at the early stage of growth. Moreover, transverse cracks are also observed in the primary crystals when

magnetic field is applied, as shown in Fig. 3.5(f). The clean and sharp appearance of these cracks suggests that they form at the end of the crystal growth.

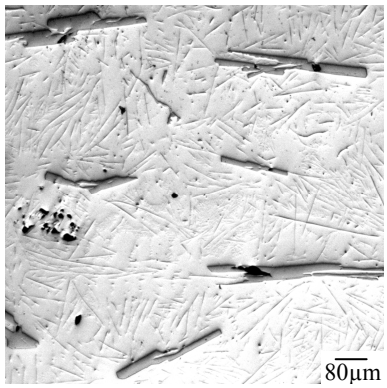

Figure 3.6 Microstructure corresponding to Position 6 in Fig. 3.4.

Fig. 3.6 shows the microstructure obtained under the gradient field (position 6 in Fig. 4). It can be found that the morphologies of the primary Al_3Fe crystals formed under the gradient field are similar to those obtained under a uniform field (Fig. 3.5(d) and (e)). A statistical observation indicates that cracks and irregular-bifurcation still exist in them.

3.3.2 Nucleation amount

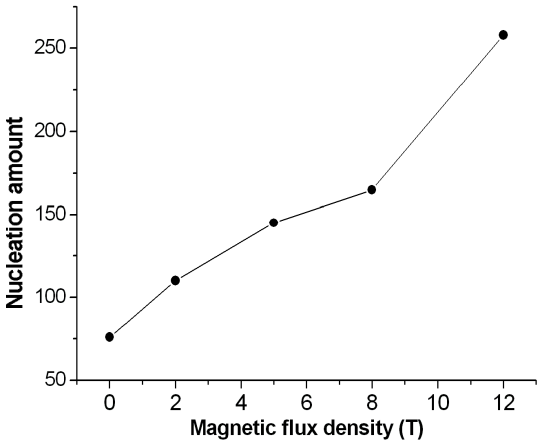

Figure 3.7 Nucleation amount of the primary Al_3Fe crystals under different magnetic flux densities.

In Fig. 3.3(a)-(e), it can also be found that the magnetic field has a remarkable effect on the amount of the primary Al_3Fe crystals. As the individual primary Al_3Fe crystals are single crystals, it is reasonable to assume that the final crystal amount corresponds to the nucleation amount of the Al_3Fe crystals. Fig. 3.7 shows the amount on the longitudinal sections of the specimens solidified under various magnetic flux densities (corresponding to Fig. 3.3(a)-(e)).

It is seen that the nucleation amount increases with the increase of the magnetic flux densities. With a 12-Tesla field the nucleus amount is more than 3 times of that in the absence of a magnetic field.

3.3.3 Crystallographic orientation

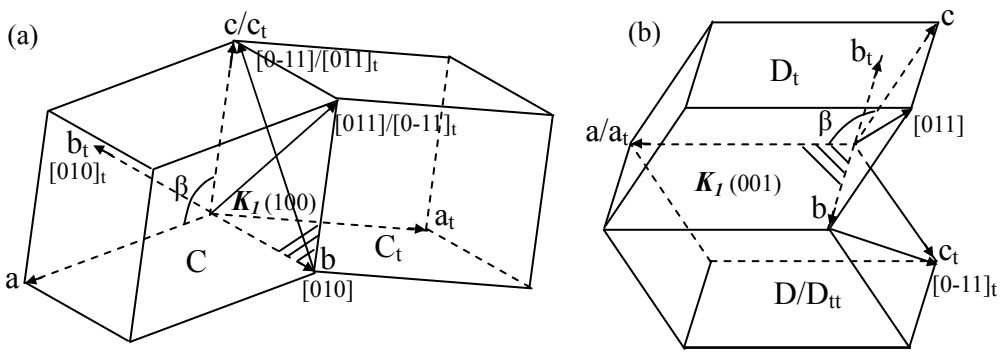

Figure 3.8 Geometric relationship between the matrix and (a) the compound twin and (b) the type I twin. K_1 is the twinning plane.

In the absence of the magnetic field the crystallographic features of the primary Al_3Fe phase have been carefully examined in section 2.3.1. The main features can be summarized as:

1) There are two preferred crystallographic extension directions: <010> and <011>. The occurrence frequency of <010> extension is a little lower than that of <011> (2:3);

2) Two sorts of twins (compound and type I) are found. In the case of <010> extension the compound twin is observed; whereas in the case of <011> extension both the compound twin and the type I twin are detected. The geometric relationship between the matrix and the twin for the two sorts of twins are illustrated in Fig. 3.8 (a) and (b), respectively;

3) The crystallographic planes exposing to the Al matrix are identified as (100) and (001) stretching in the extension direction for the monoclinic prism crystals with compound twin and (100), (001) and (02-1) for the triclinic prism crystals with type I twin.

In the presence of the 12-Tesla field an EBSD investigation has also been carried out and the result indicates that the above crystallographic features of the primary Al_3Fe phase are not modified by the magnetic field. However, the occurrence frequency of the two extension directions is heavily affected by the field - crystals extending along <010> are much more than those along <011> (4:1).

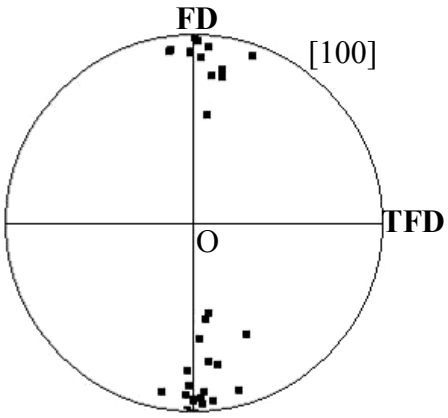

Figure 3.9 [100] direction pole figure corresponding to some distinct primary Al_3Fe crystals in the longitudinal section of the specimen with B = 12 Tesla.

Moreover, under the magnetic field, the Al_3Fe crystals show strong morphological preferential orientation, i.e. to have their principal extension direction perpendicular to the **FD**. This preferential orientation implies that there may be a specific crystallographic direction in the field direction. To verify this, a statistical calculation is made and the result indicates that the low-indexed direction [100] always appears to be close to the **FD**. To visualize this result, the [100] pole figure corresponding to the measured primary Al_3Fe crystals in the longitudinal section of the specimen with B = 12 Tesla is displayed in Fig. 3.9. It is seen that most of the crystals are aligned with their [100] in the **FD**. However, as can be seen in the pole figure, there are also quite some of the poles deviating from the **FD**. Further examination showed that the deviated poles are from the compound twinned part of the crystal. Fig. 3.10(a) shows a SEM image of a straight-extended (along <010>) and twinned (compound) primary Al_3Fe crystal composed of the matrix C and its twin C_t (a dashed line is artificially added to mark the separation between C and C_t) and Fig. 3.10(c) their correlated [100] direction pole figure. As the [100] direction (i.e., a-axis) of twin C_t is inconsistent with that of the matrix C (Fig. 3.8 (a)), pole C_t keeps away from the **FD** (26° deviation) when pole C is close to it (7° deviation). However, in the case of type I twin, both the matrix and the twin can be submitted to the **FD** as the matrix and the twin share a common [100] direction (Fig. 3.8 (b)). As an example, Fig. 3.10(b) shows a SEM image of a kink primary Al_3Fe crystal (extending along <011>) whose contour is outlined in white in the figure. The kink is the result of type I twinning. Fig. 3.10(d) displays the [100] pole figure corresponding to D and D_t. It can be seen that D and D_t parts

share a common [100] pole that is close to the **FD**.

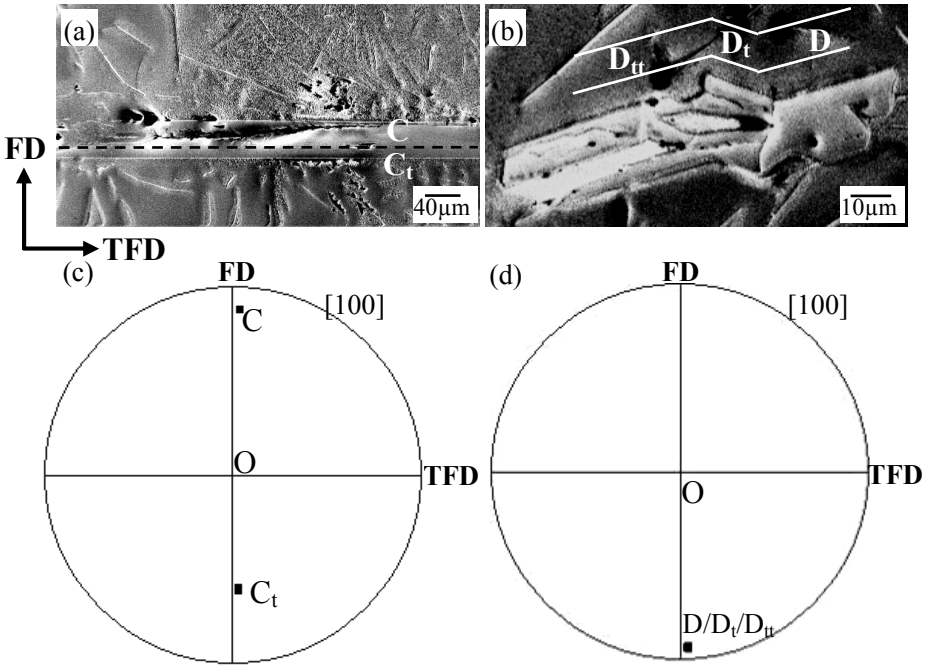

Figure 3.10 SEM images of two twinned primary Al_3Fe crystals with (a) straight and (b) kink morphology; [100] direction pole figures corresponding to (c) C and C_t in (a) and (d) D and D_t in (b).

3.4 Discussion on Al-Fe alloy

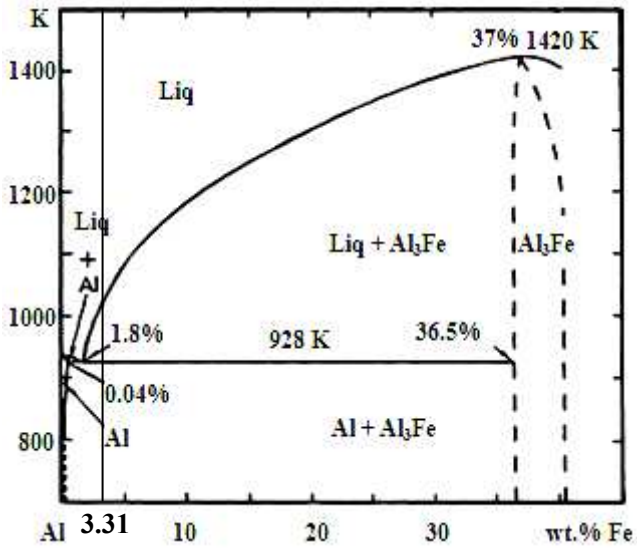

Figure 3.11 Equilibrium phase diagram of binary Al-Fe alloy at the Al rich end [24].

Fig. 3.11 shows the Al-Fe equilibrium phase diagram at the Al-rich end. It is seen that Al_3Fe phase is precipitated primarily during the solidification process of a hypereutectic alloy. This means that the precipitated Al_3Fe phase is surrounded by a liquid medium in the two-phase zone, which provides a relatively free environment for their precipitation. After

solidification, the normal microstructure is mainly composed of primary Al_3Fe phase and the eutectic mixture of alternatively distributed α phase and needle-shaped Al_3Fe.

3.4.1 Distribution

As the density of the Al_3Fe phase (ρ_1 = 3896 kg/m^3 [25]) is much higher than that of the liquid aluminum (ρ_2 = 2357 kg/m^3 at 727 °C [26]), the primary Al_3Fe crystals tend to descend when they are precipitated in liquid aluminium in the absence of a high magnetic field. However, once they begin to descend, another force – viscosity resistance force will be induced simultaneously and hinders their decent. The fact that most of the primary Al_3Fe phase located at the bottom of the specimen indicates that the viscosity resistance force is not sufficient enough to prevent them from descending (Fig. 3.3(a)). As for the primary Al_3Fe crystals appearing in the peripheral region of the specimen, it should be related to the high cooling rate of the melt close to the crucible. It is known that liquid metal solidifies from the outside toward the center during such non-directional solidification process. Thus, the dynamic viscosity of the liquid aluminum close to the crucible wall increases more quickly than that in the center. This suggests a much stronger viscosity resistance force than that in the center. Moreover, the crucible wall may also contribute to the prevention of their descent. Thus, some primary crystals precipitated in the peripheral region cannot fully descend to the bottom.

When the precipitated Al_3Fe crystals descend in the presence of a uniform high magnetic field, magnetic viscosity resistance force related to the Lorentz force will be induced and prevent their descent. This force is proportional to the square of the magnetic flux density [20] and has been verified to be quite effective in homogenizing the distribution of the primary Al_3Ni phase in Al-Ni alloy [14]. In the present work, the fact that the primary Al_3Fe crystals are distributed more and more uniformly throughout the whole specimen (see Fig. 3.3(b)-(e)) also result from this induced Lorentz force. In addition, it should be mentioned that the reorientation of the primary crystals by the magnetic field (with their long axis perpendicular to the **FD**) increases the viscosity resistance force and thus slows down the descent of the Al_3Fe crystals.

When the Al_3Fe crystals are precipitated in a gradient high magnetic field, an extra

effective magnetization force ΔF_m will be induced. When only the gradient in Z direction is considered, ΔF_m can be given as

$$\Delta F_m = V \frac{\chi_S - \chi_L}{\mu_0} B \frac{dB}{dZ} \tag{3.1}$$

where χ_S and χ_L are the respective susceptibilities of the Al_3Fe crystal and the liquid aluminum, $\mu_0 = 4\pi\times10^{-7}$ H/m is the permeability of vacuum. It has been identified that both Al_3Fe and aluminium are paramagnetic [25], suggesting that χ_S and χ_L are positive. Assuming that $\chi_S > \chi_L$, ΔF_m would be along the Z direction, i.e., upward directed. If it is strong enough, it can overcome the effective gravitational force $\Delta G = V(\rho_1 - \rho_2)g$ (V is the volume of the crystal and g the gravitational acceleration) and drive the crystals to move upward. The upward movement also induces viscosity resistance force and magnetic viscosity resistance force in the opposite direction to inhibit this movement. The balance of all these forces decides the final movement of the crystals. For the sample placed in the positive gradient magnetic field (Z_2) in the present work, the fact that most of the primary Al_3Fe phase concentrate in the upper part of the specimen evidences that the upward magnetization force is dominant and the resistance forces are limited in preventing the upward movement. Meanwhile, this fact also verifies that the magnetic susceptibility of Al_3Fe is bigger than that of the liquid aluminium, i.e., the assumption of $\chi_S > \chi_L$ is correct. Based on this inequation, the mean magnetic susceptibility of the Al_3Fe crystal χ_S can be estimated. The result indicates $\chi_S > 3.76\times4\pi\times10^{-6}$ when χ_L is taken as $1.09\times4\pi\times10^{-6}$ [27]. From the distribution of the primary Al_3Fe crystals in Fig. 3.4, it can be found that the upward movement of the Al_3Fe crystals is limited, suggesting that the true χ_S should be close to the value estimated above.

3.4.2 Alignment

In the present work, all the samples were solidified in a non-directional way. The liquid metal solidifies inward from the crucible wall. Normally, the heat should flow out of the sample along the direction perpendicular to the crucible wall, as illustrated in Fig. 3.12. It is

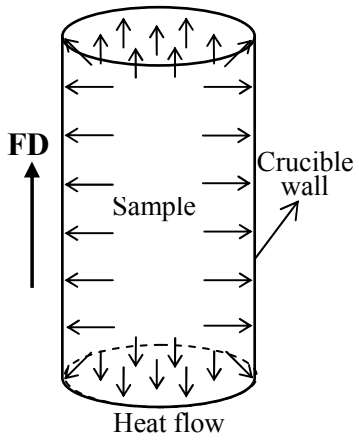

Figure 3.12 Schematic view of the heat flow direction during the solidification of the sample.

known that a crystal usually grows in the direction opposite to that of the heat flow. Purely under such a condition, the primary Al_3Fe crystals in the present work should always align with their longer axis perpendicular to the crucible wall, i.e., they are vertical at the top and at the bottom of the specimen and horizontal in the middle of the specimen. However, during the solidification in the absence of the magnetic field, convections can be easily induced due to the descent of the primary Al_3Fe crystals, which disturbs the temperature field in the melt and thus results in instability of the heat flow. Moreover, the convections may also change the initial orientations of the precipitated nuclei during their descent. All of these contribute to the final random distribution of the primary Al_3Fe crystals in the matrix (Fig. 3.3(a)).

When a magnetic field is applied, the Al_3Fe crystals tend to align with their [100] direction parallel to the **FD**, indicating that the crystals possess crystallographic magnetic anisotropy. It is known that Fe has 3d unpaired electrons that give rise to the magnetism, whereas Al atom has no unpaired electrons and hence it is magnetically neutral. Therefore, it is reasonable to consider that the crystallographically anisotropically distributed Fe atoms in the Al_3Fe crystal gives rise to the crystallographic magnetic anisotropy of the crystal. Detailed examination of the Fe atomic positions in the Al_3Fe unit cell shows that [100] direction is the Fe close-packed direction, indicating an enhanced magnetism in this direction. It is known that the magnetization energy U_i is dependent on the magnitude of the crystallographic magnetic susceptibility in the field direction [5]:

$$U_i = -\frac{\chi_i}{2\mu_0\left(1+N\chi_i\right)^2}B^2 \tag{3.2}$$

where the subscript i denotes crystallographic direction i, N is the demagnetization factor. As can be seen in Eq. (3.2), when the highest magnetic susceptibility direction of the crystal is in the field direction, the magnetization energy reaches the minimum; hence the crystal reaches its stable position. In the present work, the alignment of the Al_3Fe crystal with their [100] direction parallel to the **FD** obviously shows an energetic preference due to the enhanced magnetism in [100]. The driving force for the crystal alignment arises from the magnetic torque, which is proportional to the square of the imposed magnetic flux density [28]. Thus, the alignment tendency of the primary crystals enhances with the increase of the magnetic flux densities (Fig. 3.3(a)-(e)). However, it should be noted that once the crystal starts to be rotated by the magnetic torque, two other preventing torques induced by Lorentz force and viscosity resistance will also be generated simultaneously. If the magnetic flux density is not strong enough, the rotation will be suppressed. The alignment of most of the primary crystals in Fig. 3.16(e) indicates that these preventing torques are overcome by the magnetic torque when a 12-Tesla field is applied.

Once the crystals in the central region of the specimen are oriented with their [100] direction parallel to the field, their preferred extension direction <010> turns to the favorable heat evacuation direction that is perpendicular to the **FD** in the middle of the ingot (Fig. 3.12). This further ensures the alignment of the Al_3Fe phase. For the crystals extending along <011>, the easy magnetization direction is not perpendicular to the extension direction. Therefore, for such crystals, the extension in the favorable heat evacuation direction and the magnetic alignment cannot be simultaneously satisfied. From our crystallographic orientation analysis, it seems that alignment by the magnetic field is dominant.

In section 3.3, it was mentioned that the occurrence frequency of the primary Al_3Fe crystals principally extending along <010> is higher than that of the crystals extending along <011> when a 12-Tesla field is applied. This should also be attributed to the combined effects of the magnetic field and the heat evacuation. As the primary Al_3Fe crystals extending along <010> are simultaneously favored by these two effects, it is natural that their occurrence frequency turns to be higher.

3.4.3 Bifurcation and cracks

Other than the above-mentioned magnetic viscosity resistance force and magnetization force, thermoelectric magnetic force (TEMF) can also be induced by the magnetic field during the growth of the primary crystals. The axial bifurcation of the primary crystals (Fig. 5(b)-(e)) when magnetic field is applied may just result from this TEMF. During the solidification process of metallic alloys, a temperature gradient at the solid-liquid interface can produce a Seebeck electromotive force and then results in a local thermoelectric (TE) current [29]. When an external magnetic field is applied, this TE current will result in the so-called TEMF both in the solid and liquid [30]. In the present work, the primary Al_3Fe crystals should also be subjected to this TEMF. As shown in Fig. 3.5(f), the surfaces stretching parallel to the extension direction of the primary Al_3Fe crystal are relatively smooth (they are crystallographically low-indexed according to the previous crystallographic analysis), whereas that at the tip is rough (enclosed by the white frame in Fig. 3.5(f)). During the crystal growth the solid/liquid interfaces at the tips of these crystals should also be rough with protrusions, therefore the temperature gradient may not be homogenous. Thus, the TEMF is not constant with changes in direction and in magnitude. Under the inhomogeneously distributed TEMF, migration of the solid/liquid interfaces during the growth process is disturbed. Some protrusions could be twisted or distorted and thus deviate from the original extension direction, becoming new branches. Meanwhile, the “gaps” between them are filled by the Al melt. If the TEMF is strong enough, detachment of some of the protrusions may even happen and the fragmented crystals can act as seeds for the nucleation of the new primary Al_3Fe crystals if the thermal and compositional conditions are appropriate. Some similar disturbing effects on the solidification interfaces of Al-Cu alloy induced by the TEMF have also been found during the solidification process [30].

It is known that Al_3Fe phase is brittle [31], suggesting that it has a high cracking tendency. When the temperature of the melt drops near the solidus line, another force – internal stress will probably be induced in the primary Al_3Fe due to the large difference in the linear shrinkage coefficient between the aluminium solid solution and the primary Al_3Fe phase [32], and then may result in the formation of transverse cracks (Fig. 3.5(f)). In the case of 0-T field, the primary Al_3Fe crystals are mainly located at the bottom of the specimen and wrapped by a

small volume of aluminium solid solution. Thus, the internal stress induced by the shrinkage difference between the primary crystals and aluminium solid solution is relatively small. Moreover, as can be seen in Fig. 3.5, the primary crystals in the absence of magnetic field are thicker than those in the presence of the magnetic field; therefore they are more cracking resistant. Taking the two factors into account, it can be understood that less cracks form in the primary Al_3Fe phase in the absence of the magnetic field.

3.4.4 Nucleation

The magnetic field applied clearly increases the amount of the Al_3Fe crystals as displayed in Fig. 3.7, indirectly showing that the magnetic field increases the nucleation rate.

It is known that during solidification if the magnetisms of the liquid phase and the solid phase are different, the application of a high magnetic field will introduce an additional Gibbs free energy difference and the total Gibbs free energy difference for the precipitation of the solid phase ΔG_f can be expressed as follows [33]:

$$\Delta G_f = -V_S \Delta G_V + \sum_i A_{SL}^i \gamma_{SL}^i - V_S \Delta G_M \tag{3.3}$$

where V_S is the volume of the solid, ΔG_V the volumetric Gibbs free energy difference between the solid and the liquid, A_{SL}^i the solid/liquid interfacial area, γ_{SL}^i the interfacial energy density, and ΔG_M volumetric magnetization energy difference between the solid and the liquid (the subscripts S and L denote the solid and the liquid, respectively). Theoretically, it can help reduce the critical energy barrier for the nucleation when $\Delta G_M > 0$ and thus favors the increase of the nucleation rate. However, the induced magnetization energy difference is usually very small and can be ignored compared with the volumetric Gibbs free energy difference ΔG_V. To verify this, some calculations were carried out as follows.

When the undercooling ΔT is small, ΔG_V can be taken as

$$\Delta G_V \approx L_V \Delta T / T_m \tag{3.4}$$

where L_V is the latent heat of fusion per unit volume and T_m the melting temperature of the solid. Moreover, ΔG_M can be expressed as

$$\Delta G_M = \frac{1}{2}\frac{\chi_S - \chi_L}{\mu_0} B^2 \tag{3.5}$$

As there is no experimental data or calculated data of latent heat of fusion for Al_3Fe available, the L_V =9.857×10^8 J/m^3 [34] of pure aluminium is taken as the calculating parameter. Based on the estimated result in section 4.1, a conservative value of χ_S = 5×4π×10^{-6} is taken as another parameter. The melting temperature T_m of Al_3Fe is 1442.5 K [35]. Assuming ΔT = 5 K, we obtain ΔG_V = 3.42×10^6 J/m^3 and ΔG_M = 2.82×10^3 J/m^3. From this result, it can be found that ΔG_M is much smaller than ΔG_V, suggesting that the energetically effect of the magnetic field on the nucleation of the primary Al_3Fe crystals is very limited. Therefore, there should be some other reasons inducing the substantial increase of the nucleation amount in the present work.

One of the reasons may be the detachment caused by TEMF as mentioned in section 3.4.3. The other may be attributed to the suppression of Fe solute diffusion induced by magnetic field. It has been previously mentioned in the experimental section that the magnetic field was applied before the heating process of the solidification. As the magnetic field strongly damps the melt convection and suppresses the diffusion of the charged solutes in the direction perpendicular to the field direction [36-38], the redistribution (or homogenization) of the solute atoms during the reheating process is greatly inhibited compared with the heating process in the absence of a magnetic field. The solute Fe atoms are more concentrated at the sites of previous Al_3Fe (primary and eutectic) crystals. Since the initial material is prepared under forced electromagnetic and mechanical stirring and solidified under rapid cooling, there was no obvious segregation of primary Al_3Fe crystals as shown in Fig. 3.2. After the reheating under the high magnetic field, more high concentration sites of Fe atoms may be left and act as potential nuclei for the primary Al_3Fe crystals during the subsequent solidification. In this way, the nucleation amount is enhanced. This result also possesses practical interest for nucleation control during solidification. By introducing a magnetic field during the reheating of a specially prepared alloy, the nucleation of the primary phase can be controlled.

3.4.5 Growth

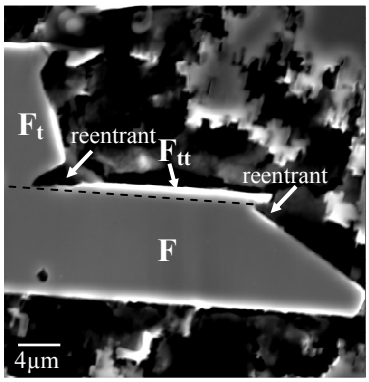

Figure 3.13 Magnified SEM image of the structure in the while frame in Fig. 3.5(e).

It has been presented in Mn-Sb near-eutectic alloy that the solidified eutectic MnSb crystals can be magnetized in the magnetic field direction and then attract Mn atoms to their solidification front during the solidification [39]. As a consequence, the MnSb phase is elongated in the **FD**. In the present work, the primary Al_3Fe crystals are also rotated to have their easy magnetization direction to the field direction. Logically the Fe atoms could also be attracted to the liquid/solid interface in the **FD** and result in an elongation in the **FD**. However, it is not the case for the present alloy. The true elongation always happens in the perpendicular direction, suggesting a different growth mechanism. According to current crystal growth theories, the growth of a crystal is realized by the migration of its surfaces. The migration rate of each surface is related to the atomic level roughness. The atomic arrangement of low Miller indexed surfaces is usually smooth and atoms are difficult to attach to them. Thus, the migration velocity of these surfaces is low. In the present case, it has been identified that (100) and (001) are the crystallographic planes binding the primary Al_3Fe crystals. If the primary Al_3Fe crystals should elongate along the easy magnetization direction [100], it requires the (100) planes (that is in the most perpendicular position to [100]) to migrate faster. As this plane is atomically smooth and difficult to assimilate atoms, its fast migration requires an extra energy to compensate the interfacial energy increase by allowing atoms to attach to it. Obviously in our case, the magnetization energy is not sufficient enough to compensate this interfacial energy increase. Therefore, elongation of the primary Al_3Fe crystals in the field direction is not realistic. Moreover, twinning plays an important role to promote the growth of

the crystal in the field perpendicular direction or the identified principle extension direction. For the two sorts of twins, the twinning plane is either (100) (compound twin) or (001) (type I). The twinned parts are also enclosed by the same surfaces stretching in the identified extension direction as their matrix, but at the tip of the crystals the compound twin always introduce re-entrant grooves, as shown in Fig. 3.13. In the figure, one tip of a primary Al_3Fe crystal is displayed. Crystal F and F_t (F_{tt} has the same crystallographic orientation as F_t) are twin related (compound twin) and they all extend along <011>. Two re-entrant grooves between the twinned crystals are clearly seen. Surely these grooves are efficient in accepting atoms and enhance crystal growth in the <011> direction. In this way, growth in the field direction is not favorable.

3.5 Results of Al-Zr alloy

3.5.1 Morphology

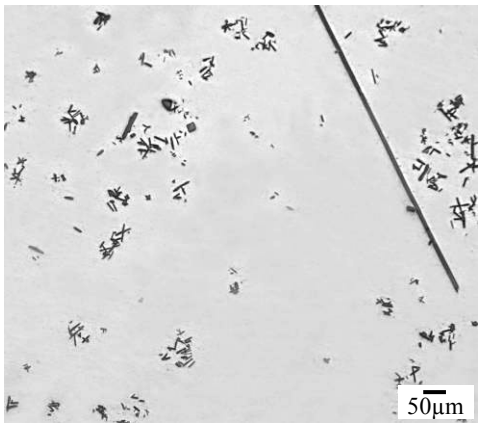

Figure 3.14 Microstructure in the longitudinal section of the initial rod cut from the as-cast billet.

Fig. 3.14 shows the microstructure in the longitudinal section of the Al-1.36 wt.%Zr as-cast billet as the initial material for the subsequent solidification without and with a high magnetic field. It can be seen that the initial microstructure is composed of the fine primary Al_3Zr phase (dark grey color) and the α-Al matrix (light grey color), which are confirmed by EBSD measurement. Due to the electromagnetic stirring and the mechanical stirring, the primary Al_3Zr crystals are distributed relatively homogeneously within the cast billet. No macrostructural segregation of the primary Al_3Zr caused by the density difference between the two microstructural constituents is spotted.

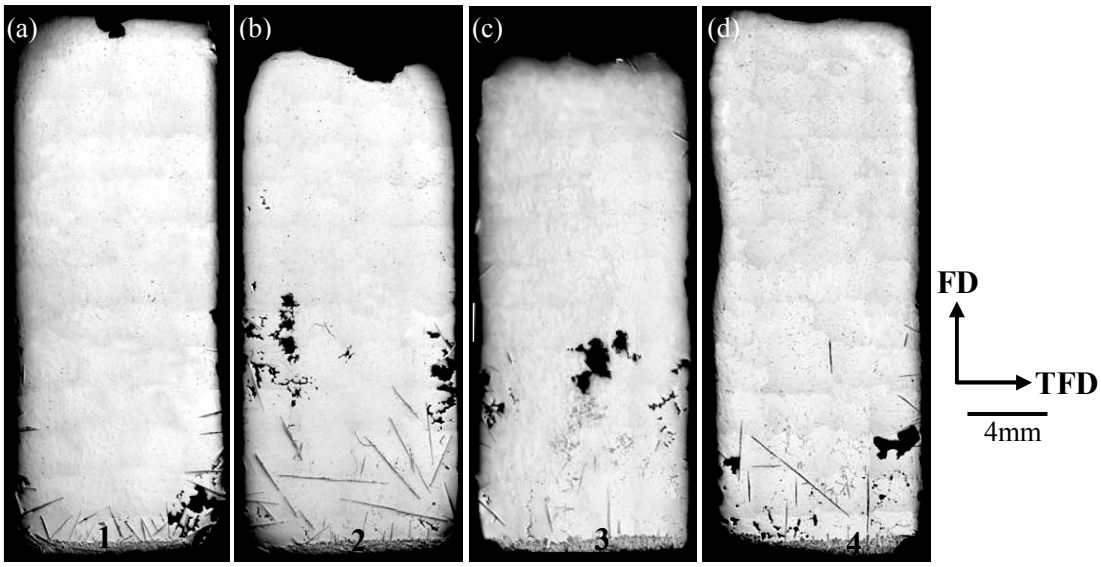

Figure 3.15 Macrostructures in the longitudinal sections of the specimens with magnetic flux densities *B* of (a) 0, (b) 2, (c) 5 and (d) 12 Tesla. **FD** and **TFD** denote the field direction and the transverse field direction, respectively.

Fig. 3.15(a)-(d) show the macrostructures in the longitudinal sections of the Al-1.36 wt.%Zr specimens with magnetic flux densities of 0, 2, 5 and 12 Tesla, respectively. It can be observed that the primary Al_3Zr phase (dark grey color) reveals two different sorts of morphologies in all the specimens – the short dimensioned ones in the thin sedimentary deposit layer (postions 1, 2, 3 and 4) and long bars. Fig. 3.16(a)-(d) displays the microstructures of the sedimentary deposit layer corresponding to positions 1, 2, 3 and 4, respectively. Clearly, the layers are composed of bar- and plate-shaped primary Al_3Zr crystals and α-Al matrix. Here, it should be mentioned that these bar- and plate-shaped primary Al_3Zr crystals actually have tabular morphology, which has been thoroughly studied previously. Besides the long bars and the tabular crystals in the deposit layer, a further microscopic observation at position 5 in Fig. 3.15(c) indicates that the primary Al_3Zr crystals can also be in dendritic form, as shown in Fig. 3.17.

From the macro- and microstructures of the specimens, it can also be found that the alignment of the primary Al_3Zr phase is remarkably affected by the magnetic fields. Both the long bars (Fig. 3.15) and those in the sedimentary deposit layers (Fig. 3.16) tend to align with

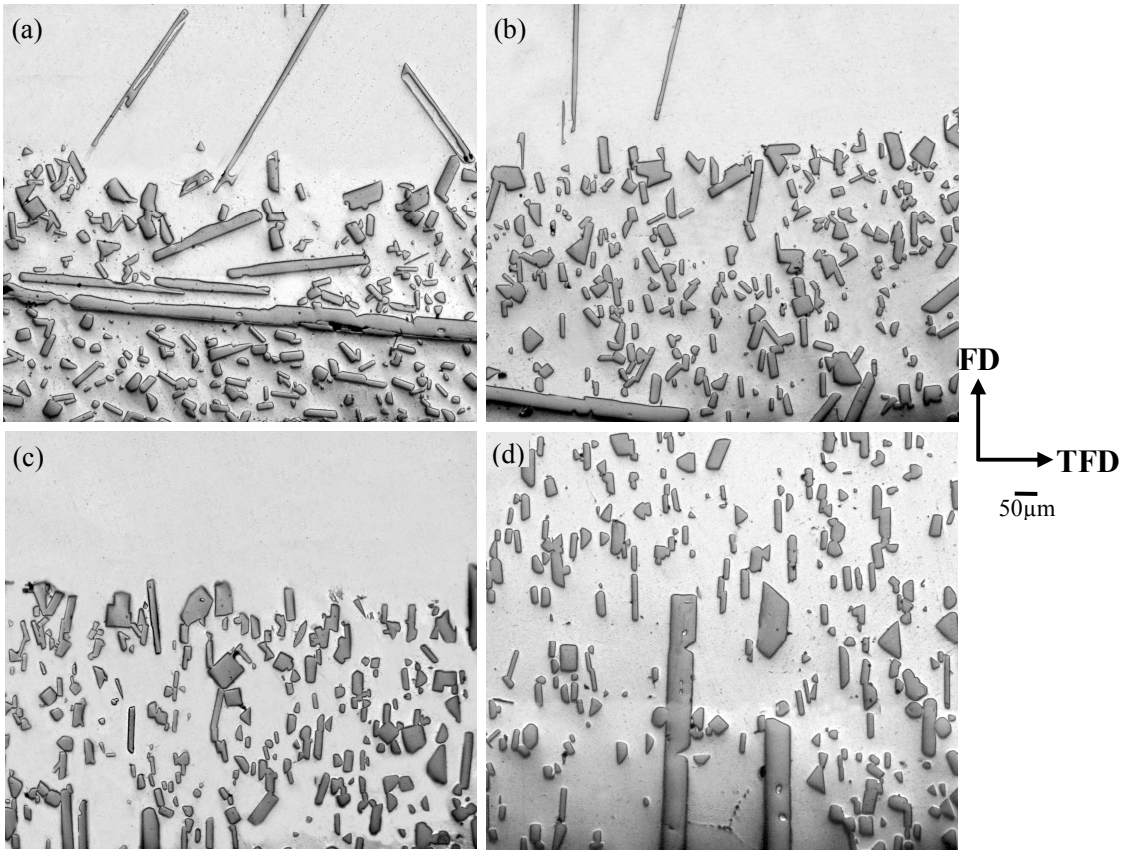

Figure 3.16 Microstructures corresponding to the positions 1 (a), 2 (b), 3 (c) and 4 (d) in Fig. 3.15.

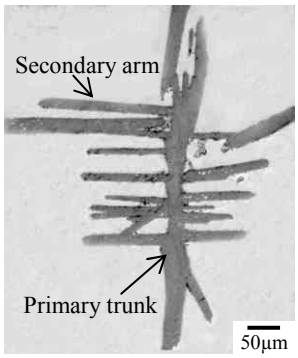

Figure 3.17 The dendritic primary Al_3Zr crystal observed at position 5 in Fig. 3.15(c).

their longer axis to the field direction (**FD**), and this tendency is enhanced with the increase of the magnetic flux densities. However, a statistical observation around position 5 in Fig. 3.15 indicates that the 5-Tesla magnetic field does not have remarkable influence on the alignment of the dendritic crystals – they are randomly oriented in the matrix. In addition, it should also be noted that the distribution of the primary crystals is not sensitive to the magnetic fields – they are mainly distributed at the lower parts of the specimens.

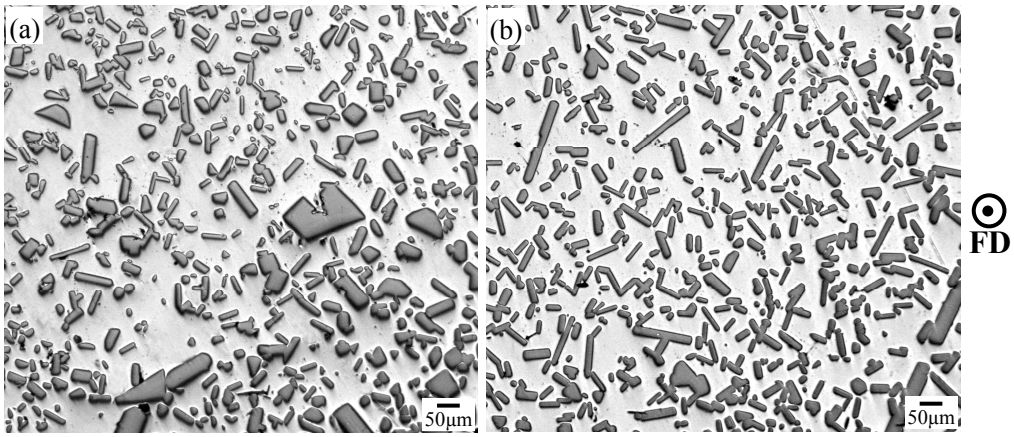

Figure 3.18 Microstructures in the transverse sections of the specimens with magnetic flux densities *B* of (a) 0 and (b) 12 Tesla.

In order to examine the three-dimensional distribution of the primary Al_3Zr crystals in the sedimentary deposit layers, Fig. 3.18(a) and (b) show the microstructures in the transverse sections of the specimens without and with a 12-Tesla field, respectively. Different from the longitudinal sections, there is no specific alignment in the directions perpendicular to the field direction **FD**, confirming that the primary Al_3Zr plates only align in the field direction.

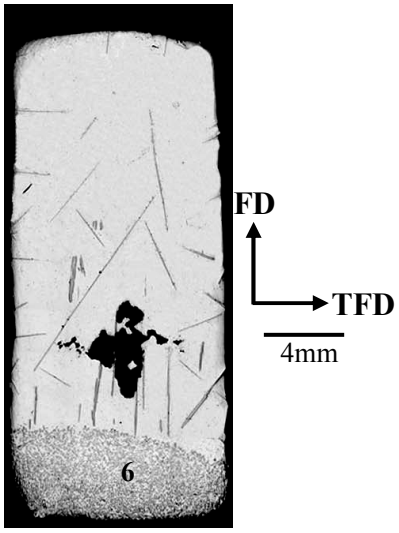

Figure 3.19 Macrostructure in the longitudinal section of the Al-1.95 wt.%Zr specimen with magnetic flux density *B* of 12 Tesla.

Fig. 3.19 shows the macrostructure in the longitudinal section of the Al-1.95wt.%Zr specimen solidified under the magnetic field of 12 Tesla and Fig. 3.20 the microstructure of its sedimentary deposit layer, corresponding to position 6 in Fig. 3.19. It is seen that with the increased Zr content in the alloy, there is no morphology change for the primary Al_3Zr.

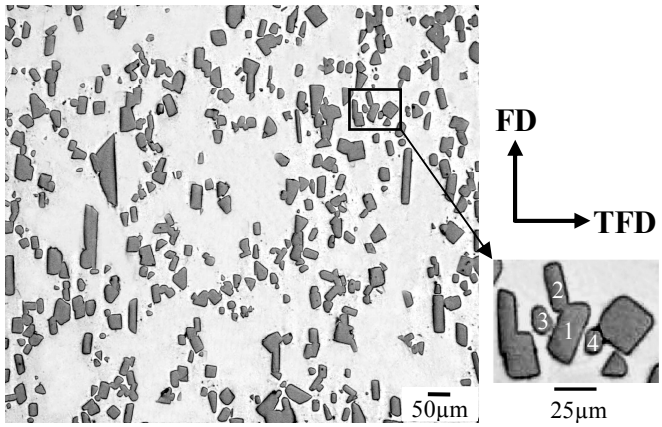

Figure 3.20 Microstructure corresponding to position 6 in Fig. 3.19. The zoom image displays the crystals enclosed in the black frame and will be analyzed in the discussion part.

However, the precipitation amount of the primary Al_3Zr is obviously increased. The sedimentary deposit layer and the long bar region are much thicker than that of Al-1.36wt.%Zr specimen (Fig. 3.15(d)). In the two regions the primary Al_3Zr crystals still tend to align with their longer axis to the field direction. For the long bars, the ones located at the lower part exhibit strong alignment tendency, whereas this tendency decreases when the bars are "levitated" to the upper part of the specimen. For the primary Al_3Zr crystals in the sedimentary deposit layer, the alignment tendency under the 12 Tesla magnetic field becomes weak compared with those in the Al-1.36wt.%Zr alloy (Fig. 3.16). As can be seen in Fig. 3.20, many primary Al_3Zr crystals gather together and form clusters as shown in the zoomed image.

3.5.2 Crystallographic orientation

It has been determined in 2.3.2 that in the absence of the magnetic field the primary Al_3Zr crystals in the deposit layer are bound by {001}, {101} and {111} faceted planes at the initial state of formation. As the three planes have different atomic roughness and hence different migrating rate, the rough {111} and stepped {101} planes migrate faster than the smooth {001} plane. The crystal expends laterally by the migration of the {111} and {101} planes. Between the {111} and the {101} planes, {111} migrate faster and tend to disappear during the growth process. Finally the tabular plates with octagonal longitudinal form enclosed with the three kinds of planes and the rectangular form enclosed with only {001} and {101} are obtained. A further detailed crystallographic study in this work indicates that the long bars and the dendritic crystals are bound by the same faceted planes. For the long bars, they are

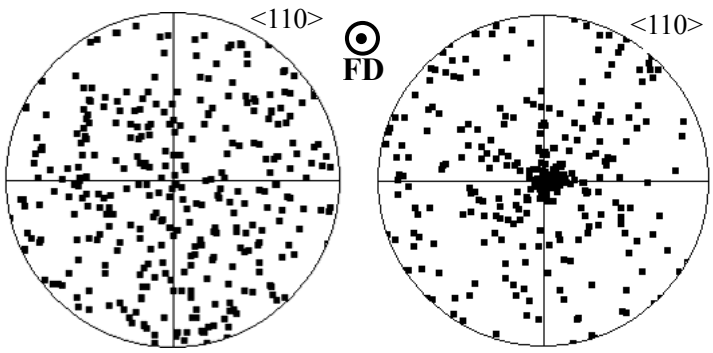

Figure 3.21 <110> stereographic projections on the observation plane corresponding to some distinct primary Al_3Zr crystals.

preferentially extended along one <100> direction. As found in the previous work, the primary Al_3Zr crystals tend to twin. The reorientation of the crystal by twinning changes its growth direction. As a result, dendrites develop from the matrix. It seems that the magnetic field applied has little effect on the above crystallographic features (surface plane and twinning). However, it exhibits remarkable influence on the crystallographic orientations of the tabular crystals in the deposit layer. The crystallographic calculation indicates that the low-index direction <110> of the tabular primary crystals in the deposit layer always appears in the **FD**. Fig. 3.21(a) and (b) show the <110> stereographic projections on the observation plane of individually selected tabular primary crystals in the transverse sections of the Al-1.36wt.%Zr specimens solidified without and with the 12-Tesla magnetic field. It is seen that without the magnetic field the <110> directions are distributed randomly in the sample coordinate system, whereas with the 12-Tesla magnetic field they are mainly concentrated in the **FD**, suggesting that the primary Al_3Zr crystals reorient to have their <110> directions parallel to the **FD**. From this phenomenon, it is reasonable to consider that <110> direction is the field preferred direction.

For most of the long bars in both Al-1.36wt.%Zr (Fig. 3.15(d)) and Al-1.95wt.%Zr (Fig. 3.19) specimens obtained under the 12-Tesla magnetic field, the calculation result indicates that no specific crystallographic direction appears in the **FD**. However, an investigation on those with longer axis parallel to the **FD** indicates that their crystallographic directions vary between <100> and <110> in the **FD**. For the dendritic crystals in the specimen with a 5-Tesla field (Fig. 3.15(c)), there is no specific crystallographic direction in the **FD**, either.

3.6 Discussion on Al-Zr alloy

3.6.1 Distribution

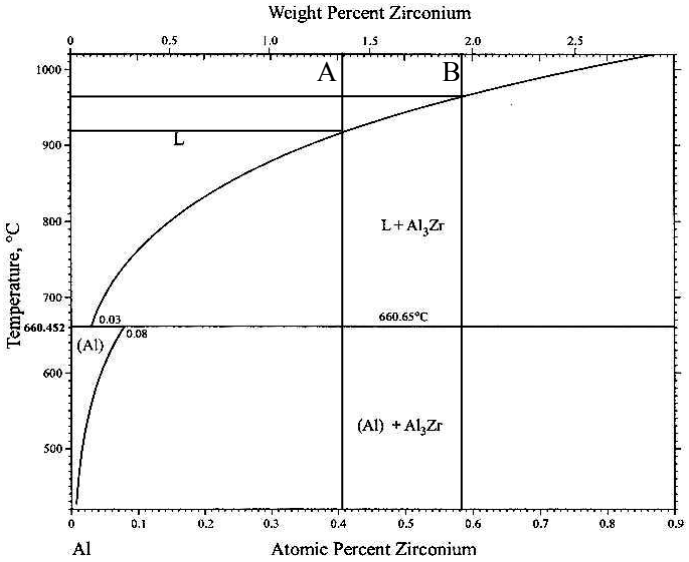

Figure 3.22 Phase diagram of binary Al-Zr alloy at the Al rich end [40].

Fig. 3.22 shows the Al-Zr equilibrium phase diagram at the Al-rich end. It is seen that during the solidification of Al-1.36wt.%Zr (vertical line A) and Al-1.95wt.%Zr (vertical line B), Al_3Zr phase is precipitated primarily when the temperature drops below the liquidus line (920 °C for Al-1.36 wt.%Zr alloy and 965 °C for Al-1.95 wt.%Zr alloy), and then with a further temperature drop to the solidus line (660.65 °C) some of the Al_3Zr will react with the liquid to form α-Al solid solution. Therefore, the solidified microstructure of the alloy is composed of primary Al_3Zr and α-Al matrix. As seen in Fig. 3.14, the as-cast initial Al-1.36wt.%Zr rods used for the non-field and field solidification experiments just consist of such microstructure, primary Al_3Zr phase plus the matrix. When such rods are reheated to the temperature above the solidus line, the α-Al matrix begins to melt but some of the original primary Al_3Zr crystals still remain solid, as the heating rate is relatively low and allows the alloy to stay in the liquid-solid region for some time. It is known that the density of Al_3Zr crystal (4100kg/m^3 [25]) is much higher than that of the liquid aluminium (2330 kg/m^3 at 800 °C [26]), so the un-melted primary Al_3Zr crystals will descend. As the duration in the two-phase region in the heating process for Al-1.36wt.%Zr reaches 52 min (temperature interval: 920 °C – 660 °C; heating rate: 5 °C/min), the un-melt primary Al_3Zr crystals have

enough time to descend to the bottom of the crucible. As a consequence, the averaged Zr content at the bottom is remarkably increased and exceeds the initial average Zr content (1.36wt.%). According to the Al-Zr phase diagram, the increased Zr content corresponds to an elevated liquidus line, i.e. elevated melting temperature. Thus, some of the deposited primary Al_3Zr crystals may still remain solid even the sample is heated to the temperature (980 °C) above the liquidus line of the Al-1.36wt.%Zr alloy. When cooling starts, the un-melted primary Al_3Zr crystals at the bottom of the crucible start to grow, and at the same time, new primary Al_3Zr crystals start to nucleate in the Al_3Zr deplete melt, i.e. the upper part of the ingot. The two kinds of Al_3Zr crystals grow under different environments.

The growth of the primary crystals at the bottom of the crucibles is restricted by the solute diffusion, i.e. they mainly absorb the solutes around them. Therefore, it is not easy for them to grow into large sizes. Compared with these crystals, the growth of the newly precipitated primary Al_3Zr crystals is facilitated by two favorable conditions. One is that the nucleation rate is relatively low due to the low cooling rate and thus the low undercooling of the melt and the other is that they can more easily absorb Zr solutes from the melt. Therefore, they can grow into large sizes.

As mentioned previously, the growth of the crystals is realized by the lateral migration of the {101} planes ({111} tend to disappear). Crystallographically the planes from the same family are identical and should have the same migration rate. However , in reality their migration strongly depends on the heat flow and composition conditions, which may not be locally uniform due to some disturbance, such as convection induced by their descent. When only the lateral planes on one side or two opposite sides of the newly precipitated primary Al_3Zr crystals are favored by these two conditions, long bars that preferentially extend along one <100> direction will be formed. Thus, the previously descent crystals during the heating form the thin sedimentary deposit layer, whereas the later precipitated crystals during the cooling grow into the long bars. For the dendritic crystals, it has been analyzed previously that they are related to the formation of compound twins which may result from some external disturbance (e.g. convections in the melt).

It has been proved during the solidification of previous Al-Fe alloy that the application of

a high magnetic field can “levitate” the primary crystals and homogenize their distribution in the samples due to the induced magnetic viscosity resistance force. However, during the solidification of Al-Zr alloy the density of Al_3Zr crystal is much higher than the Al melt so that the magnetic field is not sufficient to suppress their descent. As a consequence, the primary Al_3Zr crystals are mainly distributed at the lower parts of the specimens even under a high magnetic field.

For the Al-1.95wt.%Zr rod, it is solidified under the same treatment condition as that of the Al-1.36wt.%Zr, therefore there is no morphology change for the primary Al_3Zr crystals. However, as the zirconium content is increased, it is natural that the precipitation amount of the primary crystals is increased. Meanwhile, the long bars can also absorb more solute atoms and then grow longer. As a consequence, the sedimentary deposit layer and the long bar region become much thicker than that of Al-1.36wt.%Zr. As the length of the long bars is increased, the viscosity resistance force acting on them during their descent will be enhanced when their longer axis are not parallel to the gravity force. Therefore, more long bars remain in the upper part of the ingot when the solidification is complete, as seen in Fig. 3.19. However, the long bars with the longer axis close to the gravity force are less affected by the viscosity resistance force, so they descend more rapidly to the lower part.

From the above analysis, it appears that to effectively eliminate the gravity segregation and multiform of the primary Al_3Fe crystals, magnetic field is not sufficient. Other means like rapid heating and cooling plus forced stirring could be an alternative solution.

3.6.2 Alignment

During the heating process of the alloy without the magnetic field, convections will be induced due to the descent of the primary Al_3Zr crystals. They can disturb the temperature field in the melt and change the orientations of the original primary Al_3Zr crystals during their descent. All of these contribute to the final random distribution of the primary Al_3Zr crystals in the deposit layer (Fig. 3.15(a)). For the long bars formed during the cooling process, their random distribution is also related to the induced convections.

When a high magnetic field is applied during the heating and cooling process, the Al_3Zr crystals tend to align with their <110> along the **FD**. This is probably caused by the magnetic

anisotropy of the primary Al_3Zr crystals. Similar to the primary Al_3Fe crystals, the magnetization energy reaches the minimum when the crystallographic direction of the crystal with the maximum magnetic susceptibility turns to the **FD** according to Eq. (3.2). Therefore, this direction tends to orient preferentially in the **FD**. In the present work, <110> is obviously this preferred direction.

The field induced rotation is also accomplished by the magnetic torque, and two other preventing torques induced by Lorentz force and viscosity resistance will also be generated once the crystal starts to be rotated by this torque. The alignment of most of the primary crystals in the deposit layer in Fig. 3.16(d) indicates that these preventing torques are overcome by the magnetic torque when a 12-Tesla field is applied. According to the calculation results of some other crystals under a similar situation [14, 28, 41], the rotation time should be very short (in the order of seconds). This means that they can be oriented before they deposit to the bottom of the crucible.

Other than the magnetic toque, the heat flow direction at the bottom of the crucible is also helpful for the final alignment of the primary crystals. As schematically shown in Fig. 3.12, the heat flow should be mainly in the vertical direction (parallel to the **FD**) at the bottom of the crucible. Therefore, growth in this direction will have the favorable heat evacuation condition. For the Al_3Zr crystals in the deposit layer, when they descend to the bottom during heating, they are already aligned to the field direction (i.e. <110>//**FD**). As analyzed previously in section 3.2.2, the growth of the Al_3Zr crystals is realized by the migration of the lateral {101}, or in another word, by stretching their top and bottom {001} planes. Once the <110> direction of the primary crystals is in the **FD**, the {001} planes are brought to be parallel to the heat flow direction, as illustrated in Fig. 3.23. In this position, the further stretch of the {001} planes is well coherent with the heat evacuation, thus the alignment can be maintained to the end of the solidification. In addition, the high magnetic field weakens the macroscopic convections induced by the descent of the primary crystals, and thus reduces the instability of the temperature field in the melt and hence provides a relatively stable environment. This further ensures the <110> alignment of the primary Al_3Zr crystals.

For the long bars that form during the cooling process, the field should have the same effect to align their <110> to the **FD**. However, this alignment will cause them to be in a

gravity instable position, as shown in Fig. 3.24. It is known that within a certain size range the

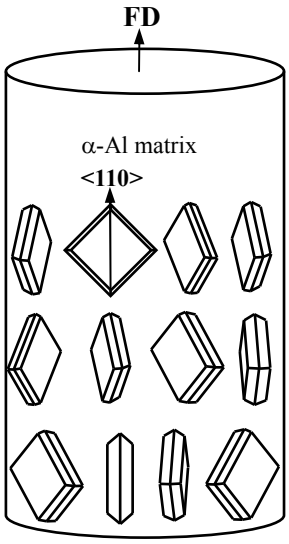

Figure 3.23 Three-dimensional scheme illustrating the alignment of the primary Al_3Zr crystals under a 12-Tesla magnetic field.

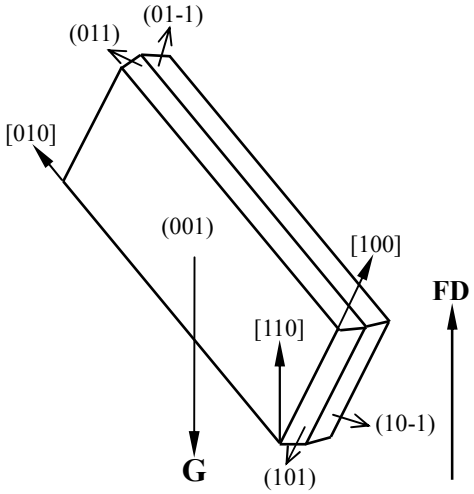

Figure 3.24 Schematic illustration of the effect of gravitational force on the long bar-shaped primary Al_3Zr crystals. **G** denotes the gravitational force.

gravity force plays an important role in affecting the orientations of the crystals [42]. As seen from the figure, the long bar shaped crystals tend to lie down to minimize its gravitational energy. Therefore, the final orientation of the long bars is the result of the competition between the magnetization force and the gravity force. As a consequence, the crystallographic directions of the vertical long bars in **FD** vary between <100> and <110>.

For the dendritic crystals (Fig. 3.17), as the branches and the primary trunks are twinned

with each other, their <110> crystallographic directions are inconsistent with each other. Therefore, their alignment cannot be well controlled by the magnetic field. As a consequence, no specific alignment can be achieved.

When the zirconium content is increased, another important factor in influencing the crystal orientation cannot be ignored - the interaction of the primary crystals with each other. In Al-1.36wt.%Zr alloy, the amount of the primary crystals is relatively low, so the interaction among them is not remarkable and the primary crystals can be easily rotated in the melt (Fig. 3.15(d)). However, in Al-1.95wt.%Zr alloy, the amount of the primary crystals is remarkably increased so that the interaction of some of them becomes unavoidable. As shown by the zoomed image in Fig. 3.20, crystal 1 is surrounded by crystals 2, 3 and 4. Under a high magnetic field, crystal 1 should possess a tendency to rotate with its longer axis parallel to the **FD**. However, its rotation will be hindered by crystals 2, 3 and 4. In addition, during the descent process of the primary crystals, the settlement of the later deposited crystals may impinge the previous ones and then change their orientations. All of these are detrimental to the final alignment of the primary Al_3Zr crystals. As a consequence, the alignment tendency of the primary crystals is weakened. For the randomly aligned long bars in the upper part of the specimen (Fig. 3.19), their orientations should also be deeply affected by the gravity force.

3.7 Conclusions

In the present work, Al-Fe and Al-Zr ingots are solidified under high magnetic fields and the results indicate that the precipitation behaviors of the primary Al_3Fe and Al_3Zr crystals are remarkably affected by the fields.

For the primary Al_3Fe crystals, the uniform field tends to eliminate the gravity segregation, whereas a positive one tends to create a new segregation. Under both cases, the field tends to align them with [100] longer axis perpendicular to the field direction and create strong preferential crystallographic orientation. Moreover, the field can also directly or indirectly induce axial bifurcation and transverse cracks in them and increase their nucleation number. The elimination and creation of segregations are respectively attributed to the Lorentz force and magnetization force; the alignment is induced by the magnetic torque due to the magnetic anisotropy; the bifurcation and the cracks are related to the thermoelectric magnetic force and

the linear shrinkage coefficient difference between the Al solid solution and the primary Al_3Fe phase; the increased nucleation number arises from the detachment of crystals and suppression of solute diffusion by the field.

For the primary Al_3Zr crystals, without and with a field they are mainly distributed at the lower parts of the specimens and in the form of small tabular crystals in the deposit layer, long bars and dendritic crystals. With a field, the crystals in the deposit layer and the long bars tend to align with the <110> longer axis to the field direction. However, the alignment of the dendritic crystals is less affected. The increased Zr content increased the precipitation amount of the crystals but weakens the alignment tendency of the crystals in the deposit layer. The segregation of the crystals results from their high density. The crystals in the deposit layers are those surviving from the heating; while the long bars are those forming during the cooling. The dendritic crystals are attributed to the compound twin. The alignment of the crystals in the deposit layer arises from the magnetic torque, but that of the long bars and dendritc crystals is disturbed by the gravity force and the inconsistence of the preferred direction, respectively. The weakness of the alignment arises from the interaction between the crystals.

Reference

[1] Michio S and Kei-ichi M, *Scr. Mater.*, 2002, 42:499-503.

[2] Tahashi M, Sassa K, Hirabayashi I and Asai S, *Mater. Trans. JIM*, 2000, 41:985-990.

[3] Taniguchi T, Sassa K, Yamada T and Asai S, *Mater. Trans. JIM*, 2000, 41:981-984.

[4] Li S Q, Wu C Y, Sassa K and Asai S, *Mater. Sci. Eng. A.*, 2006, 422:227-231.

[5] Asai S, Sassa K and Tahashi M, *Sci. Technol. Adv. Mater.*, 2003, 4:455-460.

[6] Mikelson A E and Karklin Y K, *J. Cryst. Growth*, 1981, 52:524.529.

[7] Savitisky E M, Torchinova R S and Turanoy S A J, *J. Cryst. Growth*, 1981, 52:519.

[8] Yasuda H, Tokieda K and Ohnaka I, *Mater. Trans. JIM*, 2000, 41:1005-1012.

[9] Rango P D, Lee M, Lejay P and Sulpice A, *Nature*, 1991, 349:770-772.

[10] Katsuki A, Tokunaga R, Watanabe S I and TanimotoY, *Chem. Lett.*, 1996, 25:607-608.

[11] Lu X Y, Nagata A, Watanabe K, Nojima T, Sugawara K, Hannda S and Kamada S, *Physica C*, 2002, 382:27-32.

[12] Chen W P, Maeda H, Kakimoto K, Zhang P X, Watanabe K, Motokawa M, Kumakura H

and Itoh K, *J. Cryst. Growth*, 1999, 204:69-77.

[13] Li X, Fautrelle Y and Ren Z M, *Acta Mater.*, 2007, 55:5333-5347.

[14] Wang C J, Wang Q, Wang Z Y, Li H T, Nakajima K and He J C, *J. Cryst. Growth*, 2008, 310:1256-1263.

[15] Li X, Fautrelleb Y and Ren Z M, *J. Cryst. Growth*, 2007, 306:187-194.

[16] Li X, Ren Z M and Fautrelle Y, *J. Cryst. Growth*, 2008, 310:3488-3497.

[17] Liu T, Wang Q, Gao A, Zhang C, Li D G and He J C, *J. Alloys Compd.*, 2009, 481:755-760.

[18] Sassa K, Waki N and Asai S, In: Mishra B and Yamauchi C (eds), *Proceedings of the Second Conference on Processing Materials for Properties, The Minerals, Metals and Materials Society,* San Francisco, 2000, p. 565.

[19] Wang Q, Wang C J, Pang X J and He J C, *Chin. J. Mater. Res.*, 2004, 18:568-576.

[20] Jin F W, Ren Z M, Ren W L, Deng K, Zhong Y B and Yu J B, *Sci. Technol. Adv. Mater.,* 2008, 9:1-6.

[21] Li X, Ren Z M and Fautrelle Y, *Mater. Des.*, 2008, 29:1796-1801.

[22] Wang Q, Lou C S, Liu T, Wei N, Wang C J and He J C, *J. Phys. D: Appl. Phys.*, 2009, 42:1-5.

[23] Lou C S, Wang Q, Wang C J, Liu T, Nakajima K and He J C, *J. Alloys Compd.*, 2009, 472:225-229.

[24] Allen C M, O'Reilly K A Q, Cantor B and Evans P V., *Prog. Mater. Sci.*, 1998, 43:89-170.

[25] Mondolfo L F, Aluminum alloys: structure and properties, Butterworth, London, 1976.

[26] Assael M J, Kakosimos K, Banish R M, Brillo J, Egry I, Brooks R, Quested P N, Mills K C, Nagashima A, Sato Y and Wakeham W A., *J. Phys. Chem. Ref. Data*, 2006, 35:285-300.

[27] Shimoji M, Liquid Metals, London: Academic Press, 1977.

[28] Sugiyama T, Tahashi M, Sassa K and Asai S, *ISIJ Int.*, 2003, 43:855-861.

[29] Lehmann P, Moreau R, Camel D and Bolcato R, *Acta Mater.*, 1998, 46:4067-4079.

[30] Li X, Ren Z M and Fautrelle Y, *Acta Mater.*, 2008, 56:3146-3161.

[31] Miyazakia S, Kawachib A, Kumaia S and Satoa A, *Mater. Sci. Eng. A*, 2005, 400-401:294.299.

[32] Belov N A, Aksenov A A and Eskin D G, Iron in aluminum alloys: impurity and alloying element, Taylor & Francis, London and New York, 2002.

[33] Ferreira P J, Liu H B and Vander Sande J B, *J. Mater. Res.*, 1999, 14:2751-2763.

[34] Hitchcock M, Wang Y and Fan Z, *Acta Mater.*, 2007, 55:1589-1598.

[35] Onishi T, Iwamura A E, Takaqi K and Yoshikawa K, *J. Vac. Sci. Technol. A*, 1996, 14:2728-2735.

[36] Kassemi M, Barsi S, Alexander J I D and Banish M, *J. Cryst. Growth*, 2005, 276:621-634.

[37] Miyake T, Inatomi Y and Kuribayashi K, *Jpn. J. Appl. Phys. Part 2*, 2002, 41:L811-L813.

[38] Hu X W, Theoretical Basis of Plasma, Beijing: Beijing University Press, 2006.

[39] Wang Q, Gao A, Liu T, Liu F, Zhang C and He J C, *J. Mater. Res.*, 2009, 24:2331-2337.

[40] Okamoto H, *J. Phase Equilib.*, 2002, 23:455-456.

[41] Zhang B W, Ren Z M, Wang H, Li X and Zhuang Y Q, *Acta Metall. Sin.*, 2004, 40:604.608.

[42] Wu C Y, Li S Q, Sassa K, Chino Y, Hattori K and Asai S., *Mater. Trans.*, 2005, 46:1311-1317.

Chapter 4 Microstructural transformation by conventional direct current magnetic field during the semi-continuous casting of Al-based binary alloys

4.1 Introduction

Semi-continuous casting is a common process for producing aluminum alloy products in industry. The casting ingots consisting of a uniform and refined grain microstructure is usually desirable for further processing, such as rolling, forging and extrusion. However, some other microstructures, such as columnar grains and feathery grains, often appear in the ingots. Each represents particular morphological and crystallographic characters and requires specific formation conditions. Columnar grains normally appear in small slabs on condition of approximate one-dimensional heat transfer and grow roughly perpendicular to the solid-liquid interface. Feathery grains, which are usually undesirable in manufacturing due to its strong anisotropy and non-uniform aspect after etching, occasionally occur in aluminum alloy ingots when specific solidification conditions (high temperature gradient at the solidification front, high cooling rate [1], the presence of convection [2] and/or certain alloying elements [3]) are met. Several efforts have been made on revealing the crystallographic characteristics and the formation conditions of this microstructure [2, 4]. It was found that they are made of twinned lamellas with the primary and secondary arms growing in <110> directions [4]. The primary trunks which constitute the lamellas are split in the center by their common {111} planes (the coherent twinning planes), while the secondary arms distribute systematically with respect to the {111} twinning planes on both sides of the primary trunks as “feathers”. The impingement of these “feathers” belonging to two neighboring lamellas forms the incoherent wavy boundaries. Simultaneously, side arms can also be found growing closely along <110> in the twinning planes. Moreover, the spacing between the columnar trunks in the twinning plane (in-plane spacing) is much smaller than the lamellar spacing (interplane spacing). The twin plane is associated with stacking faults which are favored by a strong shearing rate related to convection, while the transition of the growth direction is induced by solute additions and/or solidification conditions (thermal gradient, growth rate and melt convection). It was further clarified that under forced flow conditions the feathery growth is an intermediate case

between equiaxed and columnar growth and similar to the growth of <100> regular dendrites with the competitive branching-twinning mechanisms [5]. Despite many years of investigations [1-7], the formation mechanism of feathery grains is still not clearly understood and further investigation is required.

Since electromagnetic fields were introduced to the solidification process of metallic alloys, many interesting microstructural modification effects have been induced [8-18]. Considering the importance of semi-continuous casting technique and the easy availability of conventional direct current (DC) magnetic field, applying such a field during the semi-continuous casting of aluminium alloys is of practical and fundamental interest and may bring about some unexpected phenomena. Based on this, two Al-9.8wt%Zn and Al-0.24wt%Fe slabs were semi-continuously cast with and without the application of DC conventional magnetic fields in the present work in order to reveal the effects of the magnetic fields on the cast microstructures.

4.2 Experimental

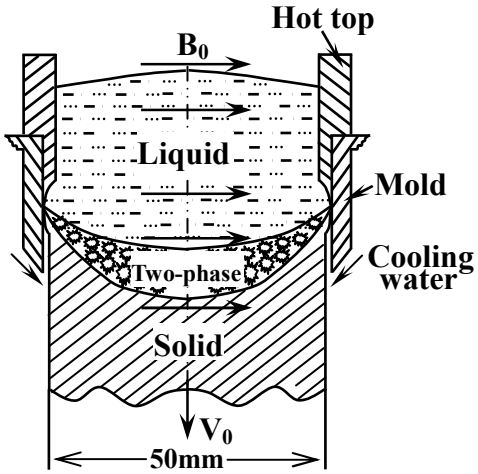

Figure 4.1 Schematic diagram of the casting configuration. $\mathbf{B_0}$ and $\mathbf{V_0}$ are the static magnetic field and the casting direction, respectively.

Two Al-9.8wt%Zn and Al-0.24wt%Fe slabs with dimensions of $50\times100\times1000mm^3$ were semi-continuously cast, respectively. The casting configuration is schematically illustrated in Fig. 4.1. The pouring temperatures for these two alloys were 720 °C and 715 °C, respectively, and the casting speeds $\mathbf{V_0}$ were both 3 mm/s. The melt was introduced to the mold by a horizontal inlet through the short-dimensioned side of the hot top. For the Al-9.8wt%Zn slab,

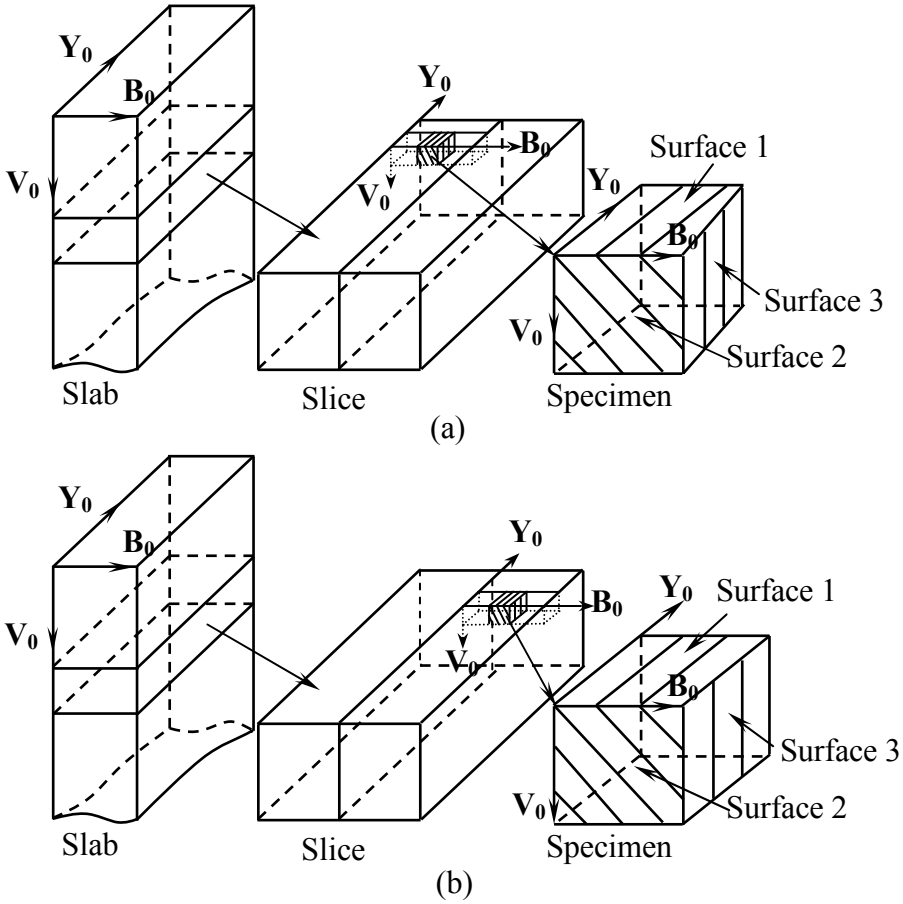

Figure 4.2 The schematic diagrams of the relative positions of the specimen and the slice in the (a) Al-9.8wt.%Zn and (b) Al-0.24 wt.%Fe cast slabs. $\mathbf{B_0}$, $\mathbf{Y_0}$ and $\mathbf{V_0}$ denote the horizontal DC magnetic field direction, melt pouring direction and casting direction, respectively.

the first half of the slab was cast without switching on a magnetic field, whereas the second half was cast under a horizontal direct current magnetic field $\mathbf{B_0}$ with a nominal value of 0.2 Tesla. For the Al-0.24wt%Fe slab, the first 1/3 part of the slab was cast without switching on a magnetic field, whereas the second 1/3 and the third 1/3 parts were cast under $\mathbf{B_0}$ with nominal values of 0.1 and 0.2 Tesla, respectively. The fields were imposed perpendicularly to the casting direction $\mathbf{V_0}$, as shown in Fig. 4.1. Several transverse slices with dimensions of 50×100×20 mm^3 to the casting direction $\mathbf{V_0}$ were cut out from the respective non-field and field cast parts for macrostructure observation. Afterwards, specimens with dimensions 5×5×5 mm^3 were further cut out from the slices for microstructural analysis. The relative positions between the specimen, slice and slab for these two alloys are schematically shown in Fig. 4.2(a) and (b), respectively. The microstructure observation was performed in the transverse section to the casting direction $\mathbf{V_0}$ (Surface 1), and in the two longitudinal sections of the

specimens – one parallel to the field direction $\mathbf{B_0}$ (Surface 2) and the other perpendicular to $\mathbf{B_0}$ (Surface 3) (for Al-9.8wt%Zn alloy, Surface 3 is nearly perpendicular to $\mathbf{B_0}$) to obtain the three-dimensional microstructural information.

The macrostructures of the slices were etched with NaOH (100g/L) reagent for 8 minutes after mechanical polishing and then washed with HNO_3(20%) reagent and taken with an OLMPUS C8080WZ camera; whereas the microstructures were etched with Keller's reagent (2ml HF(48%), 3mL HCl(concentrated), 5ml HNO_3(concentrated), 190ml H_2O)for a few seconds and observed using an OLYMPUS BX61 optical microscope. The crystallographic orientations of the microstructural constituents in the non-field and field treated specimens were measured and analyzed by EBSD technique attached to a JOEL JSM 6500 FE-SEM, equipped with HKL Channel 5 software after an electrolytic polishing (700ml ethanol, 120ml distilled water,100ml 2-butoxyethanol and 80 ml perchloric acid(6%), 40V, 5s). The EBSD mapping was performed with a step size of 2 μm for Al-9.8wt%Zn alloy and 0.7μm for Al-0.24wt%Fe alloy. Moreover, statistical analyses have also been made on the average primary spacing in the Al-0.24wt%Fe field cast specimens using the related micrographs and stereographic projections on the observation plane.

4.3 Results

4.3.1 Al-9.8wt%Zn alloy

Fig. 4.3 shows the cross section macrostructures of the non-field and field cast parts of the Al-9.8wt%Zn slab. It can be observed that without the magnetic field the grains are mainly equiaxed, while with the field the grains are lamellar.

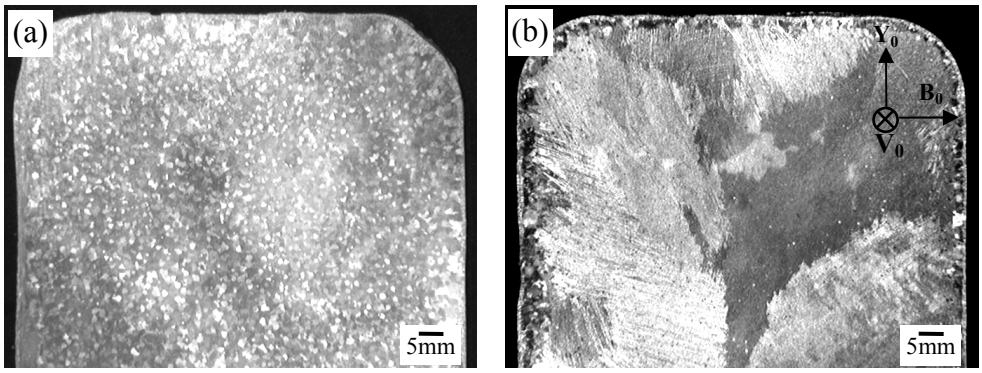

Figure 4.3 Macrostructures in the cross sections (to the casting direction $\mathbf{V_0}$) of the slices cast without (a) and with (b) a 0.2-Tesla DC magnetic field.

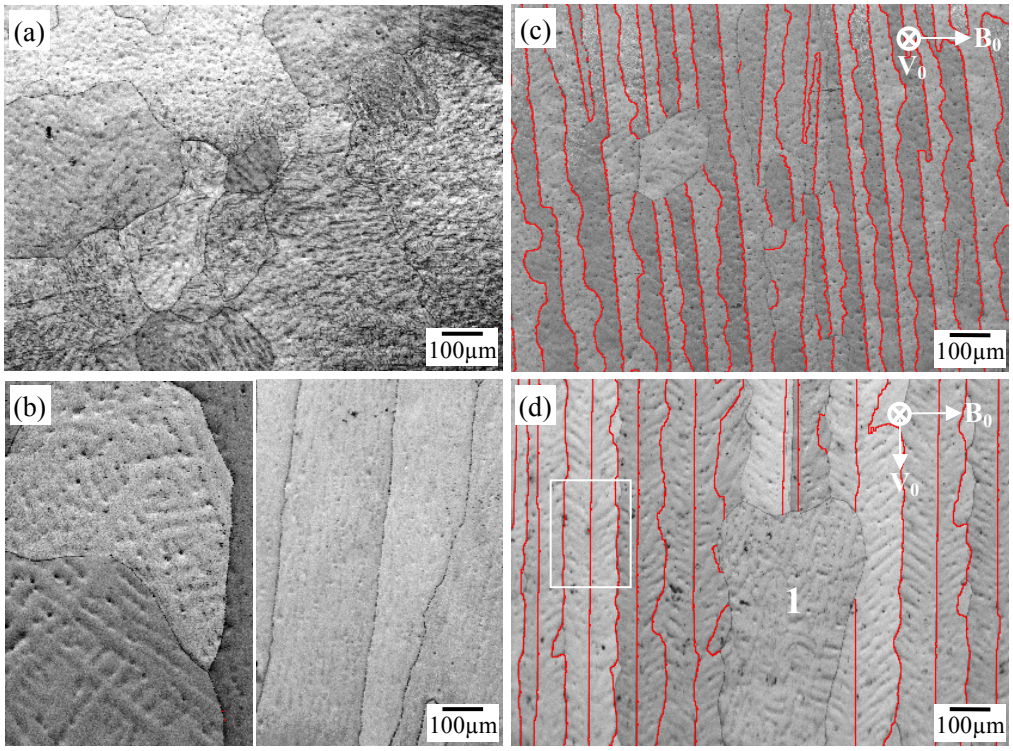

Figure 4.4 EBSD band-contrast orientation micrographs in the cross section and the longitudinal section (Surface 1 and 2 in Fig. 4.4(a)) of the non-field and field cast specimens. (a) Surface 1 and (b) Surface 2 of the non-field cast specimen; (c) Surface 1 and (d) Surface 2 of the field cast specimen. Red lines: Σ3 boundaries. The microstructure enclosed in the white frame will be further analyzed in Fig. 4.7.

The EBSD band contrast orientation micrographs from the cross section and the longitudinal section (Surface 1 and 2 in Fig. 4.2(a)) of the non-field and field cast specimens are shown in Fig. 4.4. From the two perpendicular sections, the three-dimensional image of the microstructure can be figured out. It is found that without the field (Fig. 4.4(a) and (b)), the microstructure consists of equiaxed and columnar grains; whereas with the field, the microstructure (Fig. 4.4(c) and (d)) is mostly composed of feather-like lamellas that are usually called “feathery crystals”. The red lines in Fig. 4.4(c) and (d) display the CSL Σ3 boundaries (we remind that CSL is the abbreviation of coincident site lattice in which the orientations of the two neighboring allow some lattice points of the other grain, see e.g. [19]). This boundary indicates that in cubic system the two neighboring crystals are related to each other by a 60° rotation around the common <111> axis. It has been well clarified that in FCC structures this orientation relationship defines the twin relation between the two crystals. The twinning plane is {111} and twinning direction is <11-2>. Fig. 4.4(c) and (d) clearly reveal the feathery character of the microstructure [1] obtained by magnetic field casting. It is

composed of thin lamellas, separated by straight and wavy boundaries, most of which are Σ3 boundaries. The straight Σ3 boundaries represent the coherent twin boundaries, while the wavy boundaries represent the incoherent twin boundaries. Columnar grains are occasionally spotted, but their growth is often suppressed by the feathery grains (i.e. 1 in Fig. 4.4(d)). Moreover, no Σ3 boundaries are found in Fig. 4.4(a) and (b).

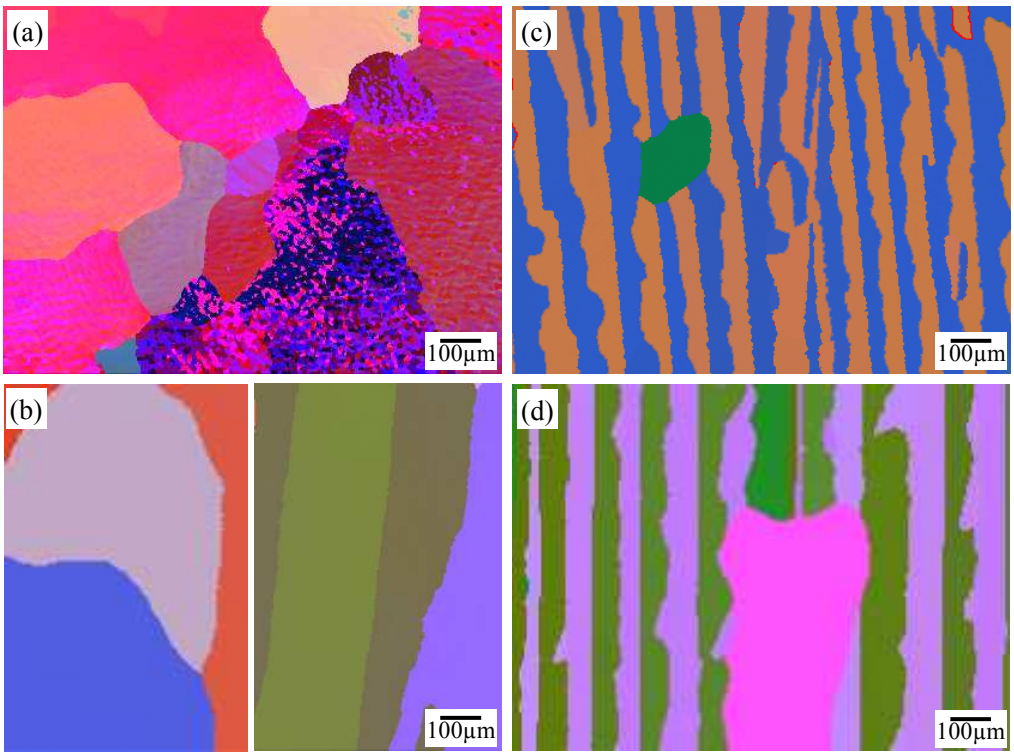

Figure 4.5 EBSD all-Euler orientation micrographs corresponding to Fig. 4.4(a)-(d). (a) Surface 1 and (b) Surface 2 of the non-field cast specimen; (c) Surface 1 and (d) Surface 2 of the field cast specimen.

To clearly show the difference of the crystallographic orientations between the non-field and field cast specimens, Fig. 4.5 (a)-(d) display the EBSD all-Euler orientation micrographs corresponding to Fig. 4.4(a)-(d), respectively. In these micrographs, different colors represent different orientations. As can be seen, without magnetic field the equiaxed and columnar grains are clearly distinguished by several different colors, whereas with magnetic field the lamellas are distinguished by two alternative colors, suggesting that this lamellar structure mainly possesses two orientations.

The grains in the non-field and field cast specimens differ from each other also in the crystallographic growth direction. Fig. 4.6 displays the <100> stereographic projections on the observation plane of the columnar grains in the non-field cast specimen shown in the right

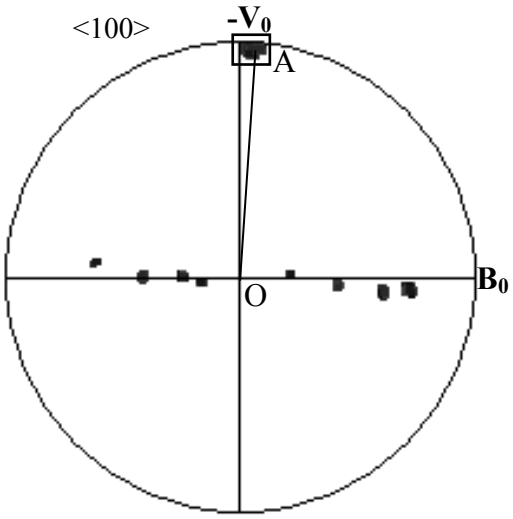

Figure 4.6 <100> stereographic projections on the observation plane corresponding to the columnar grains in Fig. 4.4(b).

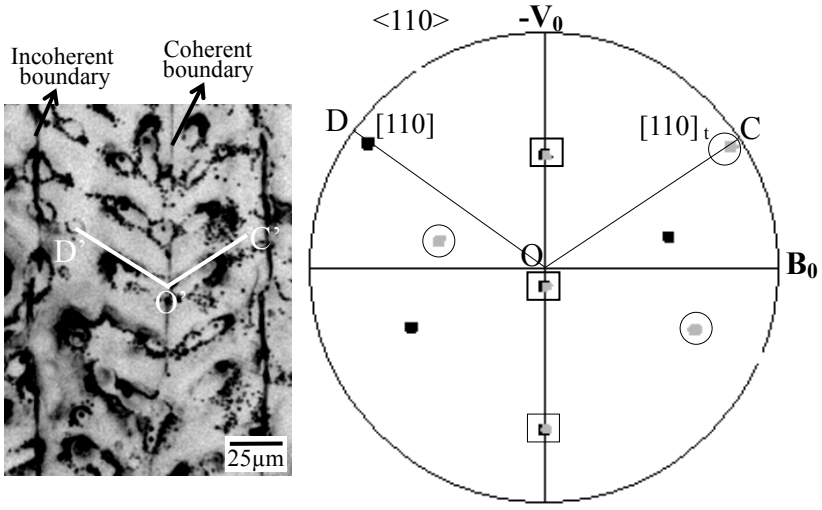

Figure 4.7 <110> stereographic projections on the observation plane of the corresponding feathery grains enclosed in the white rectangle in Fig. 4.4(d) and the zoomed micrograph.

part of Fig. 4.4(b). It can be observed that all grains share one <100> pole that is enclosed in the black square. The corresponding <100> direction is closely parallel to the casting direction $\mathbf{V_0}$, indicating that the principal growth direction of the columnar grains is <100>. Fig. 4.7 shows the <110> stereographic projections on the observation plane of the feathery grains enclosed in the white rectangle in Fig. 4.4(d) and the zoomed micrograph. The black poles are from the left part of the feathery grains and the grey ones in the circles from the twinned right part. The poles in the rectangles are common for both parts. The micrograph

well reveals one kind of secondary arms of the twinned feathery grain. From the contour (O'C' and O'D' in the micrograph of Fig. 4.7) of the secondary arms outlined by the dark contrast resulting from the solute segregation, it can be observed that they go continuously from the straight twinning boundary to the wavy boundaries that separate the adjacent feathery crystals, evidencing that the sectioning plane is parallel to the main axes of these secondary arms. The projection lines of the [110] (Line OD) and $[110]_t$ (Line OC) in Fig. 4.7 are very close to the true [110] and $[110]_t$ crystal lines as their poles are close to the outer circle of the stereographic projections on the observation plane (the index "t" refers to the twinned part as opposed to the matrix). In addition, OC and OD are, respectively, parallel to the secondary arm traces O'C' and O'D' in the micrograph. This indicates that these secondary arms grow along <110> directions.

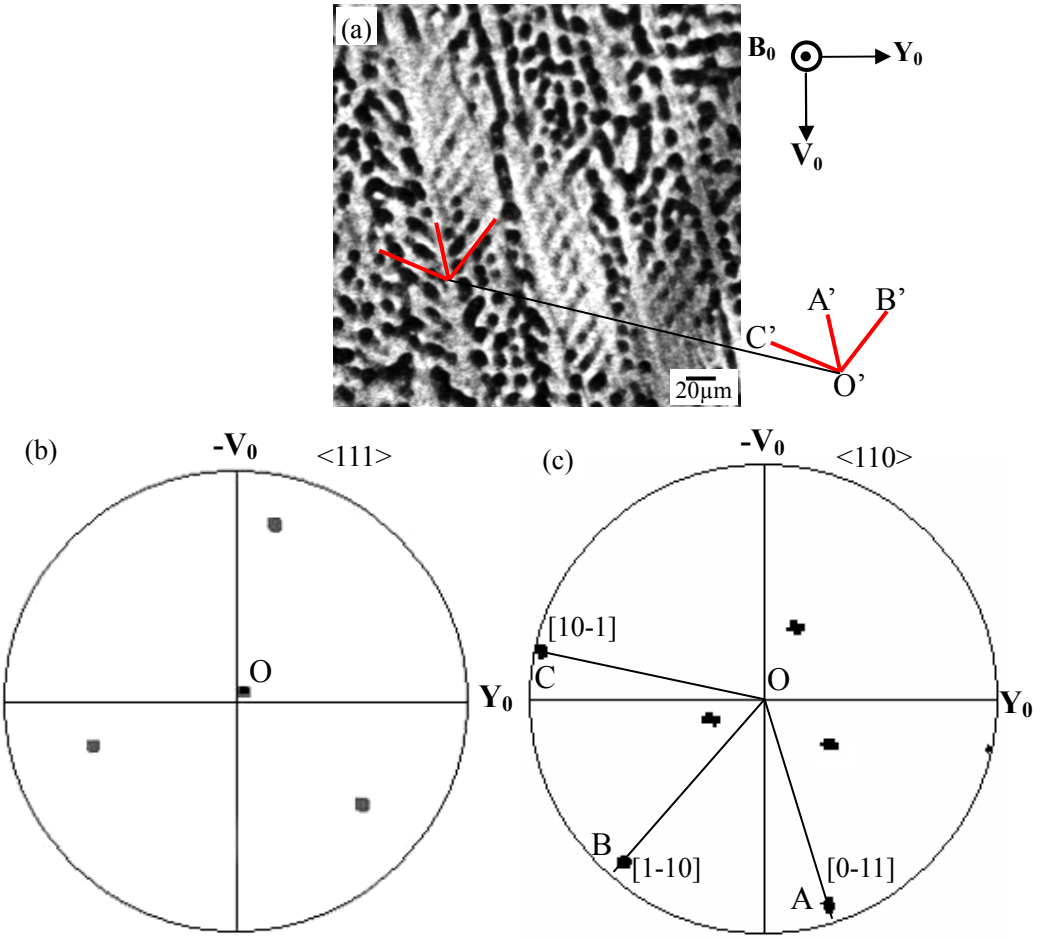

Figure 4.8 (a) the etched microstructure on Surface 3 in Fig. 4.2(a)); (b) <111> and (c) <110> stereographic projections on the observation plane corresponding to (a).

To find out the primary trunks and other possible secondary arms and their growth

directions, the microstructure on Surface 3 in Fig. 4.2(a) was etched out and is shown in Fig. 4.8(a). The related <111> and <110> stereographic projections on the observation plane are also displayed in Fig. 4.8(b) and (c), respectively. The micrograph in Fig. 4.8(a) clearly indicates the configuration of the primary trunks and the secondary arms that are distributed on both sides of the primary trunks. In the <111> stereographic projections on the observation plane, the pole O is near the center of big circle, indicating that the section we observe is just the {111} twinning plane. Following the same analyzing principles described above, it can also be found that the growth directions of the primary trunk (O'A') and those of the two secondary arms (O'C' and O'B') correspond to the poles A, B and C in the <110> stereographic projections on the observation plane. Thus, their growth directions can be determined as <110>. It should be noted that each of these secondary arms should possess a twinned counterpart with respect to the (111) twinning plane.

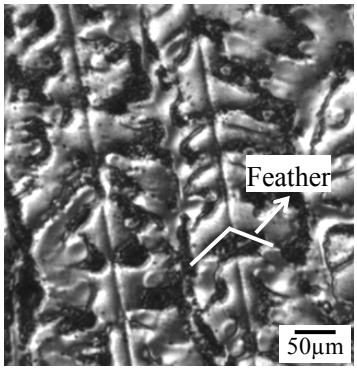

Figure 4.9 Etched microstructure in the transverse section corresponding to Surface 1 in Fig. 4.2(c).

To fully understand the three-dimensional microstructure of the feathery grains, Fig. 4.9 displays the etched micrograph on Surface 1 in Fig. 4.2(c). It can be observed that the "feathers" distribute symmetrically with respect to the straight boundaries and extend towards one direction (see the two white lines in Fig. 4.9).

Following the observation and analysis above, the crystallographic growth direction of feathery grains can be summarized as follows: if the primary trunks is supposed to grow along [01-1], the feathers grow along [110] and $[110]_t$ and the secondary arms in the twinning plane [10-1] and [-110], as schematically shown in Fig. 4.10.

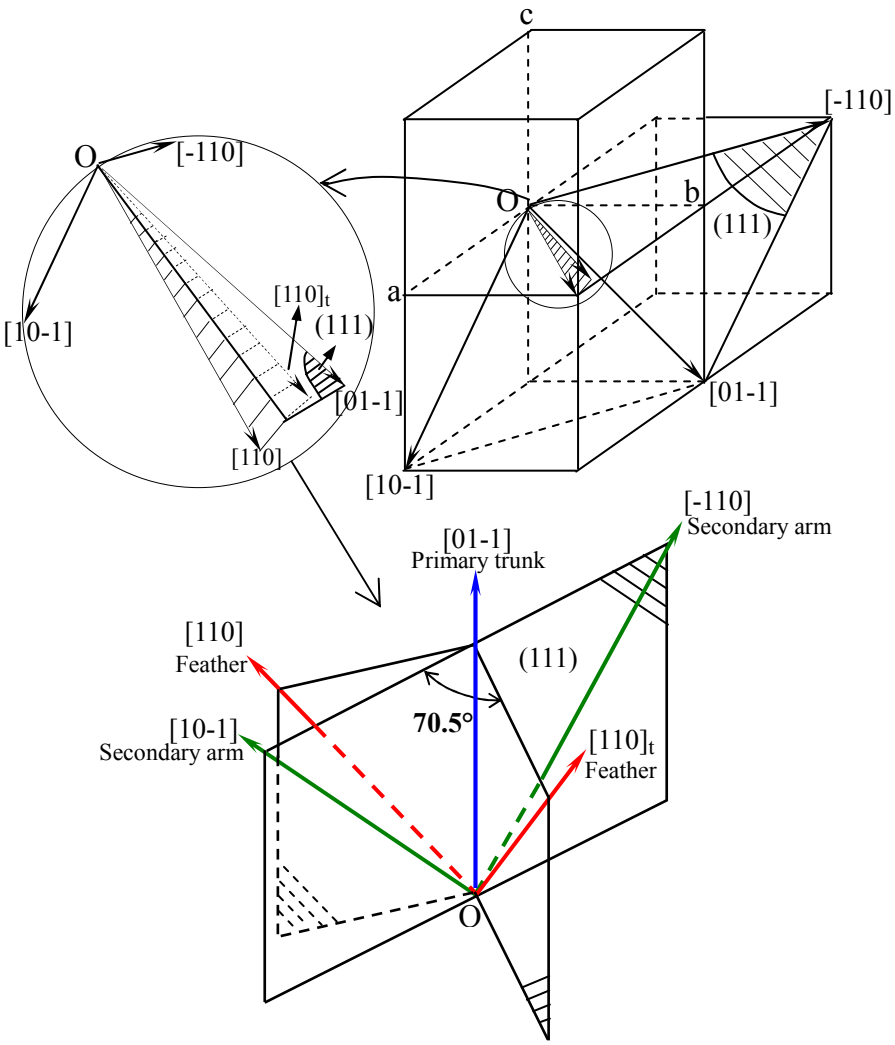

Figure 4.10 Crystallographic growth directions of feathery grain.

4.3.2 Al-0.24wt%Fe alloy

The etched microstructures on Surface 1 and Surface 2 (see Fig. 4.2(b)) of the non-field cast Al-0.24wt%Fe specimen are shown in Fig. 4.11(a) and (b), respectively. It is seen that it consists of two microstructural components: the proeutectic α phase (the light colored areas) and the eutectic mixture of the α phase and Al_3Fe (dark lines) distributed along the boundaries of the proeutectic α phase. The zoomed image of the eutectic structure is given in Fig. 4.11(e). The crystal structure of Al_3Fe is confirmed by indexing its EBSD Kikuchi patterns with Channel 5 software. It is seen that the eutectic mixture is composed of alternatively distributed α phase and needle shaped Al_3Fe, and meanwhile there is no clear separation between the proeutectic α phase (the matrix) and the eutectic α phase. The EBSD all-Euler orientation micrographs corresponding to the etched microstructures in Fig. 4.11(a) and (b)

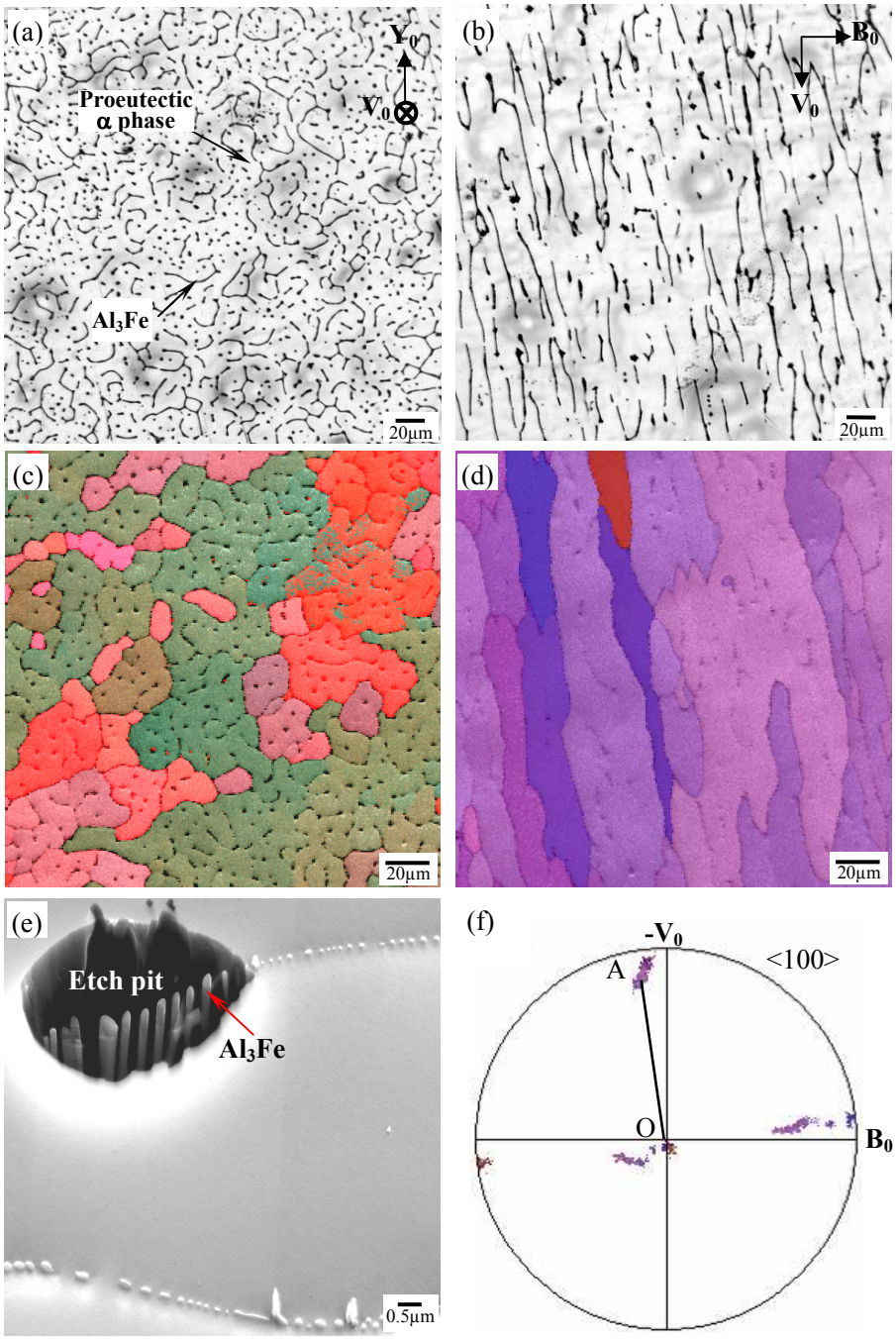

Figure 4.11 Etched microstructures on Surface 1 (a) and Surface 3 (b) cast under 0-Tesla filed; EBSD all-Euler orientation micrographs corresponding to Surface 1 (c) and Surface 3 (d); (e) the zoomed image showing the eutectic structure of α phase and Al_3Fe; (f) <110> stereographic projections on the observation plane corresponding to (d). The black part in the zoomed image (e) is a pit where the α phase is etched and Al_3Fe is left.

are given in Fig. 4.11(c) and (d). In these two orientation micrographs, the morphology of the proeutectic α grains revealed by different colors is clearly shown. Obviously, the grains are elongated in the casting direction, showing a typical columnar growth character. To determine their crystallographic growth direction, the crystallographic orientations of the grains were

carefully studied. The <100> stereographic projection on the observation plane corresponding to Fig. 4.11(d) is shown in Fig. 4.11(f). From the projections, it can be observed that all the grains share one common pole A. Considering the consistence of the OA direction (O is the origin of the circle of the projections) in the projections with the growth direction of the columnar grains in Fig. 4.11(d), it can be deduced that all the columnar grains grow along <100> direction.

Fig. 4.12(a) and (b) display the microstructures revealed by etching on the respective Surface 1 and Surface 3 of the 0.1-Tesla field cast specimen. Microstructure observation and analysis indicate that the alloy still consists of the same proeutectic α phase (the matrix) and eutectic mixture. However, the proeutectic α grains are remarkably changed by the field - from the columnar shape in the non-field specimen (Fig. 4.11) to the lamellar structure as displayed by the etched microstructure in Fig. 4.12(a) and (b). Fig. 4.12(d) and (e) display the EBSD all-Euler orientation micrographs corresponding to the etched microstructures in Fig. 4.12(a) and (b), respectively. The black lines plotted with the channel 5 software in the images

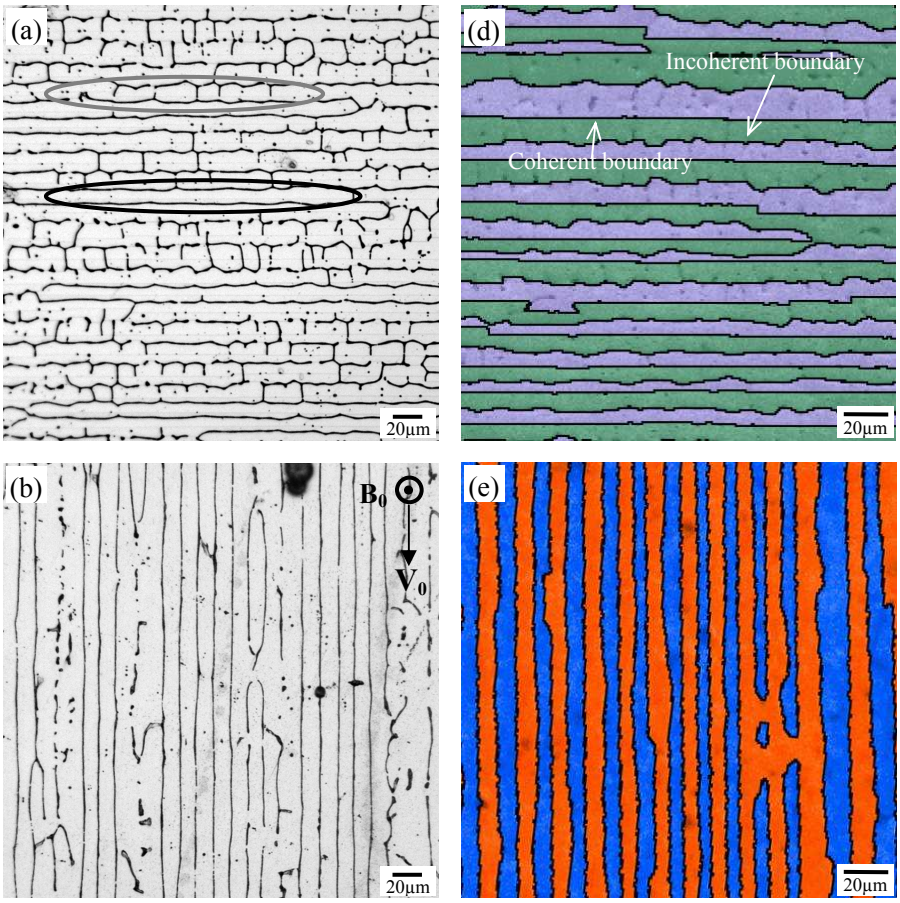

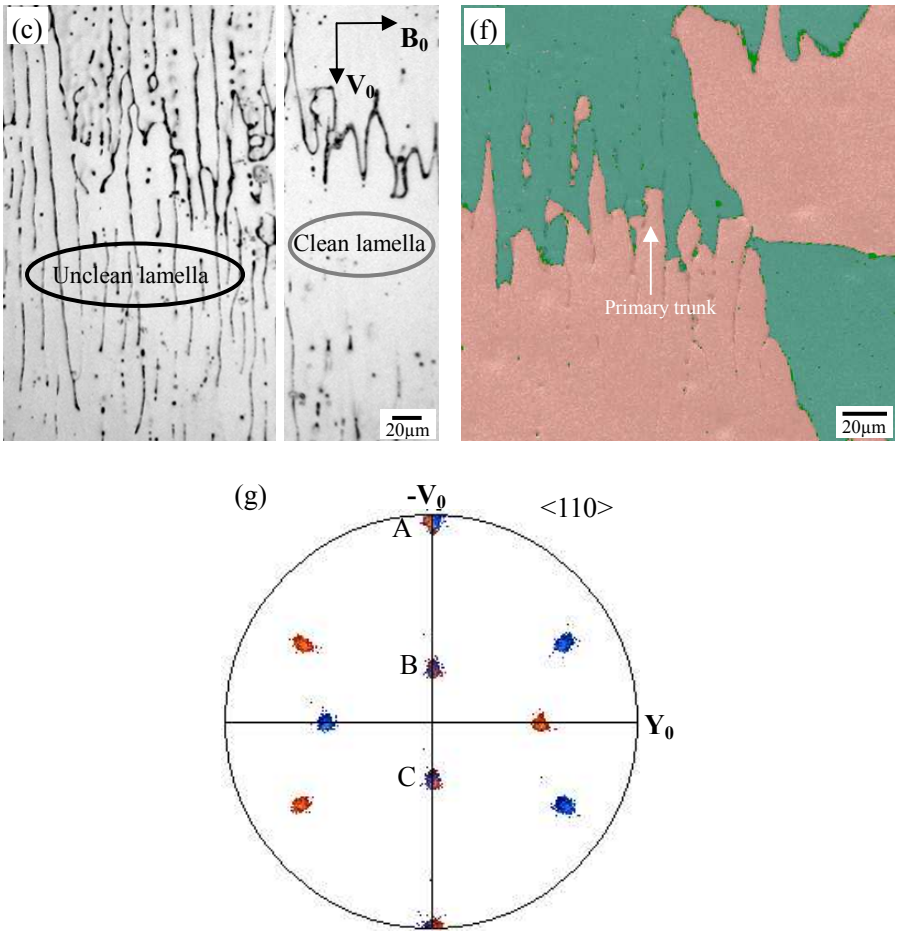

Figure 4.12 Etched microstructures on Surface 1 (a), Surface 3 (b) and Surface 2 (c) cast under 0.1-Tesla filed; EBSD all-Euler orientation micrographs corresponding to Surface 1 (d), Surface 3 (e) and Surface 2 (f); <110> stereographic projections on the observation plane (g) corresponding to (c).

show the CSL Σ3 boundaries between the α lamellas. Further orientation relationship analysis shows that the α lamellas are twin-related with {111} twinning plane and <11-2> twinning direction. The straight lines represent the coherent twin boundaries, whereas the wavy lines represent the incoherent ones. It is obvious that the eutectic mixtures are mainly distributed along the incoherent twin boundaries with a few of them formed inside the α lamellas. To find out the full morphology of the lamellas, Fig. 4.12(c) and (f) show the etched microstructure and the EBSD all-Euler orientation micrograph on Surface 2 (see Fig. 4.2(b)). It can obviously be seen that the lamellar proeutectic crystals have two characters. One is "clean" lamellas that are free of eutectic mixtures (circled in gray in Fig. 4.12(a) and (c)) and the other is the "unclean" lamellas that possess inner eutectic mixtures (circled in black in Fig. 4.12 (a) and (c)). The distribution of the inner eutectic mixtures outline columnar trunks, showing that

in reality one lamella is constituted of one array of columnar trunks. This can also be observed in Fig. 4.12(f). Based on the microstructural analysis above, both the average lamellar spacing (i.e. the interplane spacing) and the average spacing between columnar trunks in the twinning plane (i.e. in-plane spacing) are determined as around 14μm. To determine the growth direction of the primary trunks, Fig. 4.12(g) displays the <110> stereographic projections on the observation plane corresponding to Fig. 4.12(e). The colors of the poles correspond to the orientation colors of the related lamellas. Following the same analyzing principle, it is found that the columnar trunks that form the lamellas grow in <110> direction. The lamellar morphology and crystallographic growth direction of the proeutectic α phase in the present field-cast Al-0.24wt%Fe show the characters of the well known "feathery crystals", however no "feathers" (secondary arms) branching out from the twinning plane (Fig. 4.12(a) and (b)) and side arms in the twinning plane (Fig. 4.12(c)) are spotted in the microstructure, which represents a significant difference from the true "feathery crystals".

Fig. 4.13(a)-(c) display the etched microstructures on the respective Surface 1, Surface 3 and Surface 2 of the 0.2-Tesla field cast specimen. Their corresponding EBSD all-Euler orientation micrographs are given in Fig. 4.13(d)-(f). The black lines still indicate the Σ3 CSL boundaries. Fig. 4.13(g) displays the <110> stereographic projections on the observation plane of the lamellas corresponding to Fig. 4.13(e). Microstructure observation and crystallographic analysis indicate that under the 0.2-T field, there is no microstructural component and growth direction change. The proeutectic α phase is still composed of lamellar twins with the same crystallographic growth direction as those obtained under the 0.1-T field. The striking difference is that more eutectic mixtures formed inside the lamellar

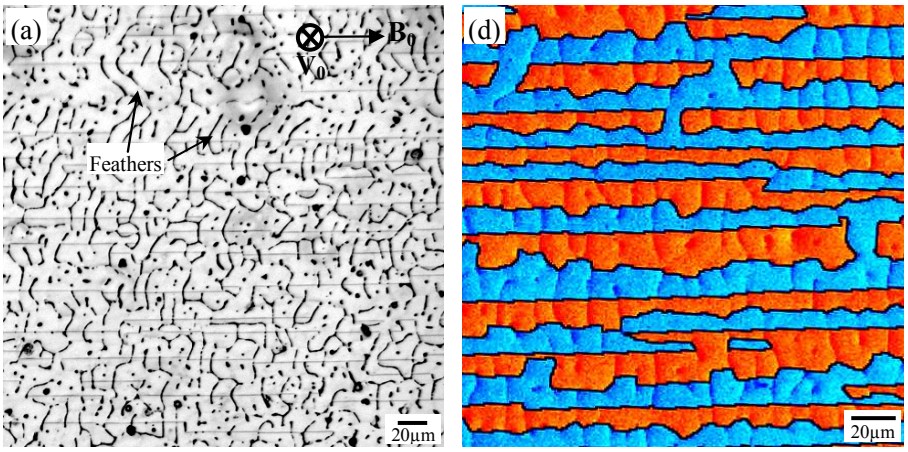

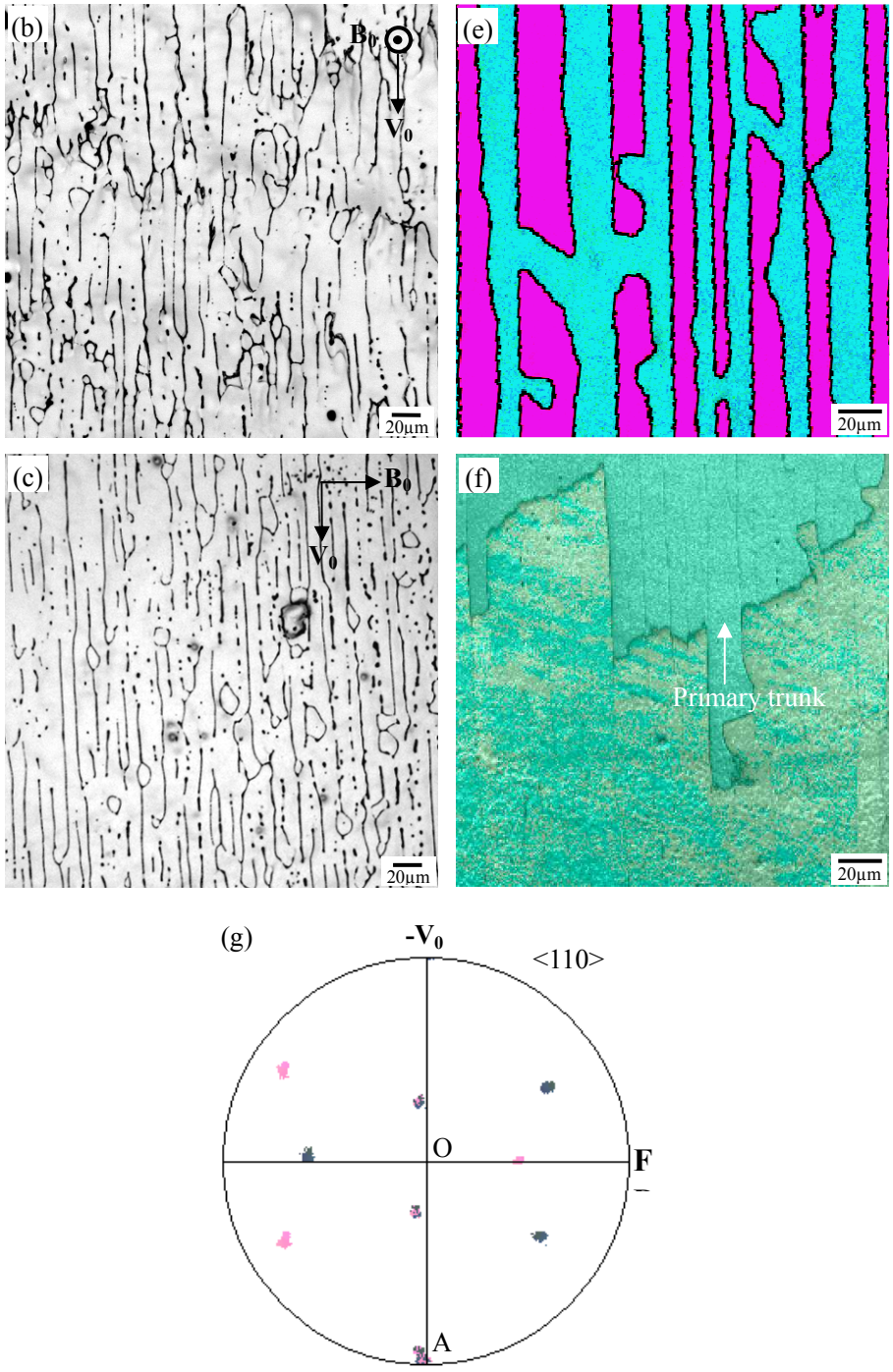

Figure 4.13 Etched microstructures on Surface 1 (a), Surface 3 (b) and Surface 2 (c) cast under 0.2-Tesla filed; EBSD all-Euler orientation micrographs corresponding to Surface 1 (d), Surface 3 (e) and Surface 2 (f); <110> stereographic projections on the observation plane (g) corresponding to (c).

α phase outlining not only the primary columnar trunks but also the initiation of the "feathers" (secondary arms), as arrowed in Fig. 4.13(a). However, side arms, as found in the true "feathery grains", are still not spotted in the twinning plane (Fig. 4.13(c)). Moreover, the average interplane spacing increases from about 14μm in the 0.1-T field cast specimen to

about 22μm, while the average in-plane spacing remains unchanged.

4.4 Discussion

4.4.1 Non-field crystal growth

For small slab casting, as in the case of the present study, columnar grains are generally expected due to the approximate one-dimensional heat transfer in normal semi-continuous casting condition (without a magnetic field) except those equiaxed grains forming in the peripheral region near the mould surface. However, dendrite fragmentation and subsequent crystal multiplication during solidification can happen due to convection [20, 21]. When a secondary branch of a columnar dendrite initially forms, an increase in the local temperature or shearing force due to convection can detach it from the dendrite. These fragments act as seeds for the equiaxed grains if the thermal and compositional conditions are appropriate. In the present experiment, this convection in the bulk liquid can be induced both by the temperature and solute concentration difference (natural convection) and mold filling (forced convection). Moreover, equiaxed grains can also probably grow from predendritic crystals which are formed during pouring at or near the mould and brought to the bulk by convection with some surviving. For Al-9.8wt%Zn alloy, dendrite fragmentation and subsequent crystal multiplication can easily happen due to its relatively high alloy concentration and thus the high constitutional undercooling which favors the growth of dendrites. Therefore, equiaxed and columnar grains can coexist in the non-field cast specimen (Fig. 4.4(b)). In contrast, the alloy concentration of Al-0.24wt%Fe alloy is low, so the chance for forming dendrite fragmentation is also small. Thus, only columnar grains form (Fig. 4.11(b)).

4.4.2 Field crystal growth

4.4.2.1 Braking effect of DC magnetic field on convection

It is well known that when electrically conducting melt crosses the DC magnetic field, flux variations occur, which lead to local electromotive forces [22]

$$\boldsymbol{E}_{\mathrm{m}} = \boldsymbol{u} \times \boldsymbol{B} \tag{4.1}$$

where $\boldsymbol{u}$ and $\boldsymbol{B}$ denote the local velocity and the magnetic flux density, respectively. Induced electric currents then arise

$$\boldsymbol{J} = \sigma\left(\boldsymbol{u} \times \boldsymbol{B}\right) \tag{4.2}$$

where σ is the electrical conductivity of the melt. The interaction of the induced electric currents with the applied static magnetic field gives rise to Lorentz force

$$\boldsymbol{F} = \boldsymbol{J} \times \boldsymbol{B} \tag{4.3}$$

in the direction against the local velocity component $\boldsymbol{u}_{\perp}$ perpendicular to the field, which brakes the flow of the melt.

The effectiveness of the magnetic field in damping the convection is usually quantified by Hartman number [23]

$$Ha = \mu BL\sqrt{\sigma/\eta_0} \tag{4.4}$$

where μ is the relative magnetic permeability (1[24]), L a characteristic length of the system (half width of the short-dimensioned side of the mold (0.025m) is taken in the present work [25]), σ electrical conductivity and η_0 the dynamic viscosity of the melt. When Ha>>1, the effective dynamic viscosity of the melt η_e can be expressed as [26]

$$\eta_e = \frac{Ha}{3}\left[1 + o\left(Ha\right)\right]\eta_0 \tag{4.5}$$

For Al-9.8wt%Zn alloy at 727 °C (close to the pouring temperature), the respective electrical conductivities of the pure aluminum and the aluminum with 70~80% zinc are $4\times10^6\Omega^{-1}m^{-1}$ and $2.63\times10^6\Omega^{-1}m^{-1}$[27], while the respective viscosities of the pure aluminum and the aluminum with 30% zinc are 1.178×10^{-3} Pa·s [28] and 2.23×10^{-3} Pa·s [27]. It is known that the electrical conductivity of the aluminum lineally decreases with the increase of zinc content, while the viscosity is just the opposite, i.e. it lineally increases with the increase of zinc in proportion [27]. In the present work, we can easily interpolate the respective σ and η_0 for the used alloy. They are $3.82\times10^6\ \Omega^{-1}m^{-1}$ and 1.3×10^{-3} Pa·s. For Al-0.24wt%Fe alloy, we take the related parameters of pure aluminium at 715 °C to estimate the values of *Ha* and η_e in the present work. Substituting the corresponding parameters into Eq. (4.4) and (4.5), *Ha* and η_e can be estimated and the results are given in Table 4.1.

Table 4.1 *Ha* and η_e in the alloy melt induced by the DC magnetic fields

Alloys	σ /$\Omega^{-1}m^{-1}$	η_0 / Pa·s	*L*/m	*B*/Tesla	*Ha*	η_e / Pa·s
Al-9.8wt.%Zn	3.82×10^6	1.3×10^{-3}	0.025	0.2	271	117.4×10^{-3}
Al-0.24wt.%Fe	4.17×10^6 [27]	1.2×10^{-3} [28]	0.025	0.1	147	58.9×10^{-3}
				0.2	294	117.8×10^{-3}

It has been proved that the convection was completely damped with a Hartman number of 54 by a vertical magnetic field during Czochralski growth of molten gallium [29]. From Table 4.1, it is seen that the Hartmann numbers for the two kinds of alloys under 0.1 or 0.2-T fields are much bigger than 54, suggesting that the melt motion in the direction perpendicular to $\mathbf{B_0}$ is effectively weakened by the field in the present work. In addition, it can also be found that the effective dynamic viscosities of the melt are also greatly increased when DC magnetic fields are applied.

4.4.2.2 Effect of DC magnetic field on heat and mass transfer

When a DC magnetic field is applied during the slab casting, the convection in the sump mainly caused by mold filling in the direction perpendicular to $\mathbf{B_0}$ will be slowed down by the Lorenz force and the effective dynamic viscosity of melt is also increased. As a consequence, the solidification conditions at the solidification front are modified. The braking of the convection and the increased effective dynamic viscosity reduce the superheat discharge into the mold and the solid and lowers the solute transmitting capacity in the melt, which result in the concentration of latent heat generated by solidification and the segregation of solute atoms at the solid/liquid interface. Both the concentrated latent heat and the segregated solute atoms decrease the undercooling degree at the solidification front, as the undercooling degree is defined as the temperature difference between the melting point and the real solidification temperature, i.e. the solid front temperature. It should also be noted that the solidification of the previous part of the slab (without magnetic field) also contributes to the latent heat and the solute enrichment and further decreases the undercooling degree at the solidification front. The reduction of the superheat evacuation delays the melt transformation from the liquid to solid [30] and the loss of undercooling decreases the growth rate and requires low solid/liquid interfacial energy according to the thermodynamic theory.

4.4.2.3 Crystallographic growth direction change by DC magnetic field

In metals of cubic crystal structure, dendrite tips grow in most cases along the <100> orientations [31]. The formation character of the columnar grains in the non-field cast specimen obviously obeys this rule. As mentioned above, when static magnetic field is applied, the loss of undercooling requires low solid/liquid interfacial energy. Thus, solidification path with lower interfacial energy is supposed to be triggered. This may account for the growth direction change from <100> (columnar grain) to <110> (feathery grains or lamellar crystals). Moreover, the loss of undercooling and the segregation of solutes at the solidification front may also change the surface tension and/or attachment kinetics anisotropy, and thus contribute to change of this growth direction. It has been proved in directional and Bridgman solidification that the increase of Zn concentration can transform the growth direction from <100> to <110> in Al-Zn alloy [32].

4.4.2.4 Formation of twinned lamellas

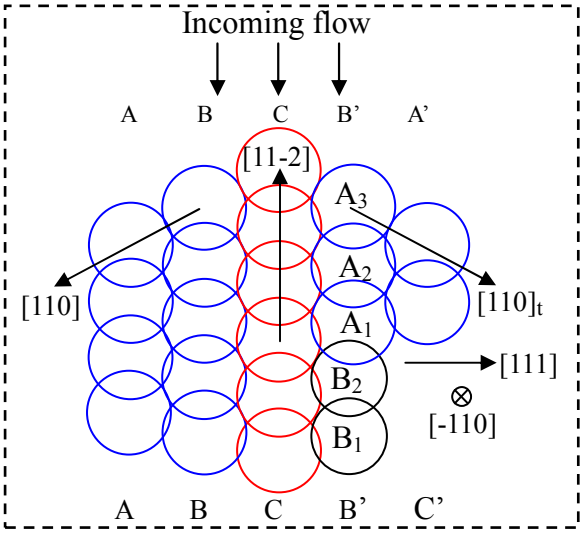

Figure 4.14 Schematic illustration of (111) stacking fault induced by the atomic radii difference between aluminum and zinc or iron and the incoming flow. B_1 and B_2 are zinc or Fe atoms and the others are aluminum atoms. The aluminum atoms in B' layer above B_1 and Z_2 go down and assume a mirror reflection position of the atoms in B with respect to the layer C.

Once the primary trunk grows in <110>, it will necessarily bring one {1-11} plane to the up-flow position. When atoms attach to the dendrite tips in the alloy, as illustrated in Fig. 4.14, some atomic positions in the growth direction could be occupied by zinc or iron atoms (B_1 and B_2) with the help of the incoming flow related to the columnar trunks. As the atomic radii

of Zn (133.5 pm [33]) and Fe (124.1 pm [33]) are smaller than that of Al (143.2 pm [33]), the aluminum atoms (A_1, A_2 and A_3) in Layer B' above the zinc or iron atoms (B_1 and B_2) go down to the positions lower than the normal ones and assume a mirror reflection position with respect to those in Layer C. Moreover, the lowering of the solute transmitting capacity of the melt, as mentioned above, guarantees sufficient solute alloy atoms left at the solidification front. Therefore, a stacking fault with respect to the {111} plane occurs readily. All of these give rise to the formation of twinning.

For the request of reducing solid/liquid interfacial energy under low undercooling condition, decreasing the total interfacial area is also a natural solution. It has been proved that in most metal systems with dendritic growth character, the solid/liquid interface is rough and exposes a lot of sides for the attachment of atoms from the liquid [31]. In the low undercooling condition, reducing interfacial area means lower its microscopic roughness. A more flat interface would be an ideal configuration. The <110> primary trunk surrounded by symmetrically distributed up-flow secondary <110> arms for Al-9.8wt%Zn alloy and the stacks of twin related lamellas with uniform lamellar spacing for Al-0.24wt%Fe alloy show collective growth tendency and similar growth preference, therefore such solid front could offer a low roughness solid/liquid interface. The arrangement of the parallel primary trunks forms one-twinned lamella (for the feathery grains, the primary trunk is also surrounded by symmetrically distributed up-flow secondary arms) and the packing of the identical lamellas forms a cluster of twinned lamellas. This would offer a large stretch of low roughness solid/liquid interface. In this way, large clusters of the feathery crystals or twinned lamellas appear. In addition, in cubic structure Σ3 boundary is the low energy boundary, therefore the formation of the twinned lamellar structure with Σ3 boundaries will also meet the request of low undercooling degree condition.

Furthermore, for Al-9.8wt%Zn alloy, the effective damping of convection by the magnetic field decreases the detachment of fragments from the secondary arms that act as seeds for equiaxed grains (these grains usually block the growth of columnar grains). In another word, the field provides a favorable environment and thus promotes the growth of feathery grains.

4.4.2.5 Effect of an enhanced 0.2-Tesla magnetic field on the twinned lamella growth in Al-0.24wt.%Fe alloy

The significant difference of the twinned lamellas formed in Al-0.24wt.%Fe specimen cast with 0.1-T magnetic field from the true "feathery crystals" is that there are neither "feathers" (secondary arms) branching off the primary trunks nor the side arms in the twinning plane forming. This is supposed to be attributed to the low initial Fe concentration. It is known that the presence of constitutional undercooling at the solidification front gives rise to the instability of the liquid/solid interface. With the growth of the columnar trunks, solutes are rejected both in front and to the sides of the columnar trunks tips. When there are sufficient solutes causing constitutional undercooling at the sides of the tips, secondary arms can be induced by a perturbation. However in the present investigated alloy, the solute concentration is very low. It seems that at this state (0.1T) the accumulated solute atoms around the columnar trunk are not enough to induce the secondary branching. As a result, they are mainly pushed to the incoherent twin boundaries with some left between the primary trunks inside the lamellas. It is reasonable to consider that the "clean" lamellas do not grow up as a whole, instead, they may also be composed of columnar trunks but just not outlined by sufficient Al_3Fe phase.

When the magnetic field increases from 0.1 Tesla to 0.2 Tesla, the braking effect on convection in the sump by Lorentz force becomes more efficient and further lowers the transmitting capacity of the solutes, and thus leaves more solutes at the solid front. Moreover, the solutes segregated from the two former casting parts (under 0-Tesla and 0.1-Tesla field) of the slab are pushed back to the last 1/3 part (under 0.2-Tesla field) and further enhances the solute concentration at the solidification front. The enhancement of the solute concentration makes the interface at the sides of the columnar trunk tips unstable. Thus, the initiation of "feathers" outlined by the Al_3Fe phase formed inside the lamellas becomes possible in the specimen cast under 0.2-Tesla magnetic field (Fig. 4.13(a)). However, the solute concentration is still not high enough to induce fully developed "feathers" (secondary arms) and side arms in the twinning plane as those in true "feathery grains". Thus, obvious branching traces on Surface 2 and side arms on Surface 3 can not be spotted.

According to Jackson-Hunt theory, the primary spacing λ is related to the temperature

gradient G_L ahead of the solidification front and the growth velocity V_S and assumes the following relation [34]

$$\lambda = AG_L^{-m}V_S^{-n} \tag{4.6}$$

where A is a constant proportional to the fourth root of the alloy composition for dilute alloys, and m and n are constants (generally m = 0.5 and n = 0.25). As the increased magnetic field further lowers the temperature gradient ahead of the solid front, decreases the growth rate and reduces the solute transmission capacity by damping convection, the primary spacing λ is increased by the magnetic field according to Eq. (4.6). Moreover, the former cast parts also contribute to the solute enrichment and latent heat concentration, and thus exert an influence on the primary spacing λ in the same direction. Actually, the primary spacing in the perpendicular direction to the twinning plane gives the lamellar spacing. Thus, the average lamellar spacing (i.e. the interplane spacing) in the specimen under 0.2-Tesla magnetic field becomes larger than that under 0.1-Tesla field. However, it should be noted that the lamellar spacing increases accompanied by the initiation of "feathers". Conversely, the average primary spacing in the twinning plane remaining unchanged should be related to the undeveloped side arms in this plane.

4.5 Conclusions

Two Al-9.8wt%Zn and Al-0.24wt%Fe slabs were semi-continuously cast under DC magnetic fields, respectively. A 0.2-Tesla DC magnetic field changes the solidification microstructure of the Al-9.8wt%Zn alloy from equiaxed and columnar grains to feathery grains, whereas a 0.1-Tesla DC magnetic field changes the microstructure of the Al-0.24wt%Fe alloy from regular columnar grains to twinned lamellas. Both transformations are accompanied by a change of growth direction from <100> to <110> and finally result in the formation of strong crystallographic texture and CSL Σ3 boundaries. The transformations are attributed to the modification of the solidification conditions at the liquid/solid front by the Lorentz force induced by the magnetic field. Both microstructural transformations are accompanied by a crystallographic growth direction change of the primary trunks from <100> to <110>. For the Al-0.24wt%Fe alloy, the lamellas bear the morphological and crystallographic characters of the "feathery grains". However, no "feathers" (secondary arms)

branch off the twinning planes at 0.1 Tesla, but only initiate at 0.2 Tesla. Under both fields, no side arms in the twinning planes were observed. Moreover, the interplane spacing increases with the increase of the field; whereas the in-plane spacing in the twinning plane remains unchanged. The microstructural transformations for both of these two alloys are mainly attributed to the modification of the solidification conditions at the liquid/solid front by the Lorentz force induced by the magnetic field. The difference between the Al and Zn (or Fe) atomic radii facilitates the formation of the twins. The lowered liquid/solid interface roughness required by the reduced undercooling degree accounts for the formation of lamellas. For the twinned lamellas in Al-0.24wt%Fe, the absence of "feathers" at 0.1-Tesla magnetic field is attributed to the low original Fe content, whereas the initiation of the "feathers" at 0.2-Tesla field results from the increased damping effect on convection.

Reference

[1] Anada H, Tada S, Koshimoto K and Hori S, *J. Jpn. Inst. Light Met.*, 1991, 41:497-503.

[2] Henry S, Gruen G U and Rappaz M, *Metall. Mater. Trans. A*, 2004, 35:2495-2501.

[3] Gullman L O and Johansson L, AIME, 1972, 345:437-463.

[4] Henry S, Jarry P and Rappaz M, *Metall. Mater. Trans. A*, 1998, 29:2807-2817.

[5] Turchin A N, Zuijderwijk M, Pool J, Eskina D G and Katgerman L, *Acta Mater.*, 2007, 55:3795-3801.

[6] Eady J A and Hogan L M, *J. Cryst. Growth*, 1974, 23:129-136.

[7] Granger D A and Liu J, *JOM*, 54.59.

[8] Uhlmann D R, Seward III T P and Chalmers B, *Trans. Metall. Soc. AIME*, 1966, 236:527-532.

[9] Ambardar R, *Aluminum*, 1986, 62:446-448.

[10] Youdelis W V and Dorward R C, *Can. J. Phys.*, 1966, 44:139-150.

[11] Youdelis W V and Cahoon J R, *Can. J. Phys.*, 1970, 48:805-808.

[12] Verhoeven J D and Pearson D D, *J. Mater. Sci.*, 1973, 8:1409-1412.

[13] Boettinger W J, Biancaniello F S and Coriell S R, *Metall. Trans. A*, 1981, 12:321-327.

[14] Tewari S N, Shah R and Hui S, *Metall. Mater. Trans. A*, 1994, A25:1535-1544.

[15] Alboussiere T, Moreau R and Camel D, *C. R. l'Academie. Sci., Ser. II Univers*, 1991,

313:749-55.

[16] Moreau R, Laskar O, Tanaka M and Camel D, *Mater. Sci. Eng., A*, 1993, A173:93-100.

[17] Moreau R, Laskar O and Tanaka M, *Magnetohydrodynamics*, 1996, 32:173-177.

[18] Li X, Gagnoud A, Ren Z M, Fautrelle Y and Moreaub R, *Acta Mater.*, 2009, 57:2180-2197.

[19] Zuo L, Watanabe T and Esling C, *Z. Metall.*, 1994, 85:554.558.

[20] Hunt J D and Jackson K A, *Trans. Met. Soc. AIME*, 1967, 239:864.867.

[21] O'Hara S, Tiller W A, *Trans. Metall. Soc. AIME*, 239:497-501.

[22] P. Gillon, *Mater. Sci. Eng*., 2000, 287:146-152.

[23] Carruthers J R, In: Wilcox W R and Lefever R A (eds), *Preparation and Properties of Solid State Material*s, Marcel Dekker, New York, 1977, vol. 3, p. 1.

[24] Metals Handbook, 8th ed., ASM, Metals Park, OH, 1961, vol. 1, p. 1064.

[25] Hunt J C R, *J. Fluid. Mech.*, 1965, 21:577-590.

[26] Wang C J, Wang Q, Wang Z Y, Li H T, Nakajima K and He J C, *J. Cryst. Growth*, 2008, 310:1256-1263.

[27] Mondolfo L F, Aluminum alloys: structure and properties, Butterworth, London, 1976.

[28] Marc J Assael, Konstantinos Kakosimos, Michael Banish R, Jürgen Brillo, Ivan Egry, Robert Brooks, Peter N Quested, Kenneth C Mills, Akira Nagashima, Yuzuru Sato and William A Wakeham, *J. Phys. Chem. Ref. Data*, 2006, 35:285-300.

[29] Szabo G, Juhaz Z, Paitz J and Poltl J, *J. Cryst Growth*, 1986, 78:558-560.

[30] Vives C and Perry C, *Int. J. Heat Mass Transfer*, 1987, 30:479-496.

[31] Cantor B and Vogel A, *J. Cryst Growth*, 1977, 41:109-123.

[32] Gonzales F and Rappaz M., *Met. Mater. Trans. A*, 2006, 37:2797-2806.

[33] Villars P, Pearson's Handbook Desk Edition, Crystallographic Data for Intermetallic Phases, ASM Int., Materials Park, OH, (Crys. Structure, Review, 5), 1997.

[34] Jackson K A and Hunt J D, *Trans. AIME*, 1966, 236:1129-1142.

Chapter 5 Conclusions and perspectives

The main objective of the present work is to theoretically and experimentally study the effects of magnetic field on the crystallography and microstructures of Al-based binary alloys, including the precipitation behaviors of the primary Al_3Fe and Al_3Zr phases under high magnetic field and the microstructural transformation of Al-Zn and Al-Fe alloys under conventional DC magnetic field. Besides these, we also systematically investigate the crystallographic features of the Al_3Fe and Al_3Zr phases. After a carefully theoretical and experimental study, the main achievements and conclusions have been drawn as follows.

5.1 Crystallographic features of the primary Al_3Fe and Al_3Zr phases

Al-3.3wt.%Fe and Al-1.36wt.%Zr alloys were solidified to form primary Al_3Fe and Al_3Zr phase. The crystallographic features of these two phases are investigated by EBSD technique and summarized up as follows.

5.1.1 Primary Al_3Fe phase

<010> and <011> are identified as the two preferred crystallographic extension directions of the bar-shape primary Al_3Fe crystals. In the case of <010> extension, a compound twin is observed; whereas in the case of <011> extension, both compound twin and type I twin are detected. The complete twinning elements for these two sorts of twins are determined. The morphologies of the primary Al_3Fe crystals are related to the crystallographic extension direction and twinning. Type I twin can induce the bent growth of the crystals. The Al_3Fe crystals are in two forms - monoclinic prism and triclinic prism. The crystallographic planes of their surfaces are identified as (100) and (001) in the extension direction for the monoclinic prism and (001), (001) and (02-1) for the triclinic prism. The twins are the result of the exposure of (001) and (001) planes in the Al melt during the growth.

5.1.2 Primary Al_3Zr phase

The primary Al_3Zr phase show tabular morphology. The longitudinal cut of the smaller crystals displays an octagonal form; whereas that of the larger crystals is in a rectangular one.

Primary crystals in dendritic form are also observed. The faceted planes binding the smaller sized crystals are crystallographically determined as {001}, {101} and {111}, whereas those binding the larger ones {001} and {101}. Two compound twins are detected in the dendritic crystal. The complete twinning elements for the twins are also determined. The tabular shape of the primary crystals and the disappearance of {111} in the larger sized crystals are related to the low roughness of {001} planes and high roughness of {111} planes, respectively. The twins are the result of the lattice shear plus local atom stacking fault accompanied by local atomic reshuffling. The dendritic crystals just result from the formation of the twins.

5.2 Effect of high magnetic field on the precipitation behaviors of the primary Al_3Fe and Al_3Zr phases

Al-3.31wt.%Fe and Al-1.36wt.%Zr (and Al-1.95wt.%Zr) ingots are solidified under various high magnetic fields. It is found that the precipitation behaviors of the primary Al_3Fe and Al_3Zr crystals are remarkably affected by the high magnetic fields.

5.2.1 Primary Al_3Fe phase

1) With a uniform magnetic field, the gravity segregation of the primary Al_3Fe crystals tends to be eliminated in the specimen. This is related to the prevention of the field-induced magnetic viscosity resistance.

2) With a uniform magnetic field, the primary Al_3Fe crystals tend to align with their <100> crystallographic direction parallel to the field direction and thus form strong preferential crystallographic orientation. This is due to the strong magnetic anisotropy of the primary phase and thus the magnetic torque acting on the crystals.

3) With a gradient field the primary Al_3Fe crystals move upward and segreate at the upper part of the specimen. This migration is driven by the magnetization force.

4) With the increase of magnetic fields, the nucleation amount of the primary crystals is increased. This may result from detachment of crystals and the suppression of solute diffusion by the field.

5) Axial bifurcation and transverse cracks are produced in the primary phase when magnetic field is applied. The bifurcation may result from the TEMF; whereas the cracks are related to the linear shrinkage coefficient difference between the Al solid solution and the

reduced anti-cracking ability of the primary phase.

5.2.2 Primary Al_3Zr phase

1) Without and with a field the primary Al_3Zr crystals are mainly distributed at the lower parts of the specimens and in the forms of small tabular crystals in the deposit layer, long bars and dendritic crystals. The distribution is attributed to the high density of Al_3Zr. The formation of the crystals in the deposit layers and long bars is correlated with the respective heating and cooling processes, whereas that of the dendrictic crystals results from the compound twin.

2) With a field both the crystals in the deposit layer and the long bars tend to align with the <110> longer axes to the field direction, but the dendritic crystals are less affected. The alignment tendency is attributed to the magnetic anisotropy of Al_3Zr and thus the induced magnetic torque. For the long bars the gravity force has a competition with the field, whereas for the dendritic crystals the in-consistent <110> direction in the twinned parts cause the alignment impossible.

3) The increase of Zr content induces an increased precipitation amount of the primary crystals and a weakened alignment tendency of the crystals in the deposit layer. The weakness is the result of the increased interaction between the crystals.

5.3 Microstructural transformation by conventional direct current magnetic field during the semi-continuous castings of Al-Fe & Al-Zr binary alloys

Two Al-9.8wt%Zn and Al-0.24wt%Fe slabs were semi-continuously cast under DC magnetic fields respectively and the results are summarized up as follows.

1) The solidification microstructure of the Al-9.8wt%Zn alloy changes from the equiaxed and columnar grains to the lamellar feathery grains accompanied by the crystallographic growth direction change from <100> to <110> after the application of a 0.2-Tesla DC magnetic field during the semi-continuous casting.

2) The solidification microstructure of the Al-0.24wt%Fe alloy changes from the regular columnar grains to the twinned lamellas accompanied by the transfer of the crystallographic growth direction from <100> to <110> after the application of a 0.1-Tesla DC magnetic field during the semi-continuous casting. The lamellas bear the morphological and crystallographic

characters of the “feathery crystals”. However, no “feathers” (secondary arms) branch off the twinning planes at 0.1 Tesla, but only initiate at 0.2 Tesla. Under both fields, no side arms in the twinning planes were observed. Moreover, the interplane spacing increases with the increase of the field; whereas the in-plane spacing in the twinning plane remains unchanged.

For both of these two alloys, the microstructural transformations give rise to the formation of strong crystallographic texture and CSL Σ3 boundaries. The application of the DC magnetic field results in the reduction of the heat discharge and solute mixing capacity through a damping effect on convection and thus a delay of the melt transformation to solid and a request to reduce the liquid/solid interface energy through reducing the interface area due to the loss of undercooling. The delay and the request account for the growth direction change and the formation of lamellas. Moreover, the possible change of the surface tension and/or attachment kinetics anisotropy may also contribute to the growth direction change. The difference between the Al and Zn (or Fe) atomic radii and the related incoming flow facilitate the formation of the twinning. The overall absence of “feathers” in Al-0.24wt%Fe alloy is attributed to the low initial Fe concentration. The increase of the interplane spacing is the result of the further lowered temperature gradient, growth rate and solute transmission capacity by the increased magnetic field; whereas the unchanged in-plane spacing in the twinning plane should be related to the undeveloped side arms in this plane.

5.4 Perspectives

Up to now, magnetic field has been widely used in various areas of materials science. Many interesting phenomena have been experimentally found and theoretically studied. However, this technique is still young and in its early stage. Based on the existing results, many phenomena and the correlated mechanisms are waiting to be figured out. Therefore, a more comprehensive study with theoretical depth in this field is required. According to the present work and the recent development of EPM, the future prospects of the application of magnetic field in materials science may be summarized as follows:

1) Extend the experimental target materials into a wider scope and try to find some new phenomena and regulations in various materials treatments and processing under magnetic field, and then work out the corresponding physical influential

mechanisms.

2) As the present high magnetic field production equipments are small, the experimental achievements and results cannot be transformed into practical applications. Based on this, the invention of equipments with larger sizes will be quite essential.
3) As analyzed on the crystallographic features of the Al_3Fe and Al_3Zr compounds in the present work, it is of theoretical interest and practical significance to carry out a crystallographic study on these kinds of intermetallic compounds. The incomplete crystallographic data of these compounds considerably restricts the further development of many areas of materials science. Therefore, a systematic study on various intermetallic compounds formed under different techniques is urgently needed.
4) So far, the application of conventional AC magnetic fields during the continuous (or semi-continuous) casting of metallic alloys has been widely researched. Besides the easy availability, the popularity of the conventional AC magnetic fields is mainly associated with their various favorable effects on the macro- and microstructures of the alloys. In contrast to the AC fields, the researches on the application of conventional DC magnetic fields are relatively seldom although they almost possess the same easy availability as the AC ones. One of the most important reasons is that they usually impair the properties of the alloys so that they lack practical values. However, in view of the theoretical and experimental values, applying DC fields during the continuous (or semi-continuous) casting of metallic alloys is of significance, which may be able to help increase knowledge about materials manipulating and controlling. Based on this, a lot of work is left to be done in the future.

Acknowledgments

The work presented in this thesis is completed in LETAM/University of Paul Verlaine-Metz, France and EPM/Northeastern University, China.

First, I would like to thank Prof. Yves Fautrelle and Prof. Zhongming Ren for spending their time reviewing my thesis.

This thesis has benefited from many kind and knowledgeable people. Without their help, this thesis could not be possible to be finished. Here, I would like to express my sincere appreciation to all of them. At the very beginning, I would like to give my deepest appreciation to Prof. Claude Esling, Prof. Jianzhong Cui and Prof. Yudong Zhang for their invaluable supports, guidance, encouragement and suggestions throughout my graduate career. I appreciate Prof. Claude Esling and Prof. Jianzhong Cui for their giving me the chance studying in LETAM and EPM. I specially appreciate Prof. Yudong Zhang for her large and unselfish help in my academic study and daily life.

I thank Prof. Liang Zuo and Prof. Xiang Zhao, who forged links and established a good relationship between Metz University and Northeastern University in the early years.

I wish to express a special gratitude to Zhihao Zhao, Yubo Zuo and their wives for their offering me the fund guarantee for my study in France.

I am grateful to all the staffs and students who helped me a lot during the preparation of my experiments in China, including Xingjie Na, Maoyong Huang, Shouwei Chang, Qixian Ba, Huixue Jiang, Dandan Chen, Qingfeng Zhu, Haitao Zhang, Zhiqiang Zhang, Ke Qin, Fu Qu, Bo Xu and Tianyou Kang.

I thank all the people in LETAM, who create a friendly atmosphere in which I can study with pleasure. I would like to express a special gratitude to the laboratory secretary Nathalie Niclas for all her kind help. I thank my three office colleagues Daoyong Cong, Song Li and Xiaoxue Zhang, with whom I had a good time. I also thank Jing Bai, Lei Bao, Zongbin Li, Jiang Wu and Xiangdong Zhang for their large help in my daily life.

I also gratefully acknowledge the CHINA SCHOLARSHIP COUNCIL and Region Lorraine for the Chinese-French Ph.D. grant.

Last but not least, my appreciation would go to my beloved family who has been a constant source of concern, support and strength all these years. Here, I have to give a special mention for the love, understanding and patience of my wife Liang Shuang.

Publication list

Refereed Publications in International Journals

1. **Lei Li**, Yudong Zhang, Claude Esling, Zhihao Zhao, Yubo Zuo, Haitao Zhang, Jianzhong Cui. Formation of feathery grains with the application of a static magnetic field during direct chill casting of Al-9.8wt%Zn alloy [J], Journal of Materials Science, 2009, 44:1063-1068.
2. **Lei Li**, Yudong Zhang, Claude Esling, Zhihao Zhao, Yubo Zuo, Haitao Zhang, Jianzhong Cui. Formation of twinned lamellas with the application of static magnetic fields during semi-continuous casting of Al-0.24 wt%Fe alloy, Journal of Crystal Growth, 2009, 311:3211-3215.
3. **Lei Li**, Yudong Zhang, Claude Esling, Huixue Jiang, Zhihao Zhao, Yubo Zuo, Jianzhong Cui. Crystallographic features of primary Al_3Fe phase, Journal of Applied Crystallography, 2010, 43: 1108-1112.
4. **Lei Li**, Yudong Zhang, Claude Esling, Huixue Jiang, Zhihao Zhao, Yubo Zuo, Jianzhong Cui. Crystallographic features of primary Al_3Zr phase, Journal of Crystal Growth. (accepted)
5. **Lei Li**, Yudong Zhang, Claude Esling, Huixue Jiang, Zhihao Zhao, Yubo Zuo, Jianzhong Cui. Influence of a high magnetic field on the precipitation behaviors of the primary Al_3Fe phase in the solidification of hypereutectic Al-3.31wt.%Fe alloy. (in preparation)
6. **Lei Li**, Yudong Zhang, Claude Esling, Huixue Jiang, Zhihao Zhao, Yubo Zuo, Jianzhong Cui. Influence of a high magnetic field on the alignment behavior of the primary Al_3Zr phase during the solidification of Al-Zr alloy. (in preparation)

Contributions to International Conferences

1. **Lei Li**, Yudong Zhang, Claude Esling, Zhihao Zhao, Yubo Zuo, Haitao Zhang and Jianzhong Cui, Effect of a static magnetic field on crystallographic orientation of Al-9.8wt%Zn alloy during semi-continuous casting, Texture et Anisotropie, SF2M-DGM, Université de Paris-Sud 11-Orsay, 2 et 3 avril 2009. (Poster)
2. **Lei Li**, Yudong Zhang, Claude Esling, Zhihao Zhao, Yubo Zuo, Haitao Zhang and Jianzhong Cui, Influence of magnetic fields on the microstructures of aluminium alloys during the solidification process, The 4th International Workshop on Materials Analysis and Processing in Magnetic Fields (MAP4), Georgia World Congress Center in Atlanta, Georgia U.S.A., May 10-12, 2010. (Poster)
3. **Lei Li**, Yudong Zhang, Claude Esling, Zhihao Zhao, Yubo Zuo and Jianzhong Cui, Influence of high magnetic field on the precipitation behaviors of Al-3.31wt.%Fe alloy during the solidification process, Réunion Texture & Anisotropie SF2M-DGM 2010, Joint French-German Meeting, SF2M-DGM, Dresden, 19.03.2010. (Poster)